

3D FEATURE EXTRACTION AND GEOMETRIC MAPPINGS FOR IMPROVED
PARAMETER ESTIMATION IN FORESTED TERRAIN USING AIRBORNE LIDAR DATA

By

HEEZIN LEE

A DISSERTATION PRESENTED TO THE GRADUATE SCHOOL
OF THE UNIVERSITY OF FLORIDA IN PARTIAL FULFILLMENT
OF THE REQUIREMENTS FOR THE DEGREE OF
DOCTOR OF PHILOSOPHY

UNIVERSITY OF FLORIDA

2008

© 2008 Heezin Lee

To my parents and wife

ACKNOWLEDGMENTS

First of all, I would like to express my gratitude to my advisor, Dr. K. Clint Slatton, for his great inspiration, support, and guidance over my studies. His supervision gave me a lot of opportunities to explore my research interests. I am also grateful to Dr. Ramesh Shresha, Dr. John G. Harris, Dr. Jianbo Gao, and Dr. Wendell P. Cropper Jr. for their valuable time and interest in serving on my supervisory committee, as well as their comments, which helped improve the quality of this dissertation.

My special acknowledgement goes to all of my ALSM and ASPL lab colleagues, Dr. William E. Carter, Abhinav Singhania, Bidhyananda Yadav, Carolyn Krekeler, Hojin Jhee, Hyunchong Cho, John Caceres, Juan Carlos Fernandez Diaz, Karthik Nagarajan, Kittipat Kampa, Kristofer Shrestha, Kuei-Tsung Shih, Michael Sartori, Michael Starek, Pang-wei Liu, Pravesh Kumari, Raghavendra Kumar, Sweungwon Cheung, Thelma Epperson, Tory Cobb, Tristan Cossio, and William Wright, for their help, collaboration and valuable discussions. They also brought me continuous fun, which was essential during my PhD study. I owe much to them all.

Finally, my utmost appreciation goes to my parents for always believing in me. Their unceasing love and whole-hearted support made finishing this work possible. Last but not most, I thank my wife, Hyeja, for her love, support, patience, and late night prayers.

TABLE OF CONTENTS

	<u>page</u>
ACKNOWLEDGMENTS	4
LIST OF TABLES	8
LIST OF FIGURES	9
LIST OF ABBREVIATIONS.....	12
ABSTRACT.....	14
CHAPTER	
1 INTRODUCTION	17
1.1 Airborne Laser Scanning	17
1.2 3D Airborne Laser Data over Forested Terrain	21
1.3 Organization of this Study and Contributions	23
2 STUDY SITES AND DATA ACQUISITIONS.....	27
2.1 Study Sites	27
2.2 Ground Truth and ALSM Data Acquisitions.....	30
2.3 Preprocessing	32
3 FIELD OF VIEW GEOMETRIC MAPPINGS.....	34
3.1 IPAR Estimation	34
3.1.1 Motivation.....	34
3.1.2 Estimation of <i>In-Situ</i> IPAR.....	38
3.1.3 Isolating the Vegetative Contribution to IPAR.....	40
3.1.4 Optical Scope Functions	41
3.1.5 Estimation of IPAR from ALSM.....	44
3.1.6 Results.....	46
3.1.6.1 Selection of the Best Scope Function.....	47
3.1.6.2 Variation in IPAR.....	48
3.1.6.3 Residual Analysis.....	49
3.1.7 Discussion.....	50
3.1.7.1 Factors Influencing <i>in situ</i> IPAR.....	50
3.1.7.2 Potential Sources of Error	51
3.1.7.3 Bias Between Species.....	52
3.1.7.4 Spatial Variations of IPAR _{ALSM}	53
3.2 Detecting Forest Trails.....	54
3.2.1 Introduction.....	54
3.2.2 Study Area and Data Acquisition	56

3.2.3	Data Segmentation	56
3.2.4	Visibility Vectors and Geometric Constraints	59
3.2.5	Result on Test Sites.....	61
4	A CLUSTERING APPROACH TO INDIVIDUAL TREE DETECTION.....	62
4.1	Introduction.....	62
4.2	Scale-Space Method.....	65
4.3	Proposed Algorithm.....	70
4.3.1	Finding Seed Locations.....	70
4.3.2	The Effect of R on Finding Seed Points.....	71
4.3.3	Region Growing Process.....	74
4.3.4	Agglomerative Hierarchical Clustering	77
4.4	Results and Comparison	82
4.5	Discussion.....	86
5	FOREST PARAMETER ESTIMATION.....	90
5.1	Introduction.....	90
5.2	Estimation of Tree Height and Crown Length.....	90
5.2.1	Tree Height (HT)	90
5.2.2	Crown Length (CL).....	90
5.3	Results and Discussion	92
5.3.1	Tree Height	92
5.3.2	Crown Length	94
5.3.3	Underestimation of the Parameters.....	94
5.3.4	Impact of LiDAR Point Density	95
5.4	Other Parameters.....	95
5.4.1	Crown Area.....	95
5.4.2	Diameter at Breast Height (DBH).....	96
5.4.3	2-Dimensional Open Gaps.....	96
5.4.4	3-Dimensional Open Gaps.....	97
6	SPIN IMAGES OF DIFFUSE TARGETS	99
6.1	Motivation.....	99
6.2	Spin Images.....	100
6.3	Creating Spin Images from ALSM Points	101
6.4	Spin Images of Canopy Clusters.....	104
6.5	Reducing Computational Complexity.....	110
6.5.1	Number of Bins.....	110
6.5.2	Number of Points on an Object.....	110
6.5.3	Number of Spin Images	111
7	CONCLUSIONS AND FUTURE WORK.....	112
7.1	Conclusions.....	112
7.2	Future Work.....	114

7.2.1	Extension to Different Forest Types	114
7.2.2	Line-of-Sight Visibility	115
7.2.3	Multi-feature Spin Images	116
7.2.4	New ALSM Technology	117
LIST OF REFERENCES		118
BIOGRAPHICAL SKETCH		127

LIST OF TABLES

<u>Table</u>		<u>page</u>
1-1	Typical performance specifications for UF-ALSM system	19
2-1	February, 2006 <i>in situ</i> field data from across the study sites describing general information about the sites.....	29
3-1	Plot level inventory data detailing tree survival and solar angles at the time of the <i>in situ</i> PAR measurements	38
3-2	Analysis of Variance (ANOVA) table for <i>in situ</i> and estimated IPAR	49
3-3	Least Squares estimates of IPAR measured <i>in situ</i> and estimated from ALSM.....	49
4-1	Algorithm of finding seed points.....	71
4-2	Region growing algorithm.....	76
4-3	Agglomerative clustering algorithm.....	80
4-4	Results of individual tree segmentation.....	84
4-5	Results of individual tree segmentation by the scale-space method.....	86
5-1	The mean differences between the ground truth values and the estimates of HT and CL	93
6-1	The mean value of the correlation coefficients for each case in Figure 6-4.....	109
6-2	The mean value of the correlation coefficients for each case in Figure 6-5.....	110

LIST OF FIGURES

<u>Figure</u>	<u>page</u>
1-1 Illustration of a small footprint LiDAR system in operation.....	20
1-2 An example of undersampling in LiDAR data over a natural forest.....	23
2-1 The locations of the study sites (PPINES and IMPAC) with the geographic range of slash pine shaded.....	28
2-2 A schematic layout of a single plot from each study site	29
2-3 Top view of first-stop LiDAR point heights of a typical plot from each cultural intensity at each site.....	30
2-4 Segmented ground laser points and the estimated ground elevation at the IMPAC site ...	33
2-5 Raw and flattened first/last stop elevation points	33
3-1 The spatial arrangement of the plots in the IMPAC site.....	37
3-2 Solar angles (θ, ϕ) defined relative to an observer point at the origin of a local spherical coordinate frame.....	39
3-3 Different types of scope functions investigated.....	42
3-4 The weighting functions for the cone scopes.....	43
3-5 Residual analysis comparing the two types of scope functions as dimensions change, where average absolute difference is simply the average absolute value of ALSM IPAR estimates minus <i>in situ</i> IPAR measurements.....	48
3-6 Relationship between observed (<i>in situ</i>) and estimated IPAR (from ALSM) using the cone function with $\alpha = 7^\circ$ and weighted by distance	50
3-7 A side view of a plot with a hypothetical position of the sun and a scope function.....	52
3-8 $IPAR_{ALSM}$ distribution for contrasting sun angles at an observer elevation of 2 m, illustrating the spatial resolution of $IPAR_{ALSM}$ computed in equation 7-2	53
3-9 Shaded relief image and ground photos of the study area	57
3-10 Point cloud from the training site.....	57
3-11 ALSM data points between 1 m and 4 m elevation (blue dots), tree trunks (black double circles), smooth surface points (red small circles), and GPS trail (yellow circles).....	58

3-12	All acquired visibility vectors and the winning trail candidate in the training site	60
3-13	The winning trail candidate in the testing site	61
4-1	Aerial photos illustrating the variation of canopy morphology even within managed pine forests	63
4-2	Creation of 2D height image from 3D LiDAR point clouds	66
4-3	An example of a scale-space representation	67
4-4	The detected blobs and strength of their scale-space signatures at each scale	68
4-5	The mean blob signature.....	69
4-6	The result of individual tree detection by the scale-space method	69
4-7	Identifying the seed points in two different cases.....	71
4-8	Sensitivity of the detection result to the search region R	72
4-9	The number of detected seeds depending on R in a small selected area.....	73
4-10	The changes in detected seed points that occur by changing the size of R from 10 m to 1 m	73
4-11	An illustration of a case where T is necessary	75
4-12	An example of the region growing result	76
4-13	An example of hierarchical tree and merged clusters at specific levels of R	78
4-14	Probability density functions of the two classes (w_1 : partial tree clusters, w_2 : complete tree clusters) estimated by the Parzen windowing method	81
4-15	The segmentation result over the small area.....	82
4-16	Methodology overview of the proposed algorithm.....	83
4-17	An example of the segmentation results (a plot with high culture at PPINES).....	85
4-18	Performance comparison between the proposed method and the scale-space method.....	86
4-19	A top view of the low culture PPINES plot shown in Figure 2-3.....	89
5-1	An illustration of estimates of HT, HTLC, and CL on segmented LiDAR points	98
5-2	An example of the maximum possible open angles at locations on the ground.....	98

6-1	The object centered 3-D coordinate system to create a spin image.....	101
6-2	Selection of the size of spin image	102
6-3	An example of a spin image of a full tree cluster	104
6-4	Spin images of each cluster in Figure 3-9.....	106
6-5	Spin images of tree clusters from three different classes.....	107

LIST OF ABBREVIATIONS

AGL	Above Ground Level
ALSM	Airborne Laser Swath Mapping
ANOVA	Analysis of Variance
CD	Crown Diameter
CL	the length of live crown
DBH	Diameter at Breast Height
DEM	Digital Elevation Model
DSM	Digital Surface Model
EAARL	Experimental Advanced Airborne Research LiDAR
FBRC	Forest Biology Research Cooperative
FOV	Field Of View
FWHM	Full Width Half Maximum
GMM	Gaussian Mixture Model
GPS	Global Positioning System
HT	Tree Height
HTLC	the height to the base of the live crown
IFAS	Institute of Food and Agricultural Sciences
IMPAC	Intensive Management Practices Assessment Center
INS	Inertial Navigation System
InSAR	Interferometric Synthetic Aperture Radar
IPAR	Intercepted Photosynthetically Active Radiation
IR	InfraRed
KARS	Kinematic And Rapid Static
KL	Kullback-Leibler

LAI	Leaf Area Index
LiDAR	Light Detection and Ranging
LVIS	Laser Vegetation Imaging Sensor
MI	Mutual Information
PAR	Photosynthetically Active Radiation
PCA	Principle Component Analysis
pdf	probability density function
PPINES	Pine Productivity INteractions on Experimental Sites
RF	Radio Frequency
RMS	Root-Mean-Square
ROI	Region Of Interest
SLICER	Scanning LiDAR Imager of Canopies by Echo Recovery
UF-ALSM	University of Florida – Airborne Laser Swath Mapping
UTM	Universal Transverse Mercator

Abstract of Dissertation Presented to the Graduate School
of the University of Florida in Partial Fulfillment of the
Requirements for the Degree of Doctor of Philosophy

3D FEATURE EXTRACTION AND GEOMETRIC MAPPINGS FOR IMPROVED
PARAMETER ESTIMATION IN FORESTED TERRAIN USING AIRBORNE LIDAR DATA

By

Heezin Lee

May 2008

Chair: K. Clint Slatton

Major: Electrical and Computer Engineering

Scanning laser ranging technology is well suited for measuring point-to-point distances because of its ability to generate small beam divergences. As a result, many of the laser pulses emitted from airborne light detection and ranging (LiDAR) systems are able to reach the ground underneath tree canopies through small (10 cm scale) gaps in the foliage. Using high pulse rate lasers and fast optical scanners, airborne LiDAR systems can provide both high spatial resolution and canopy penetration, and these data have become more widely available in recent years for use in environmental and forestry applications. The small-footprint, discrete-return Airborne Laser Swath Mapping (ALSM) system at the University of Florida (UF) is used to directly measure ground surface elevations and the three-dimensional (3D) distribution of the vegetative material above the soil surface.

Field of view geometric mappings are explored to find optical gaps inside forests. First, a method is developed to detect walking trails in natural forests that are obscured from above by the canopy. Several features are derived from the ALSM data and used to constrain the search space and infer the location of trails. Second, a robust and simple procedure for estimating intercepted photosynthetically active radiation (IPAR), which is an important measure of forest timber productivity and of daylight visibility in forested terrain, is presented. Simple scope

functions that isolate the relevant LiDAR reflections between observer locations and the sun are defined and shown to give good agreement between the LiDAR-derived estimates and values of IPAR measured *in situ*. A conical scope function with an angular divergence from the centerline of $\pm 7^\circ$ provided the best agreement with the *in situ* measurements. This scope function yielded remarkably consistent IPAR estimates for different pine species and growing conditions. The developed idea could be extended, through potential future work, to characterize the spatial distribution of attenuation of GPS (L-band) microwave signals and of detectability from the sky for military personnel operating in forested terrain.

Measuring individual trees can provide valuable information about forests, and airborne LiDAR sensors have been recently used to identify individual trees and measure structural tree parameters. Past results, however, have been mixed because of reliance on interpolated (image) versions of the LiDAR measurements and search methods that do not adapt to variations in canopies. In this work, an adaptive clustering method is developed using 3D airborne LiDAR data acquired over two distinctly different managed pine forests in North-Central Florida, USA. A critical issue in isolating individual trees is determining the appropriate size of the moving window (search radius) when locating seed points. The proposed approach works directly on the 3D “cloud” of LiDAR points and adapts to irregular canopy sizes. The region growing step yields collectively exhaustive sets in an initial segmentation of tree canopies. An agglomerative clustering step is then used to merge clusters that represent parts of whole canopies using the locally varying height distribution. The overall tree detection accuracy achieved is 95.1% with no significant bias. The tree detection enables subsequent estimation of tree height and vertical crown length to an accuracy of better than 0.8 m and 1.5 m, respectively. Lastly, a compact representation of the different geometric characteristics of the segmented LiDAR points is

introduced using spin images as a new tool that can potentially help tree detection in complex natural forests.

CHAPTER 1 INTRODUCTION

1.1 Airborne Laser Scanning

There are two major classes of airborne laser ranging technologies currently in use: (1) large-footprint, full-waveform systems; and (2) small-footprint, discrete-return systems. Large-footprint LiDAR systems, such as the NASA Laser Vegetation Imaging Sensor (LVIS) (Drake *et al.*, 2002) and Scanning Lidar Imager of Canopies by Echo Recovery (SLICER) (Lefsky *et al.*, 1999a), generally have footprint diameters of tens of meters. The return signal is finely sampled over a long range gate, yielding a digitized reflected laser waveform. Because the large footprint spreads the transmitted photons over a wide area, many photons penetrate deep into the canopy, providing a densely sampled vertical profile. While, large-footprint systems have been used to estimate forest biophysical parameters (Lefsky *et al.*, 1999a; Lefsky *et al.*, 1999b; Means *et al.*, 1999; Ni-Meister *et al.*, 2001; Parker *et al.*, 2001; Hyde *et al.*, 2005), they are incapable of sensing structure over meter-scale spatial (horizontal) extent since the received waveform represents an integrated response for the entire area illuminated by the footprint. This limitation also leads to non-unique functional mappings from the received waveforms back to forest structure because an infinite number of structural configurations can, in principle, result in the same waveform shape. Consider, for example, a patch of forest illuminated by the circular footprint. Rotating that patch 180° about the laser bore sight will not change the received waveform. Also, full-waveform LiDAR sensors primarily remain research tools due to the excessive data volumes and associated per unit area acquisition costs (Flood, 2002). The experimental NASA system, Experimental Advanced Airborne Research Lidar (EAARL), combines waveform digitization with small-footprints (Brock *et al.*, 2002). However, the laser pulse rate is comparatively low, which further reduces terrain sampling rates. The LiDAR data

used in this work belongs to the small-footprint class of airborne laser-ranging technologies, which is more accessible to the wider research and forest management communities.

Small-footprint LiDAR systems, such as Airborne Laser Swath Mapping (ALSM) system at the University of Florida (UF), can provide spatially dense (decimeter scale) sampling of the foliage and surface in three-dimensions (3D). The point location accuracy of the UF-ALSM system is nominally 15-20 cm horizontally and 5-10 cm vertically. The UF-ALSM unit was dramatically upgraded in February 2007, but the unit that was in use prior to that was used to collect all data in this work. It records both first and last laser reflections per outgoing pulse at a rate of 33 kHz with a transmitted pulse duration (τ) of 10 ns (3 m path length) at a near-infrared laser wavelength (λ) of 1064 nm. It also records a relative intensity of each reflection where the intensity of the reflected signal depends primarily on the surface material of the target (Carter *et al.*, 2001), but also on the incidence angle. High-resolution multispectral imagery is acquired concurrently. The system records the ranges of the first and last return pulses using a constant fraction discriminator at the output of an avalanche photodiode detector to detect the Full Width Half Maximum (FWHM) points on the returned laser waveform (Slatton *et al.*, 2005). As with all discrete-return ALSM systems, the pulse length imposes a lower limit on the vertical resolution between return pulses. The approximate minimum vertical distance for which separable first and last returns can be recorded, given the 10 ns pulse duration, is 2.5 m. The distribution of laser spots on the terrain is created by a single-axis oscillating mirror. Together with the forward motion of the aircraft, it creates a saw-toothed pattern on the ground along the flight path. The half-angle laser beam divergence is 0.125 mrad, resulting in a laser footprint that is approximately 15 cm in diameter when the system flies at an Above Ground Level (AGL) altitude of 600 m. At this flying altitude, the swath width is approximately 400 m. Typical flying

altitudes, scan rates, max scan angles, and laser pulse rates of 600 m, 30 Hz, $\pm 20^\circ$, and 30 kHz, respectively, provide roughly 1 laser shot per square meter on the ground. The typical performance of UF-ALSM is depicted in Table 1-1. Much higher point densities are readily achieved using overlapping flightlines, by flying lower and slower, and by using a narrower scan angle.

Table 1-1. Typical performance specifications for UF-ALSM system (a 1233 ALSM model manufactured by Optech, Inc.) prior to February 2007. This unit provided all of the LiDAR data used in this work.

Parameter	Flying height	Flying speed	Swath width	Scan rate	Laser pulse rate	Scan angle range	Data recording
Specification	600 m	60 m/s	400 m	30 Hz	33 kHz	$\pm 20^\circ$	First and last return with intensities

In order to georeference each laser return into an earth-fixed x, y, z coordinate frame, ALSM incorporates three main technologies. (1) An onboard global positioning system (GPS) receiver: Location solutions for the aircraft are determined at a rate of 1 Hz. Given a precise measurement of the physical displacement (i.e. the “lever arm”) between the sensor head and the GPS receiver, the precise position of the LiDAR sensor head can then be estimated using one or more GPS ground reference stations near the area of study. This allows differential correction of the aircraft trajectory, resulting in a root-mean-square (rms) error to within a few centimeters. (2) An inertial navigation system (INS): A Litton LN200A INS unit integrates accelerometers and horizontal and vertical gyroscopes to record the roll, pitch, and yaw of the aircraft at a rate of 50 Hz. This information is used to compute the exact orientation of the aircraft relative to the coordinate system being used. (3) Scanning laser rangefinder: The laser transmitter installed in the bottom of an aircraft sends pulses of laser light towards the ground, and laser light is

reflected from an object (terrain, building, or foliage) to the laser receiver following the reverse optical path. By timing the round-trip travel of a returned pulse between the laser transmitter, a target, and the laser receiver, the range distance is determined using the velocity of light (3×10^8 m/s). The scanning mirror inside the sensor head is used to emit the laser pulses across a wide swath along the path of the aircraft. Scan angles recorded from the scanner, together with aircraft orientation and location, are used to convert raw laser ranges into the earth-fixed coordinate frame. An illustration of an ALSM system at work is shown in Figure 1-1. The ALSM data acquired for this study were processed using Realm 3.2c (Optech, Inc.), the GPS data were processed using the kinematic and rapid static (KARS) software (Mader, 1992), and the trajectory was computed using PosPac 4.02 (Applanix).

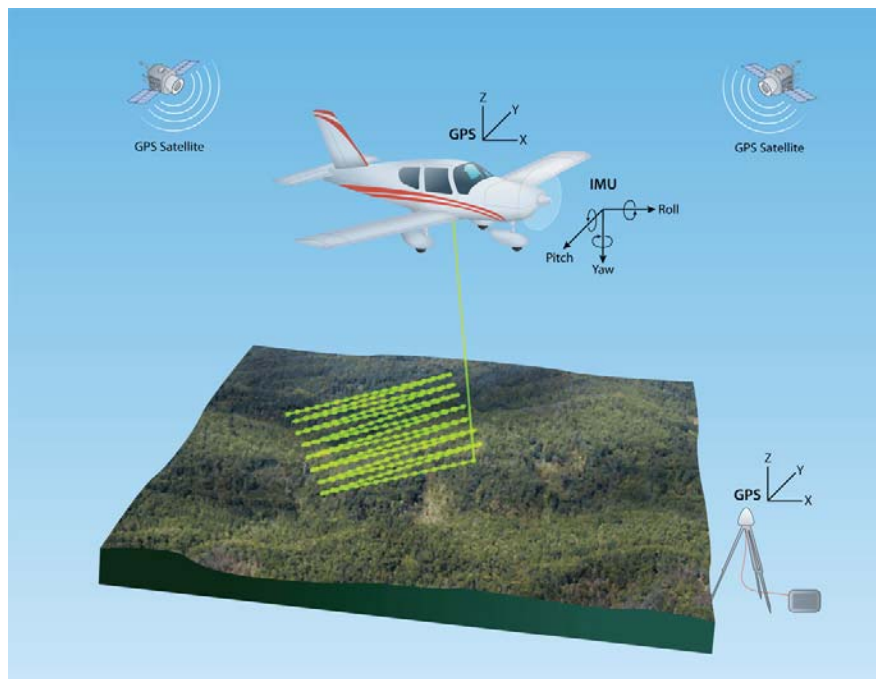


Figure 1-1. Illustration of a small footprint LiDAR system in operation, from (Roth *et al.*, 2007).

1.2 3D Airborne Laser Data over Forested Terrain

Forests are important ecosystems because they strongly modulate stores and fluxes of water and carbon near the earth's surface. Natural and managed forests also comprise an important renewable resource for the timber and paper industries. Several tree characteristics, such as stem number, density, stem volume, tree height, and canopy architecture, are of interest to forest resource managers. These parameters are utilized to estimate forest yield, describe structural characteristics for wildlife habitat, model future growth and yield, and evaluate the effectiveness of past (and need for future) silvicultural activities. Traditionally, most of these parameters have been measured using direct (*in situ*) field methods (Czaplewski, 1999). However, traditional ground-based forest inventories are expensive and time-consuming and as a result, are often limited to relatively small sample areas within the landscape of interest.

Efforts have been made to extract information about forests more efficiently using remote sensing methods. The majority of this work to date has employed multispectral (passive optical) or microwave (radar) methods. Visual interpretation from high-resolution multispectral aerial images (Brandtberg and Walter, 1998; Gong *et al.*, 2002) is often time consuming and subjective since the 2D representation in the narrow optical portion of the spectrum does not possess direct information about the 3D structure of the canopy. Radar methods have the ability to partially penetrate forest canopies, because of their longer wavelengths and widely separated frequency bands, and thus can provide some direct information about canopy density and structure (Hyypä *et al.*, 1997; Hyypä *et al.*, 2000, Slatton *et al.*, 2001). However, radar-based approaches are typically limited to spatial resolutions at the few meter scale (airborne) or few tens of meters scale (spaceborne), which are too coarse to robustly segment individual trees, making it problematic to estimate tree-based parameters from such data. Data from LiDAR systems have become more widely available in recent years for use in ecologic and forestry applications, and

these LiDAR sensors can potentially allow for accurate, precise, and automatic identification and measurement of individual trees composing the canopy (Andersen *et al.*, 2001).

For most of applications using LiDAR data, the range observations are interpolated to form 2D elevation images because one can then apply traditional image processing techniques to filter or classify the data. These images are sometimes called 2.5-dimensional maps since the laser is not capable of detecting objects hidden under opaque solid objects. However, collapsing the 3D point data into a height image early in the processing can lead to a significant loss of information when attempting to characterize landcover with structural variations in all three spatial dimensions. All algorithms in this work are developed to operate directly on the 3D raw point cloud data to avoid this information loss, which is one of the contributions in this work. By doing so, many issues associated with converting the data into 2D images, such as selecting the appropriate pixel size and an interpolation method, are avoided.

Small footprint ALSM technology can penetrate dense canopy by illuminating the ground and understory through small gaps in the crown layer. While this leads to precisely located measurements under the canopy, the fraction of laser pulses reflected back from below the canopy is small (Figure 1-2). For example, in our natural forest test site at Hogtown, which is a generally closed canopy, only about 15% of the laser returns are from the ground. The lower canopy layer just above the ground is particularly afflicted by sparse sampling with LiDAR systems that only record first and last returns, such as the system used in this work. These sparse measurements lead to a condition of undersampling where the tree stems and understory vegetation are not adequately observed. This is not critical in forests with relatively wide tree spacings, like managed forests, but can be a factor in denser natural forests. This problem can be ameliorated by estimating volumetric probability density functions (pdfs) of tree features or by

using LiDAR systems that have higher laser pulse rates and/or that record more than just the first and last returns. In this work, however, I am focused on detecting the main canopy (crown) in managed forests, and since each canopy is uniquely associated with one trunk, this issue does not pose a severe problem in this work.

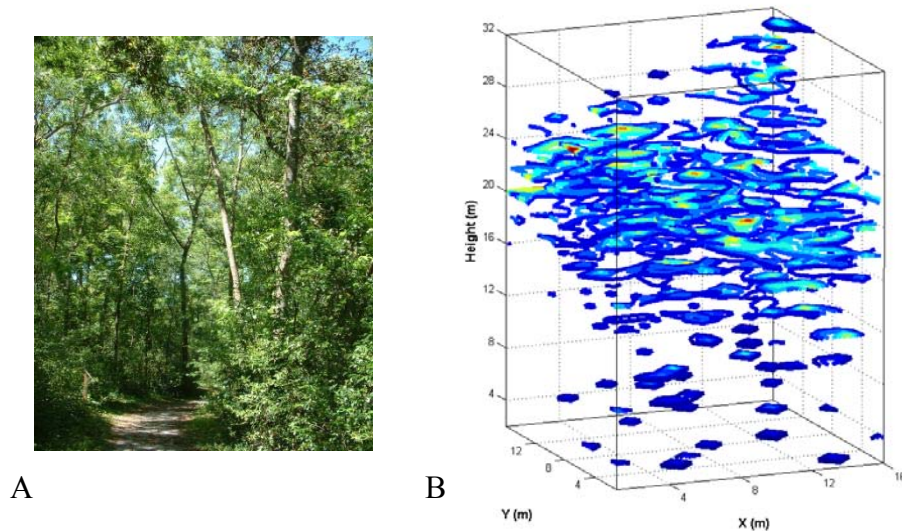


Figure 1-2. An example of undersampling in LiDAR data over a natural forest. A) An actual photograph taken from a part of Hogtown Greenway in Gainesville, FL. B) 3D probability density function (pdf) of the vegetation of the area (estimated by the Parzen windowing method and shown as a stacked contour plot for easy visualization). The LiDAR data were collected from the 33 kHz UF-ALSM. The ground returns were removed so that the pdf represents the above-ground material. Notice how the region below about 10 m exhibits lower probabilities in the pdf, yet the photograph indicates significant foliage in that region.

1.3 Organization of this Study and Contributions

Chapter 1 serves as necessary background information to the study in this dissertation. The UF-ALSM system, a small footprint discrete return LiDAR sensor, and its measurements are described. Three-dimensional point data over forests are described, and the issue of LiDAR undersampling is presented. The main contributions are also listed at the end of the chapter.

Chapter 2 describes the study site and data acquisition. The study sites, PPINES and IMPAC, are used for most of the work except in section 3.2. The study site for that section, Hogtown Greenway, is briefly explained in that section. The ALSM data and ground truth data acquisitions over the study sites are also explained.

Chapter 3 presents two geometric mapping approaches, in which the relevant LiDAR points between points of interest are isolated to find optical gaps inside forests. Firstly, a robust and simple procedure is presented for estimating IPAR. Second, a method is developed to detect walking trails in natural forests that are obscured from above by the canopy. In both of these applications, the primary structuring elements are field-of-view scope functions. While appropriate for line-of-sight estimation, these mappings are not optimal for estimating many important forestry parameters.

In Chapter 4, I describe a technique for detecting individual trees using 3D laser point data. Detecting and segmenting individual trees opens up the possibility for the direct estimation of structural parameters of paramount interest to forest managers and researchers. An adaptive clustering method is developed to merge the partial-tree clusters that are segmented by the region growing process, and the performance is compared with the scale-space method.

Chapter 5 presents results from estimating some important tree (or plot) parameters and compares the estimates with ground truth data from a field survey. The height, location, and crown length of individual trees are extracted from the segmented points. Some possible methods are introduced to compute gap distributions that are relevant to the spatial distribution of attenuation of GPS microwave signals and detectability of personnel from the sky.

In Chapter 6, a novel method for the compact representation of the geometric features of segmented LiDAR points from tree canopies is explored that uses a 3D point matching method

known as spin images. Finally, conclusions and discussion of suggested future works are presented in Chapter 7.

The main goal of this work is the development of an approach to detect individual tree canopies using 3D point data, which then allows the subsequent estimation of several important tree structural parameters. Geometric mappings, including visibility scope functions, inside forests are also developed to find optical gaps. These mappings allow the estimation of additional forest parameters, such as IPAR, and other parameters that strongly impact tactical operations, such as line-of-sight visibility and locations of obscured walking trails. Specific contributions in this dissertation are:

First, a new geometrical method for accurately estimating IPAR under forest canopies is developed. This is the first application of small-footprint discrete-return LiDAR to estimate IPAR. This is done by defining field-of-view (scope) functions between observer points in the forest and the sun that parameterize the light penetration through the canopy. These simple scope functions that isolate the relevant LiDAR reflections between observer points and the sun are shown to give good agreement between the LiDAR-derived estimates and the *in situ* values of IPAR. This idea can be extended to estimate signal attenuation for sky-ground communication or telemetry transmission.

Second, the concept of line-of-sight visibility is employed to detect walking trails in natural forests that are obscured from above by the canopy. To our knowledge, this is the first and only work using airborne LiDAR data to detect occluded forest trails. As such, there are no prior methods with which to compare. So estimated trail locations are verified using GPS data collected *in situ*. There is an absence of understory biomass on narrow irregular walking trails, but in many cases, these voids correspond to the region that is most severely undersampled by

airborne LiDAR sensors. Instead of direct detection of trails based on density variations in LiDAR point clouds, several features from the ALSM data are extracted and used to constrain the search space and infer the location of trails. The visibility vectors, as a byproduct in the process, indicate potential lines-of-fire for tactical scenarios and pathways through forested terrain that can potentially minimize traversal times.

Third, an improved method for segmenting trees in LiDAR data is developed. Unlike previous methods that gridded the LiDAR data into a height image and used image processing techniques to detect trees, the whole process is based on LiDAR point cloud data without the need for a gridding (interpolation) step. This avoids the significant loss of information associated with interpolating the 3D data to image data. Furthermore, very few works have focused on principled (non-empirical) methods for dealing with the search radius R even though R is the most important parameter in tree detection via overhead remote sensing. An adaptive clustering method, that adapts to variations in canopy shapes and sizes, is developed to merge canopy clusters initially segmented by a region growing algorithm. This contribution subsequently allows the vastly higher spatial resolution estimation of forest parameters.

CHAPTER 2 STUDY SITES AND DATA ACQUISITIONS

2.1 Study Sites

Managed forests comprise an important subset of all forests due to the economic capital invested in them and the resources derived from them. Data were collected for tree detection algorithm development at an installation of the Pine Productivity INteractions on Experimental Sites (PPINES), located in North-Central Florida (30° 14' N, 82° 18' W) (Figure 2-1). The site was established by the Forest Biology Research Cooperative (FBRC), located at the University of Florida, in January of 2000. A series of field research installations were designed to examine the interactions of full-sib (controlled ancestry) loblolly pine (*Pinus taeda* L.) and slash pine (*P. elliottii* Engelm. var. *elliottii*) families with several environmental factors, such as location, silvicultural treatment intensity, and planting density (Roth *et al.*, 2007a). The topography in North-Central Florida is generally very flat, with ground elevations in the study site varying as little as 2 m. In this work, a total of 16 plots at PPINES were selected where all plots have the same species (loblolly pine), number of planting positions in the measurement plot (48), and spacing between trees (2.74 m×2.74 m) arranged in six rows (beds) of eight trees each. A schematic layout of a typical plot is shown in Figure 2-2 (A). However, the plots are split into two different culture treatments (high and low). High cultural intensity attempts to maximize growth and health of the growing stock by understory vegetation control and fertilization.

Another managed forest, the Intensive Management Practices Assessment Center (IMPAC) (Swindel *et al.*, 1988; Jokela and Martin, 2000), located near Gainesville, Florida (29° 45' N, 82° 17' W) is used in this study (Figure 2-1). The IMPAC plots were established in January 1983 as a 2×2×2 factorial of species (loblolly pine vs. slash pine), understory vegetation control (none vs. complete and sustained), and fertilization (none vs. annual with macro- and

micronutrients). A total of 12 plots were sampled consisting of 3 replicates for each of the species by fertilization treatment combinations. The 12 plots are where the understory vegetation was controlled. Each measurement plot was 0.027 ha in size consisting of 40 planting positions on a 3.66 m × 1.83 m spacing arranged in five rows (beds) of eight trees each. A schematic layout of a typical plot is shown in Figure 2-2 (B).

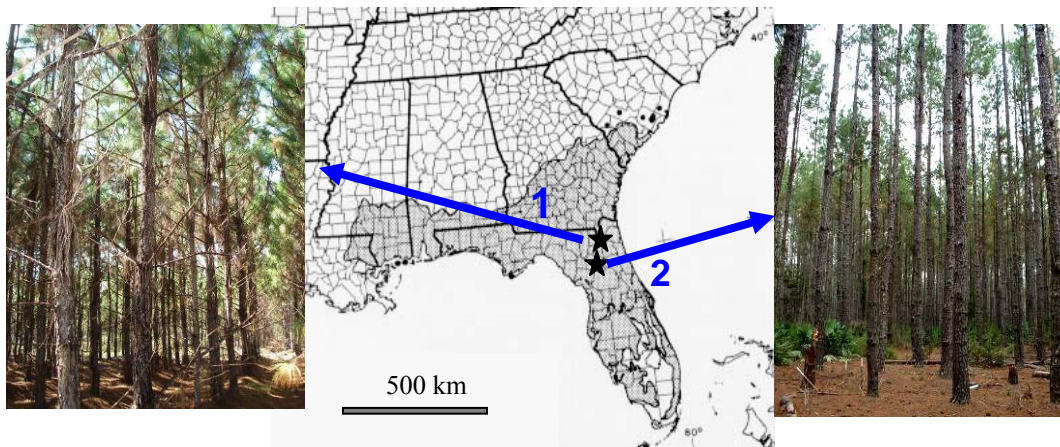


Figure 2-1. The locations of the study sites (PPINES and IMPAC) with the geographic range of slash pine shaded. The PPINES site is denoted by #1, and the IMAC site is denoted by #2.

The biophysical parameters for the trees in each site are listed in Table 2-1. Over the 16 PPINES plots, the trees averaged 7.9 m tall with a live crown length of 5.5 m. Over the 12 IMPAC plots, the average tree height was 21.3 m and the average live crown length was 6.2 m. Due to their advanced stage, the tree stands at IMPAC are at or near maximum carrying capacity, resulting in significant tree mortality in some of the plots. As a result, the number of trees, tree heights, and the sizes of canopies at IMPAC vary significantly. Unlike the conical shape of crowns in PPINES, the trees in IMPAC exhibit a wider range of shapes. The percentage of living trees (relative to those originally planted) in PPINES is 91.8 %, and 65.6 % in IMPAC. So even

in a single pine plantation, there can be significant variability in canopies, especially in older plots. Thus, an adaptive segmentation approach is needed, even for managed forests, to capture such variations within and across different sites. A top view of LiDAR data of a typical plot from each culture treatment is shown in Figure 2-3.

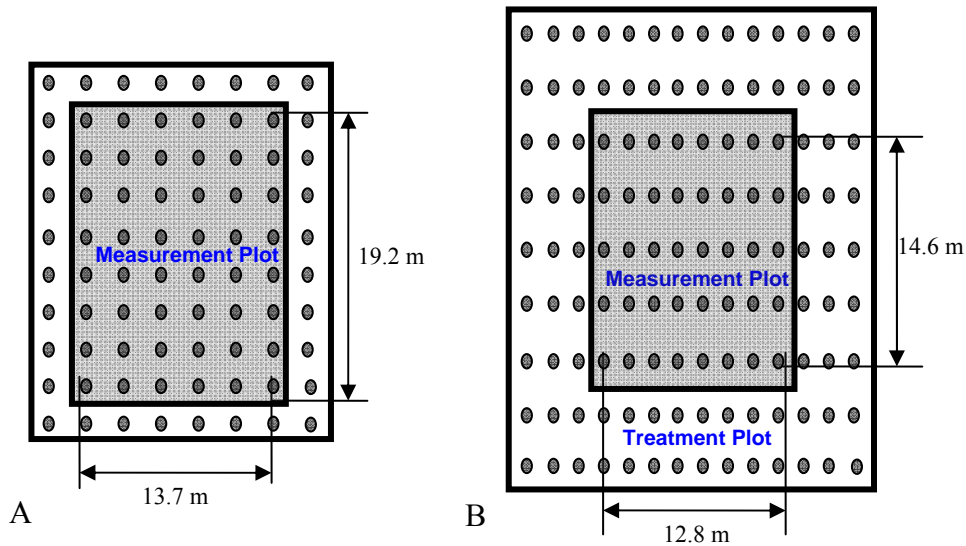


Figure 2-2. A schematic layout of a single plot from each study site, (A) PPINES and (B) IMPAC. Shaded circles indicate approximate stem locations. Dimensions of the inner measurement plot (shaded) are shown.

Table 2-1. February, 2006 *in situ* field data from across the study sites describing general information about the sites. The trees at PPINES were 6 years old, and those at IMPAC were 23 years old at the time of the investigation. The number of planted trees was 48 in PPINES and 40 in IMPAC for each measurement plot. Here, Lob = Loblolly pine, Slash = Slash pine, H = high culture, L = low culture. The tree dimensions (tree height and crown length) are written in the order of the maximum, mean, and minimum from the top in each case.

Site	Tree Species	Treatments	Number of Plots	Number of Living Trees	Tree Height (m)	Crown Length (m)
PPINES	Lob	H, L	16	705	10.7 m	7.9 m
					7.9 m	5.5 m
					4.4 m	2.9 m
IMPAC	Lob, Slash	H, L	12	315	26.1 m	15.8 m
					21.3 m	6.2 m
					10.0 m	0.9 m

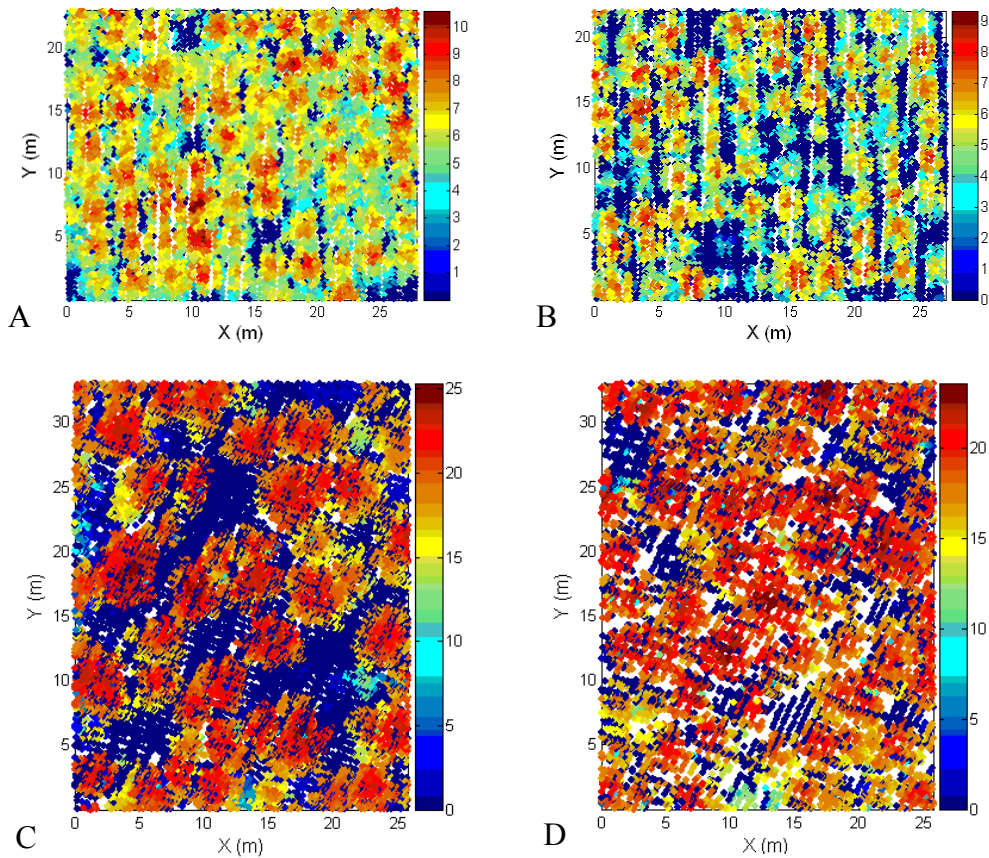


Figure 2-3. Top view of first-stop LiDAR point heights of a typical plot from each cultural intensity at each site. A) High culture at PPINES. B) Low culture at PPINES. C) High culture at IMPAC. D) Low culture at IMPAC. All units are in meters. Elevations represent relative heights above the ground. Variable point densities across the LiDAR data sets are primarily due to differences in scan angle and multiple flights overlap.

2.2 Ground Truth and ALSM Data Acquisitions

Ground surveys were performed in February 2006 for both sites to record the tree heights (HT) and the length of live crown (CL). The height to the base of the live crown was measured directly in the field and crown length was then interpreted as the difference between total height and height to the base of the live crown. The ground surveys and high-resolution aerial imagery were used to verify the individual tree segmentation results in Chapter 4 and estimates of HT and CL in Chapter 5. The aerial imagery was acquired simultaneously with the LiDAR data. Because

the objective here is to explore the degree to which information can be extracted from LiDAR data to segment trees, I only use the aerial imagery to aid in validation and not in the actual segmentation.

LiDAR data was collected as close in time to the ground surveys as possible. Collection of *in situ* and remotely sensed data at the same time is always the ideal, but we expect only negligible canopy differences if they are collected during the same year and season. However, one may generally expect considerable canopy changes if measurements are taken during the same season but in a different year, especially if the site has young fast-growing trees, or during different seasons, especially for deciduous trees. The LiDAR data used in Chapter 4 and 5 were acquired by the UF-ALSM system on March 09, 2006. Both the first and the last returns were recorded, and each laser return is the result of laser photons reflecting from the ground or foliage back up to the ALSM receiver optics. The first returns tend to reflect more from the top canopy, and the last returns reflect more from the understory and the ground. High laser point densities are generally required to robustly detect individual tree crowns. Given that the maximum available laser pulse rate was 33 kHz for these acquisitions, the flight plans were configured for dense coverage. To achieve high point densities, the LiDAR data was acquired from a relatively low AGL altitude of 350 m with a reduced scanner angle range ($\pm 10^\circ$ maximum deviation from nadir) and a 45 Hz scan rate. The maximum allowable scan angle of the sensor is $\pm 20^\circ$, but half that value was used to minimize the possibility of laser pulses passing through multiple trees. The average point densities over the study sites were 14.2 points/m² for PPINES and 10.6 points/m² for IMPAC, but the point density in each plot varied from 12 to 18 points/m² for PPINES and 8 to 20 points/m² for IMPAC due to variations in overlap among the multiple flight lines and the particular scan angle.

2.3 Preprocessing

Most studies employing small-footprint laser altimetry to date have focused on surficial mapping. In those analyses, segmentation algorithms are usually applied to estimate the bare surface elevations by “filtering out” returns from the vegetation using empirical thresholds on height variance or spatial connectedness of points (Weed *et al.*, 2002; Haugerud *et al.*, 2003; Zhang *et al.*, 2003). An adaptive multiscale filter developed by Kampa and Slatton (2004) is employed to separate the laser returns corresponding to the ground from those corresponding to the above-ground biomass. The filter employs an information-theoretic hierarchical data segmentation scheme. First, the area is classified into heavily vegetated and minimally vegetated cells. Then, a Gaussian mixture model (GMM) is estimated from the vertical histogram of aggregated last return points. An asymmetric decision rule is applied to the GMM to ensure that the probability of missing a ground return is less than the probability of erroneously admitting a non-ground return in the bare surface estimate. This decision rule is used to capture small-scale surface features, such as scarps and stream banks. This filter avoids empirical thresholding on the point distributions and retains the 3D “point cloud” data format. Figure 2-4 shows the ground laser points segmented by the filter and the resulting estimated ground surface at the IMPAC site. Both study areas are relatively flat, so the terrain slope and height are not a factor for this work. However, to remove the contribution of the terrain slope and heights for arbitrary sites, the low order (slowly varying) terrain surface is subtracted from the LiDAR points to “level out” the ground. The flattened laser points are shown in Figure 2-5.

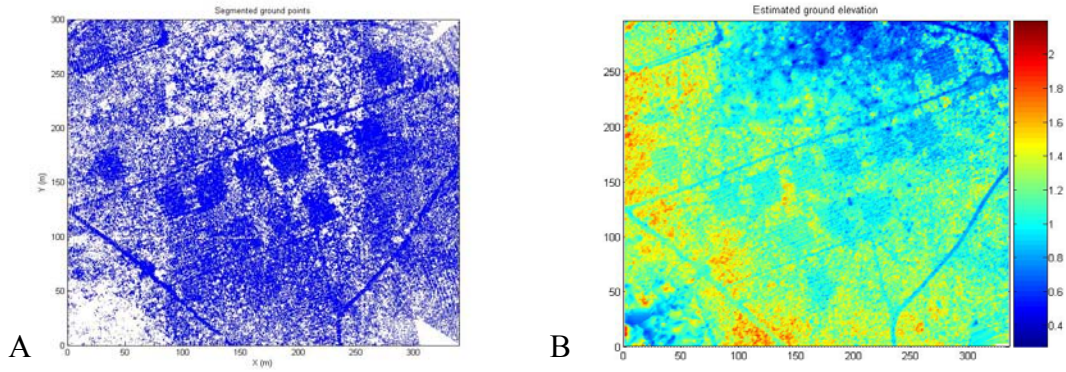


Figure 2-4. Segmented ground laser points and the estimated ground elevation at the IMPAC site. A) Segmented ground laser points. B) Estimated ground elevation surface. All units in meters.

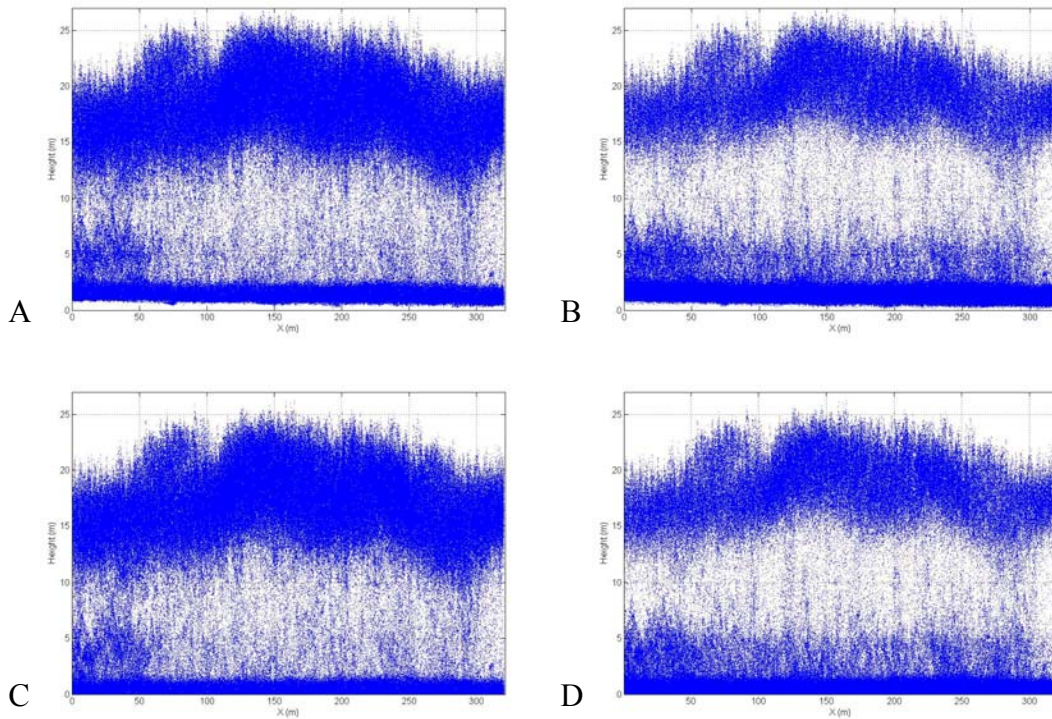


Figure 2-5. Raw and flattened first/last stop elevation points. A) Raw first stop elevation points. B) Raw last stop elevation points. C) Flattened first stop elevation points. D) Flattened last stop elevation points.

CHAPTER 3 FIELD OF VIEW GEOMETRIC MAPPINGS

3.1 IPAR Estimation

The amount of light intercepted by forest canopies plays a crucial role in forest primary production. However, the photosynthetically active part of this intercepted solar radiation (IPAR) is difficult to measure using traditional ground-based techniques. *In situ* measurement of IPAR requires labor-intensive field work, often resulting in limited datasets, especially when collected over extensive areas. Remote sensing methods have been applied to the estimation of light interception in forests, but until recently have been restricted to two-dimensional (2D) image data. These approaches do not directly account for the three-dimensional (3D) structure of forested canopies, and therefore predicting IPAR for arbitrary sun positions is problematic. I utilized a 3D point cloud dataset acquired via an airborne laser ranging (LiDAR) system to predict *in situ* measured IPAR. This was achieved by defining a ‘field of view’ (scope) function between observer points just above the forest floor and the sun, which relate IPAR to the LiDAR data over Southern pine experimental plots containing a wide range of standing biomass. A conical scope function with an angular divergence from the centerline of $\pm 7^\circ$ provided the best agreement with the *in situ* measurements. This scope function yielded remarkably consistent IPAR estimates for different pine species and growing conditions. IPAR for loblolly stands, which have diffuse canopy architecture, was slightly underestimated.

3.1.1 Motivation

Forest productivity is generally a function of leaf area index (LAI), as is well documented for Southern pine forests (McCrary and Jokela, 1998; Jokela and Martin, 2000; Martin and Jokela, 2004; Samuelson *et al.*, 2004). Light attenuation through the canopy depends strongly on the amount of foliage in the stand (Gholz *et al.*, 1991; MacFarlane *et al.*, 2003), and therefore it

is not surprising that net forest productivity has been positively and linearly related to the amount of photosynthetically active radiation (PAR) that is absorbed or intercepted by canopies (Monteith, 1972; Dalla-Tea and Jokela, 1991; McCrady and Jokela, 1998). The quantity of PAR that is intercepted (IPAR) is largely determined by the amount of foliage in the canopy as well as its orientation (Colbert *et al.*, 1990; McCrady and Jokela 1996; Landsberg and Gower, 1997; Kucharik *et al.*, 1998). However, the ability of trees to support leaf area and intercept light decreases with environmental stresses (Waring and Schlesinger, 1985; Hebert and Jack, 1998), such as soil nutrition and water limitations. The relationship between leaf area and light interception may also be modified by stand developmental processes (Martin and Jokela, 2004). Leaf area and incident radiation have been successfully used to regionally model loblolly pine productivity across the Southeast United States (Sampson and Allen, 1999) and are the key drivers in process-based models of forest productivity (Wang and Jarvis, 1990; Cropper and Gholz, 1993; Battaglia and Sands, 1998; MacFarlane *et al.*, 2003). However, IPAR estimates across the landscape are limited by a lack of available radiation measurements, which are the most sparsely measured of routine climatologic data (Aber and Freuder, 2000).

Traditional measurement of IPAR is time consuming, which is problematic given the changing light conditions throughout the day. The light incident on a particular forest canopy is constantly changing in both direction and intensity (Gay *et al.*, 1971). As a result, the proportion of intercepted radiation may need to be corrected to a constant sun angle from zenith in order to facilitate repeated measurements through time (Will *et al.*, 2005). Additionally, Southern pine foliage exhibits strong seasonal dynamics and rapid responses to altered nutrition (Gholz *et al.*, 1991), thus requiring frequent measurement of IPAR. As an alternative, remote sensing methods have been utilized to estimate canopy parameters, such as LAI, that are related to sunlight

penetration through the canopy. However, since the sun constantly changes position and forest canopies exhibit strong 3D structural variations, it is not sufficient to estimate PAR from traditional 2D data, such as multi-spectral imagery (Butson *et al.*, 2002) or polarimetric synthetic aperture radar (Saatchi *et al.*, 1994). Explicit 3D structural information is needed to predict sunlight transmission for different sun angles. While interferometric synthetic aperture radar (InSAR) can provide some 3D information, it is generally of insufficient spatial resolution to adequately measure stand-level variations (Slatton *et al.*, 2001). Airborne light detection and ranging (LiDAR) systems on the other hand can provide both high spatial resolution and canopy penetration in a 3D point cloud format. For example, airborne LiDAR measurements have been reliably related to *in situ* measurements of individual tree and stand structure (Holmgren *et al.*, 2003; Lim *et al.*, 2003; Maltamo *et al.*, 2004; Farid *et al.*, 2006), and has also been used to successfully estimate IPAR for maize and sunflower crops (Holdcroft *et al.*, 2005). For this investigation, I show that it is possible to directly exploit the 3D nature of LiDAR data to estimate sunlight intercepted by the forest canopy while accounting for variations in sun angle.

A few investigators have begun to analyze the 3D measurements of forest structure from small-footprint LiDAR (Eggleston *et al.*, 2000; Todd *et al.*, 2003). Todd *et al.* (2003) attempted to estimate indicator probabilities for different “surfaces” representing different vertical strata in the canopy, such as overstory, middle canopy, and lower canopy. Their approach involved interpolation of point data into surfaces and the *a priori* assumption of a preferred geometric shape for local distributions of points in canopies. They used a small-footprint LiDAR operating at an altitude of 750 m above ground, with a laser pulse rate of 20 kHz and a scan angle range of $\pm 15^\circ$, which produced 400 m wide swaths with a stated density of 8662 laser pulses per hectare (0.87 pulses per square meter). In this work small-footprint LiDAR data was acquired on

October 11, 2005 by UF-ALSM system, flown at 450 m AGL with a laser pulse rate of 33 kHz, scan rate of 30 Hz, and a scan angle range of $\pm 18^\circ$, resulting in a nominal laser shot density of 1.83 transmitted pulses per square meter on a single pass. Both first and last returns from each pulse are used to maximize sampling of the canopy. This configuration was used because I found that LiDAR sample densities on the order of a few per square meter were required to reliably resolve the 3D distribution of forest canopy for accurate estimates of IPAR. This sub-meter sampling supports the direct representation of the canopy as a point cloud rather than as a set of interpolated surfaces.

The overall objective of this work is to demonstrate a simple procedure for the estimation of IPAR in loblolly and slash pine plantations at the IMPAC site using airborne LiDAR remote sensing measurements. Specifically, I determined that a single parametric ‘field of view’ (scope) function can be found that enables reasonable estimates of IPAR across the set of widely varying canopy conditions studied in this trial.

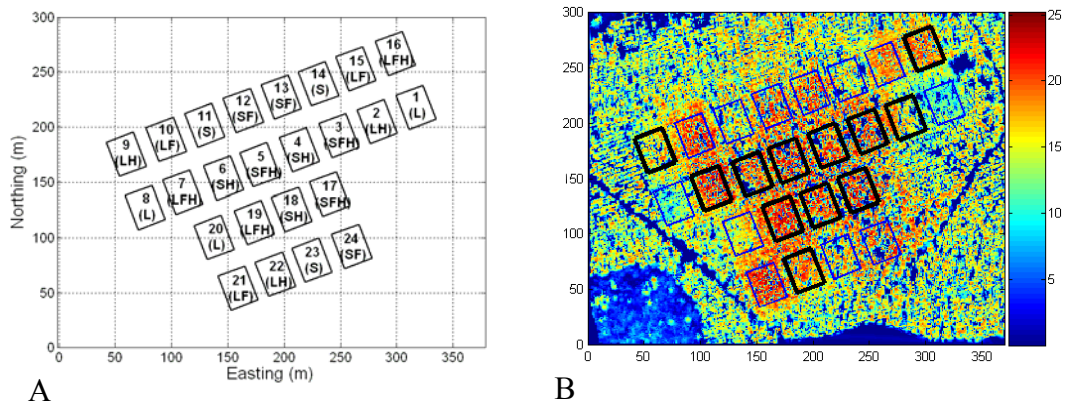


Figure 3-1. The spatial arrangement of the plots in the IMPAC site. A) The spatial arrangement of the 24 plots in the IMPAC study (plot codes: L = Loblolly, S = Slash, H = complete understory vegetation control, and F = Fertilized). B) Color-coded elevation (above local ground) image derived from ALSM data (all units in meters). The 12 plots outlined in bold correspond to those used in this study (plots 2, 3, 4, 5, 6, 7, 9, 16, 17, 18, 19, and 22).

3.1.2 Estimation of *In-Situ* IPAR

In this work, the same 12 plots in the IMPAC site in Chapter 2 are used. The details of the spatial arrangement of the plots and the selected plots are shown in Figure 3-1. A summary of tree survival and solar angles at the time of measurement for each plot is provided in Table 3-1. Sun position was defined in terms of two angles, θ (the angle from the easterly direction to the nadir projection of the observer-sun vector in the horizontal plane) and ϕ (the elevation angle of the sun above the horizon along the zenith), relative to the observation point at the origin of a translating (local) spherical coordinate frame (Figure 3-2).

Table 3-1. Plot level inventory data detailing tree survival and solar angles at the time of the *in situ* PAR measurements. Data was collected in October 2005. A total of 40 trees were planted on each measurement plot in 1983. See Figure 3-2 for a visualization of sun angles, which are expressed in degrees.

Species	Fertilized	Plot	Survival (no. of trees)	Sun Angles (ϕ , θ)
Loblolly	No	2	38	(45, 55)
		9	29	(49, 69)
		22	27	(51, 98)
	Yes	7	25	(49, 67)
		16	35	(41, 48)
		19	28	(51, 95)
Slash	No	4	29	(44, 53)
		6	30	(47, 63)
		18	29	(51, 92)
	Yes	3	19	(43, 51)
		5	27	(47, 61)
		17	18	(51, 88)

Multiple techniques have been used to estimate the amount of PAR intercepted by forest canopies. The most common method is to estimate PAR incident at the top of the canopy and relate it to PAR incident below the canopy under uniform conditions (clear-sky or overcast) centered on solar zenith (Messier and Puttonen, 1995). Many types of sensors have been

employed to quantify the light environment under forest canopies, such as radiometers, photosensitive paper or chemicals, hemispherical canopy photographs, plant canopy analyzers, or visual estimators of canopy density (Leiffers *et al.*, 1999). For the results reported here, *in situ* measurements of IPAR were made using a combination of a LiCor LI-190 Quantum PAR sensor (LI-COR inc., Lincoln, NE) and an integrating PAR ceptometer (AccuPAR Linear Par Ceptometer, Model PAR-80, Pullman, WA). The AccuPAR is a battery-operated linear PAR ceptometer containing 80 independent photodiodes, spaced 1 cm apart. The photodiodes measure PAR in the 400-700 nm spectral band in units of micromols per meter squared per second ($\mu\text{mol m}^{-2}\text{s}^{-1}$). The hemispherical field of view (FOV) was directed upward.

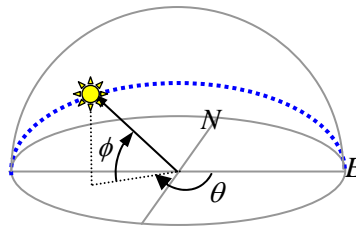


Figure 3-2. Solar angles (θ, ϕ) defined relative to an observer point at the origin of a local spherical coordinate frame. The elevation angle of the sun above the horizon along the zenith is defined as ϕ , while the angle from the easterly direction to the nadir projection of the observer-sun vector in the horizontal plane is defined as θ . All angles are reported in degrees. Local zenith is at $(\theta, 90^\circ)$.

Above canopy incident PAR (background) was collected using the LiCor LI-190 Quantum sensor which was placed in an open area adjacent to the study site. Concurrent below canopy PAR samples were collected over two measurement periods on October 16, 2005, using the integrating PAR ceptometer during a period of 2 hours centered about local solar zenith. At regular intervals during the sampling period side by side estimates were made in the open (background) to ensure concurrence between the two sensors. Observations were taken during

clear sky conditions to minimize contributions due to diffuse sky irradiance. The sun angle was noted during each *in situ* collection so that the corresponding sunlight penetration could be computed from the ALSM data. Ground measurements were collected from nine systematic transects spanning the width of each measurement plot (18.3 m) at a height of 1.5 – 2 m. Sixteen light readings were taken along each transect and averaged to generate a single *in situ* data point per plot for each of two measurement periods. *In situ* IPAR was computed using equation 3-1 with the average IPAR per plot computed from the average of the two readings ($J = 2$)

$$IPAR_{in\ situ} = \frac{1}{J} \left[\sum_{j=1}^J \left(1 - \frac{Ceptometer(j)}{Background(j)} \right) \right], \quad (3-1)$$

where $IPAR_{in\ situ} \in [0,1]$ since the intercepted sunlight flux is non-negative and the below canopy value does not exceed the open sky value.

3.1.3 Isolating the Vegetative Contribution to IPAR

Spatial variations in the sunlight flux through forest canopies are, in general, governed by local topography, latitude (sun angle), meteorological conditions (e.g. cloudiness, water vapor), and the amount and distribution of occluding vegetation. In this work, I am interested in capturing the contributing effects of vegetation, so a low-relief test site was chosen with a wide range of standing biomass. In order to relate the distribution of vegetation to ALSM observations, I first separated laser light interception by the ground surface from that of the non-ground objects by using the adaptive multiscale filter in section 2.3. While it was possible that some vegetation returns near the ground may have been included in the segmented ground points, the probability was minimized in this investigation since the data collection was limited to the areas where the understory vegetation had been removed.

To further reduce the probability of misclassifying ground points as non-ground points (i.e. vegetation), all points less than 1 m above the estimated ground surface were removed from consideration by assuming that the total error (system error + surface estimation error) was less than or equal to 1 m. This 1 m buffer is reasonable since field validation revealed that the Root-Mean-Square (RMS) error in the estimated ground surface under the canopy was much less than 1 m near ALSM points. Since that error can be larger (still less than 1 m) in small data voids where dense crowns prevent ALSM points from reaching the ground, the ALSM IPAR estimates are computed for an observation height of 2 m to correspond to the *in situ* IPAR measurement height.

3.1.4 Optical Scope Functions

Incident sunlight flux between the sun and a hypothetical observer under the forest canopy was determined by defining an optical field of view (scope function) for the observer. The scope functions originated at the observer and extended through the canopy in the direction of the sun. I examined a combination of cylindrical and conical geometries consisting of four unique scope functions: 1) a simple cylinder of 40 m in length, 2) a simple cone, 3) a cone weighted by the distance between the ALSM point and the observer, and 4) a cone weighted by both the distance between the ALSM point and the observer and the angular divergence from the conical centerline (Figure 3-3). Secondary to this, within each function, five unique sizes were defined: diameters of 2 m, 3 m, 4 m, 5 m, and 6 m for the cylinder and $\pm 5^\circ$, $\pm 7^\circ$, $\pm 10^\circ$, $\pm 15^\circ$, and $\pm 20^\circ$ angular divergences α from centerline for each of the conical functions. The choice of cylinder length was dependent upon the dominant tree height and the sun angles represented in the study area at the time of the investigation. In order to minimize computations, the shortest length that included all ALSM laser points was chosen. Since the tree height in the study area was generally less than 30 m and the sun angle greater than 40° , a 40 m cylinder length was utilized.

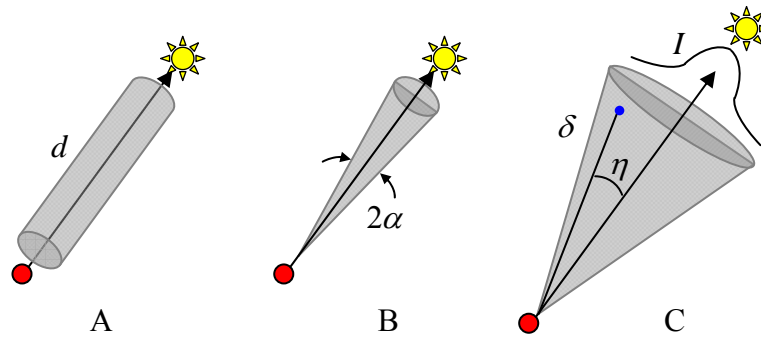


Figure 3-3. Different types of scope functions investigated. A) Cylinder scope function with diameter d . B) Cone scope function with angular divergence α . C) A weighted cone scope function, where δ is the distance from an ALSM point in the scope (blue dot) to the observer, η is the angular deviation of that ALSM point from the center line, and I is a truncated Gaussian irradiance distribution across the field of view.

The weightings for the conical functions took two forms. In the first case, the occluding effect of a LiDAR point was weighted only by the distance δ between that point and the observer. I required the function, w_δ , decrease monotonically with δ . It was also desirable to have a function with compact support to enforce upper and lower limits on the occluding effect. Maximum occlusion ($w_\delta=1$) occurs when the LiDAR reflector is located at the observer point ($\delta=0$). Zero occlusion ($w_\delta=0$) occurs when the point in the scope is farther than $\delta_{\text{vanishing}}$ from the observer. The function must also be nonlinear to accommodate the optical property that an object's occluding effect becomes less sensitive to changes in its distance from the observer as that distance increases. A second order polynomial is the simplest such function that gives a “graceful” decline in w_δ as δ approaches $\delta_{\text{vanishing}}$ by ensuring that derivatives up to 1st order remain continuous (Figure 3-4). The choice of $\delta_{\text{vanishing}}=100$ m is simply a conservative bound on the maximum expected path length from the observer to the canopy top given that canopies at the

study site were all less than 30 m tall and that sun elevation angles of less than 20° are generally not of interest for IPAR studies.

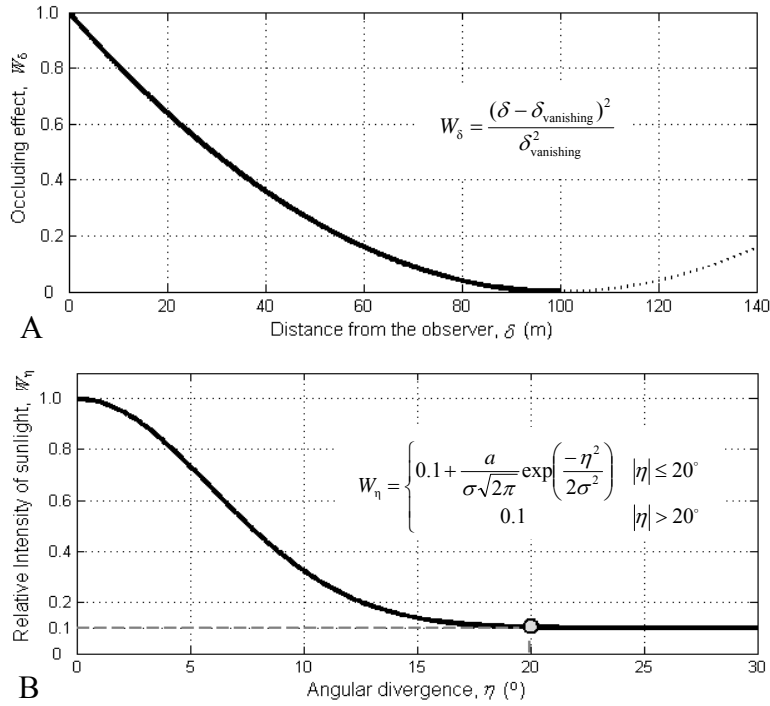


Figure 3-4. The weighting functions for the cone scopes. A) The quadratic occluding effect weighting function w_δ with respect to distance from the observer. B) The truncated Gaussian weighting function w_η with respect to angle from the line of sight, where $\sigma = 6^\circ$ and the scale factor $a = 13.5$.

In the second case, the occluding effect of an ALSM point relative to the observer was weighted by both its distance from the observer δ and its angular divergence η from the cone centerline. I followed similar reasoning for the η weighting as for the δ weighting. Namely, I wanted a function, w_η , that monotonically and continuously decreased from a maximum value at the scope centerline as a function of η to a minimum value at the cone's edge. This occluding effect should be approach the cone edge in a smooth manner (continuous up to 1st order

derivative), but it should not strictly reach zero at the cone edge since there can still be some occluding effect as long as the object is in the field of view. The function should be nonlinear to accommodate the optical property that an object's occluding effect becomes less sensitive to changes in its divergence angle as the divergence increases. A truncated Gaussian distribution was therefore used as a simple parameterization for the angular weighting of the sunlight intensity (relative irradiance). The Gaussian was preferred over a quadratic for w_η because it corresponded more closely to observations of direct solar irradiance versus angle (Halthore *et al.*, 1996). The η weighting has the following characteristics, as depicted in Figures 3-3 and 3-4: (a) the effective intensity of the sun's radiation I follows a Gaussian distribution from centerline up to $\pm 20^\circ$ and (b) the minimum intensity is reached at 20° and maintains a constant value of 0.1 for larger angles. The η and δ weighting functions were applied to each ALSM point inside a given scope so that the maximum total weight was 1.0 and the minimum was 0. In the case here, the minimum total weight never reached 0 since the maximum scope length δ_{\max} of 40 m was less than $\delta_{\text{vanishing}}$.

3.1.5 Estimation of IPAR from ALSM

For each scope function, the point densities of non-ground laser returns inside the scope, originating 2 m above the ground surface, were computed. Since the type of scope function used was fixed for a given IPAR estimate over the study area, and therefore the volume of the scope was fixed, LiDAR point densities were computed simply by counting the number of non-ground laser returns inside the scope. Each scope function was given a constant orientation towards the position in the sky that the sun occupied during the corresponding *in situ* data collection. This procedure was iterated across each measurement plot in 1 m horizontal grid increments. The sun's angular position was computed for each ALSM estimate using the latitude and longitude of

the study site in combination with the date and time of the ground truth measurement (Giesen, 2005; Gronbeck, 2005). This allowed for a direct comparison between *in situ* measured IPAR, $IPAR_{in\ situ}$, and ALSM estimated IPAR, $IPAR_{ALSM}$.

Since ALSM point clouds consist of irregularly spaced samples, with each location in the imaged area having variable point densities, the IPAR estimates derived from ALSM data were normalized by the local point density. The variation in point density in this study was small due to the fact that data from a single flight line was used. However, normalizing by point density would be crucial when working with LiDAR data sets composed of mosaics of multiple and partially overlapping flight lines. I utilized a simple normalized functional mapping algorithm in order to estimate $IPAR_{ALSM}$ from the point density of LiDAR returns corresponding to the canopy at a specific observer point, denoted by i , in equation 3-2:

$$IPAR_{ALSM}(i) = \frac{\ln(\rho_i + 1)}{\max_{i \in \{1, 2, \dots, M\}} \ln(\rho_i + 1)} \quad (3-2)$$

where ρ_i is the number of the ALSM non-ground points inside the scope at the i^{th} location where each point's contribution has been weighted as described in section 3.1.4, and M is the total number of $IPAR_{ALSM}$ calculations over the entire study site.

The number of ALSM points ρ in the scope function can in general vary from zero to some finite but large number L , which is not known *a priori*. $IPAR_{ALSM}$ was computed across the entire 370 m \times 300 m study area in order to thoroughly sample the local foliage densities for normalization purposes (i.e. the denominator in equation 3-2). The effective $IPAR_{ALSM}$ for each measurement plot was then computed as the average of all $IPAR_{ALSM}(i)$ within that measurement plot.

The simple nonlinear relationship in equation 3-2 was defined as a continuous-valued dimensionless measure bounded by 0 and 1, which could be used for comparisons with $IPAR_{in\ situ}$ in equation 3-1. While a linear scaling, such as $\rho/\max \rho$, could provide a linkage between $\rho \in [0, L]$ and $IPAR_{ALSM} \in [0, 1]$, the logarithm provided the desired property that small differences in ρ would have significant impact on the calculation for ρ small but little impact for ρ large. Normalizing by the maximum value provides the unity upper bound. The arctangent could also have been used, which would have provided somewhat similar results. However, in that case the upper bound would have been fixed (no longer dependent on L) and therefore not related to the distribution of foliage in the study area in the same way that $IPAR_{in\ situ}$ was. The exact manner in which true IPAR increases as a function of foliage density is not generally known since it depends upon the particular arrangement and spectral absorbance of occluding objects, such as stems, branches and clumps of foliage. The goal of this investigation was to derive a set of simple scope functions with minimal parameterization and empirical calibration, such that they could be employed across a wide variety of forest types and conditions.

3.1.6 Results

$IPAR_{ALSM}$ was calculated across the 12 plots using all combinations of the 4 scope functions and 5 dimension classes, which resulted in 240 estimated values. The most appropriate overall scope function and dimension was selected by comparing the residuals between the estimated $IPAR_{ALSM}$ and the *in situ* measured IPAR for each plot. Analysis of Variance (ANOVA) was performed on this dataset of residuals using SAS software (SAS Institute Inc., 2000). The best combination of scope function and dimension was selected using the LSMEANS option in the PROC GLM procedure. The PROC REG procedure was used in SAS in order to

quantify the strength of the relationship between observed and estimated values of IPAR. I tested for the need for different equations for the main effects of species and fertilization using the one-way fixed group model. Differences among the treatments for *in situ* and ALSM derived IPAR were tested using ANOVA via the PROC GLM procedure in SAS. Separation of means analysis was done using the LSMEANS procedure in SAS.

3.1.6.1 Selection of the Best Scope Function

Analysis of variance indicated that there were large differences between scope functions in their ability to predict IPAR ($p < 0.0001$). The performance was dependent on the physical dimensions as well as the shape of the scope functions. In Figure 3-5, the average absolute error is plotted for each scope function. The smallest residuals for the cylindrical function occurred when a radius of 2.5 m was used. Based on the average absolute difference values, I found that the conical scope functions have the advantage of yielding smaller maximum errors (no greater than 0.17) than the cylindrical scope function (0.33) for a wide range of angles and weights. In the case of the conical scopes, I found the strongest dependence to be on the divergence angle α . An angle of $\alpha = 7^\circ$ yielded the minimum mean squared error between $IPAR_{ALSM}$ and $IPAR_{in\,situ}$ regardless of weighting by distance δ and/or angle η . Thus, relatively narrow conical scope functions performed best overall, and within such scope functions, the position of individual ALSM points had a relatively weak effect on the IPAR estimate. This angle, $\alpha = 7^\circ$, produces a cone with a diameter of 6.2 m where it intersects the approximate middle of the canopy, given that the average tree height is 21.3 m and the average elevation sun angle ϕ was 45° . Interestingly, this diameter is the same as the average crown length in the study site. Future investigation on other sites may find a connection between the angle α and the average crown length in the ROI.

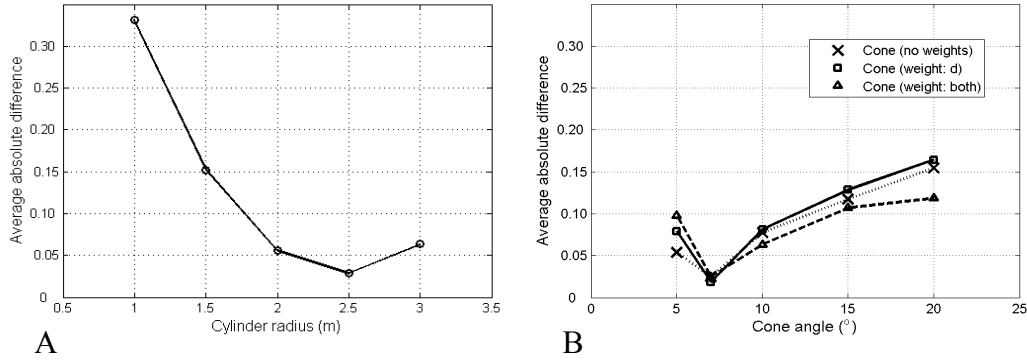


Figure 3-5. Residual analysis comparing the two types of scope functions as dimensions change, where average absolute difference is simply the average absolute value of ALSM IPAR estimates minus *in situ* IPAR measurements. A) Cylinder scope function performance with respect to diameter. B) Performance of three different cone scope functions with respect to angular divergence. The conical scope function with an angle of 7° yielded the best overall estimates.

In terms of the sign of the error, I found that for the cylindrical functions, all radii less than 2.5 m resulted in underestimates of $IPAR_{ALSM}$ and radii greater than 2.5 m resulted in slight overestimates. For conical functions, small divergence angles ($\alpha \leq 5^\circ$) led to a slight underestimation of $IPAR_{ALSM}$, while large divergence angles ($\alpha \geq 10^\circ$) led to an overestimation of $IPAR_{ALSM}$. Although the underestimation of $IPAR_{ALSM}$ for small α and overestimation for large α were relatively small, the fact that those trends were consistent for all weighting schemes suggests that omitting indirect sky irradiance may have been the cause.

3.1.6.2 Variation in IPAR

Analysis of variance for both $IPAR_{ALSM}$ and $IPAR_{in situ}$ demonstrated a significant interaction between species and fertilization ($p = 0.0276$ and $p = 0.0957$ respectively) (Table 3-2). Fertilized loblolly pine intercepted the most light, while non-fertilized loblolly intercepted the least (Table 3-3). Fertilization did not have a statistically significant influence on light

interception in the slash plots, although fertilized slash pine intercepted slightly less light than non-fertilized. I used the cone function with $\alpha = 7^\circ$ and weighted by distance because, as can be seen in Figure 3-5, that gave the minimum average absolute error.

Table 3-2. Analysis of Variance (ANOVA) table for *in situ* and estimated IPAR. *p*-values in bold are considered statistically significant at alpha less than or equal to 0.1. Degrees of freedom and mean squared residual are represented by df and MS respectively.

Source of Variation	df	<i>In situ</i>		ALSM Estimate	
		MS	<i>p</i> -value	MS	<i>p</i> -value
Species (S)	1	0.000108	0.8113	0.001800	0.3864
Fertilization (F)	1	0.002945	0.2334	0.003924	0.2132
S×F	1	0.012805	0.0276	0.007650	0.0957
Error	8	0.001772		0.002145	

Table 3-3. Least Squares estimates of IPAR measured *in situ* and estimated from ALSM. Using Bonferroni's Least Significant Difference (LSD), differences between *in situ* and ALSM values in all four rows are not significant at alpha equal to 0.05. The cone function with $\alpha = 7^\circ$ and weighted by distance is used in this analysis.

Species	Fertilized	<i>In situ</i>	ALSM
Loblolly	Yes	0.735	0.705
Slash	No	0.698	0.693
Slash	Yes	0.664	0.679
Loblolly	No	0.639	0.618

3.1.6.3 Residual Analysis

Overall the strength of the relationship between observed and predicted values of IPAR was strong, however, regression analysis determined that a bias in the prediction of remotely sensed estimates of IPAR existed between species. While there was no difference between the slopes of the equations between species ($p = 0.4850$), there was a significant difference between

intercepts ($p = 0.0094$). Using the cone function with $\alpha = 7^\circ$ and weighted by distance, IPAR for loblolly pine was slightly underestimated by the ALSM, however, slash pine was very close to the 1:1 line between observed and predicted (Figure 3-6). The relatively small residuals are considered encouraging given the minimal parameterization of these scope functions.

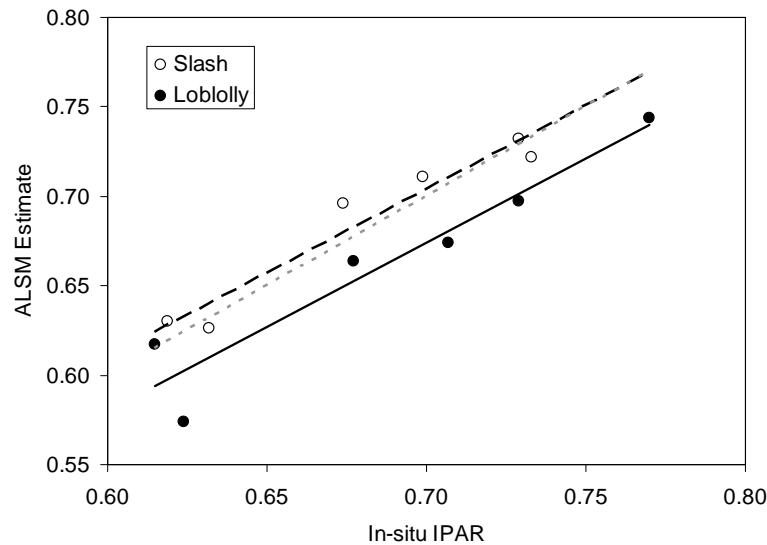


Figure 3-6. Relationship between observed (*in situ*) and estimated IPAR (from ALSM) using the cone function with $\alpha = 7^\circ$ and weighted by distance. Separate equations were developed for each species since analysis indicated statistically different intercepts ($p = 0.0094$). There was no significant difference for slopes between the equations so a common slope was used ($p = 0.4850$). The light dotted line represents a hypothetical 1-to-1 ratio between observed and estimated. The equation for Slash pine is $y = 0.9351x + 0.0493$, $r^2 = 0.935$, $RMSE = 0.0133$; and for Loblolly pine it is $y = 0.944x + 0.0132$, $r^2 = 0.913$, $RMSE = 0.0197$.

3.1.7 Discussion

3.1.7.1 Factors Influencing *in situ* IPAR

In general, fertilization builds leaf area and creates a denser canopy with high light interception (Sampson and Allen, 1998). This was the case in this study where fertilized loblolly pine had the greatest levels of light interception. The lack of differences in light interception between fertilized and non-fertilized slash pine was not unexpected since it is less responsive to

fertilization than loblolly pine (Roth *et al.*, 2007b). Individual tree mortality resulted in open gaps in this study area and corresponding lower amounts of light interception in the fertilized slash pine treatment plots. However, this occurred only where mortality was the most recent, since with time the surrounding tree canopies expand to fill these gaps.

3.1.7.2 Potential Sources of Error

One potential source of unexplained error in this investigation may be the relatively low sun elevations at the time of *in situ* PAR data acquisition (between 41° and 51°). At these angles there was some contribution to PAR interception from trees in the surrounding gross treatment plot. A hypothetical case in which the observer is in the center of the plot and the sun elevation angle is 45° is shown in Figure 3-7. Due to the plot size, trees outside the treatment plot can be seen to intercept the sunlight. While not quantified, it was assumed that tree attributes and mortality did not vary between the gross treatment and measurement portions of each plot.

Another potential source of error is the contribution of diffuse radiation. Laser light is phase-coherent and spectrally narrow-band, while sunlight is broad-band and incoherent. Therefore, in order to simplify the analysis, contributions from diffuse sky irradiance were neglected by virtue of using scope functions with narrow fields of view, collecting *in situ* measurements during clear sky conditions, and adjusting for the angle of the sun during the *in situ* measurements. For small α , too little interception was ascribed to the LiDAR points via equation 3-2, implying an overestimation of sunlight reaching the observer. This is likely caused by attributing too much of the measured light at the observer to direct solar irradiance because the contribution of indirect sky irradiance was neglected. A logical refinement of this work in future investigations would be to employ two separate scope functions to estimate IPAR, where one is tailored to capture the direct component of the total solar irradiance and the other tailored for the indirect component. However, a rigorous examination of those two components would

also require independent *in situ* measurements of each, which were not available for this investigation.

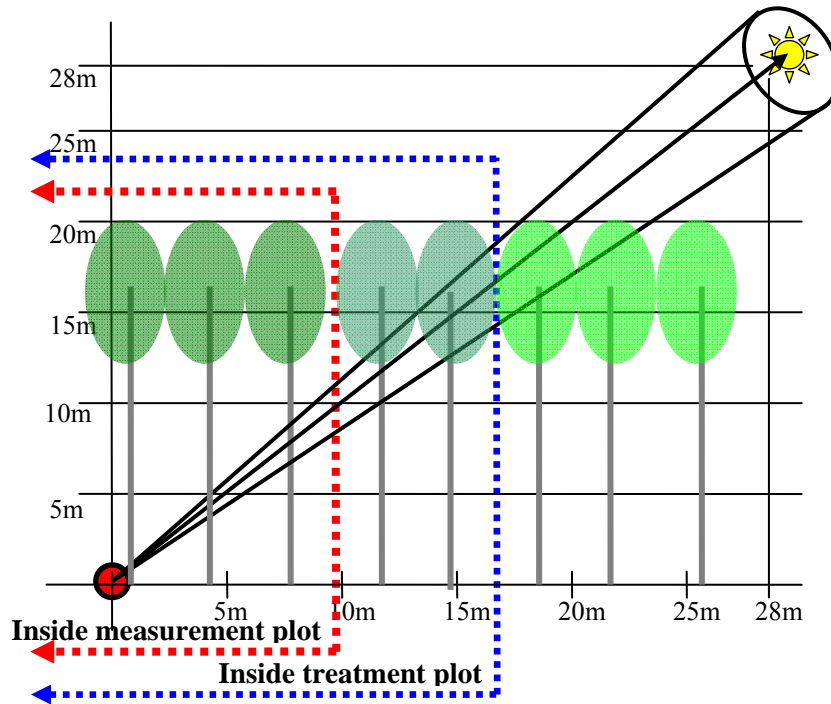


Figure 3-7. A side view of a plot with a hypothetical position of the sun and a scope function. When the sun elevation angle is 45° and the observer point (location of a scope function) is at the center of the plot, trees outside of the treatment plot can affect the PAR values.

Varying proportions of standing woody material to leaves is another potential source of error. Neither the exact reflectance nor orientation was known for objects reflecting emitted laser light, such as leaves or branches. It was therefore not possible to derive an explicit closed form relationship between the laser light reflection and sunlight interception, since the laser beam interacted with an unknown mixture of reflectors inside each 15 cm diameter footprint.

3.1.7.3 Bias Between Species

The slight, yet consistent, underestimation of IPAR for loblolly pine was unexpected and is thought to be due to structural differences in their canopy architecture. Slash pine canopies are

highly aggregated and clumped as opposed to loblolly pine, which is more diffused and continuous (Colbert *et al.*, 1990). Since each laser return is the result of laser photons reflecting from occluding surfaces, the surfaces must be dense enough to reflect a measurable signal back to the ALSM receiver optics. In the case of the underestimate for loblolly pine, it is thought that the diffuse canopy allowed a greater number of laser photons to pass through for a given amount of foliage. Apparently, the clumped canopy properties of slash pine, which have made traditional measures of light interception difficult to model (Gholz *et al.*, 1991), are in effect beneficial with respect to the ALSM methodology.

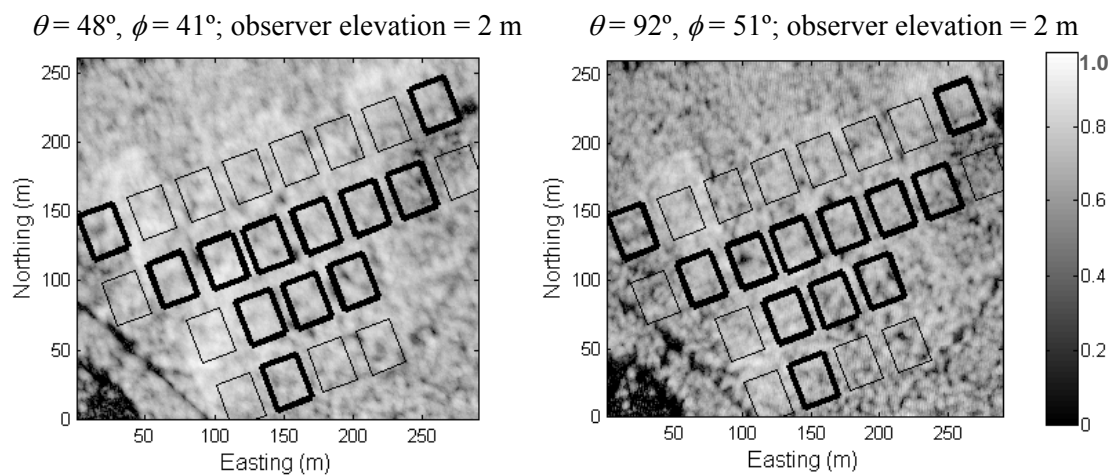


Figure 3-8. $IPAR_{ALSM}$ distribution for contrasting sun angles at an observer elevation of 2 m, illustrating the spatial resolution of $IPAR_{ALSM}$ computed in equation 3-2. The conical scope function weighted by the distance between the ALSM point and the observer was used in this case.

3.1.7.4 Spatial Variations of $IPAR_{ALSM}$

The ability of ALSM to estimate the 3D spatial variations in IPAR with superior spatial resolution is illustrated in Figure 3-8. The distribution of $IPAR_{ALSM}$ is computed using equation 3-2 assuming two different hypothetical sun angles at a 2 m elevation of scope origin. The

conical scope function weighted by the distance between the ALSM point and the observer was used in this case. Due to the conical nature of the scope, less spatial aggregating of the IPAR estimates is expected by using observer heights farther off of the ground since a raised conical scope will have a smaller radius when it intersects the canopy points. Thus, raising the scope has the potential to reveal more detailed canopy structure.

3.2 Detecting Forest Trails

There is a critical need to locate trails and other optical gaps in forested terrain for locating optimal paths and for planning troop movement, locating sites for optimal ground-to-sky Radio Frequency (RF) communications, and mapping areas of likely detection from overhead sensors. In this chapter, visibility vectors between candidate foliage voids are defined to identify optical lines of sights over the terrain. Most probable trails are detected using these optical lines of sights with help of the detected stem locations and geometric constraints.

3.2.1 Introduction

In forests with dense lower canopies and understories, walking trails can be regarded as narrow irregular paths in which there is an absence of understory biomass. Such trails that wind through densely forested terrain are difficult to detect by aerial photography and radar methods because the crown layer occludes the understory. Long-wavelength microwave energy can penetrate foliage, but discrimination of vertical structure requires more information than what a single radar backscatter image provides. In principle, vertical structure of the terrain and foliage can be estimated from multiple interferometric radar observations, but these observations generally lack the spatial resolution to detect small-scale voids in the foliage arising from trails.

ALSM technology that employs small footprints and two-stop detection can also penetrate dense canopy by illuminating the ground and understory through small gaps in the crown layer. While this leads to precisely located measurements under the canopy, the fraction of laser pulses

reflected back from below the canopy is small. These sparse measurements lead to a condition of undersampling. The layer of canopy just above the ground is the primary location of the biomass voids that correspond to trails. Yet, it is precisely the region that is most severely undersampled by ALSM sensors that record only first and last stops.

Because of the sparseness of the ALSM data from the understory and ground, direct detection of trails based on density variations in ALSM data points is not reliable. Instead, I derive several features from the ALSM data and use them to constrain the search space and infer the location of trails. First, the ground surface \hat{z}_g is estimated using the information-theoretic approach in section 2.3. Knowledge of the ground elevation constrains the search space and reduces the subsequent segmentation to a series of 2D problems. Then I use two characteristics of trails: (1) trail surfaces yield lower standard deviations of heights than does understory vegetation, and (2) the presence of a trail implies an empty volume immediately above the trail surface. Locations exhibiting these features are then used as seed locations for computing radial visibility functions.

The notion of visibility which is of much interest in surveillance applications (Zacks, 1994) implies a linearly oriented volume of empty space between two points. Each visibility vector is considered to be a local trail segment. Many false candidate vectors remain due to the data sparseness. Because trees rarely grow on trail surfaces, all visibility vectors that pass too close to the estimated tree trunk locations are discarded. Finally, additional features involving geometric consistency of visibility are used to further window the set of candidate trails segments. The primary trail is identified by choosing the longest connected set of trail segments (winner take all strategy). The trail detection algorithm is demonstrated in a dense forest near Gainesville, Florida.

3.2.2 Study Area and Data Acquisition

The study site was imaged with UF-ALSM system from an above ground altitude of 600 m. The site was imaged with two flight lines, resulting in an average of 2-2.5 returns per square meter. The majority returns correspond to the upper canopy, but some do manage to penetrate deep into the foliage through small gaps. At meter scales (the scales at which trails must be resolved) these penetrating shots are quite sparse, with an average of 0.25 returns per square meter.

The study area analyzed for this work is a mixed coniferous and deciduous forest in North-central Florida, USA. The forest is a part of Hogtown Greenway in the city of Gainesville (Figure 3-9). The true location of the walking trail (red dots) was acquired during a kinematic survey with an Ashtech geodetic GPS receiver, yielding few meter rms.

In the training site, the trail is generally straight and is roughly 3 m wide. An approach for identifying the trail was developed using this training site and then validated in the testing site, in which the trail is 2~3 m wide and curved at some points.

3.2.3 Data Segmentation

The presence of a trail implies an empty space above the trail surface where a person could walk. Trails form elongated and continuous voids in the vegetation while non-trail gaps exhibit irregular shapes. The trail in the training site is straight, so the empty space above the trail surface can be seen in the 3D point cloud (Figure 3-10). Most of the significant trail space resides between 1 m and 4 m above the ground. Selected last stop elevation points which penetrate through the canopy and reside in this space describe the gap distribution in this elevation level where the trail exists. However, the undersampling problem of ALSM in understory makes trail gaps and non-trail gaps indistinguishable based on these points alone (Figure 3-11).

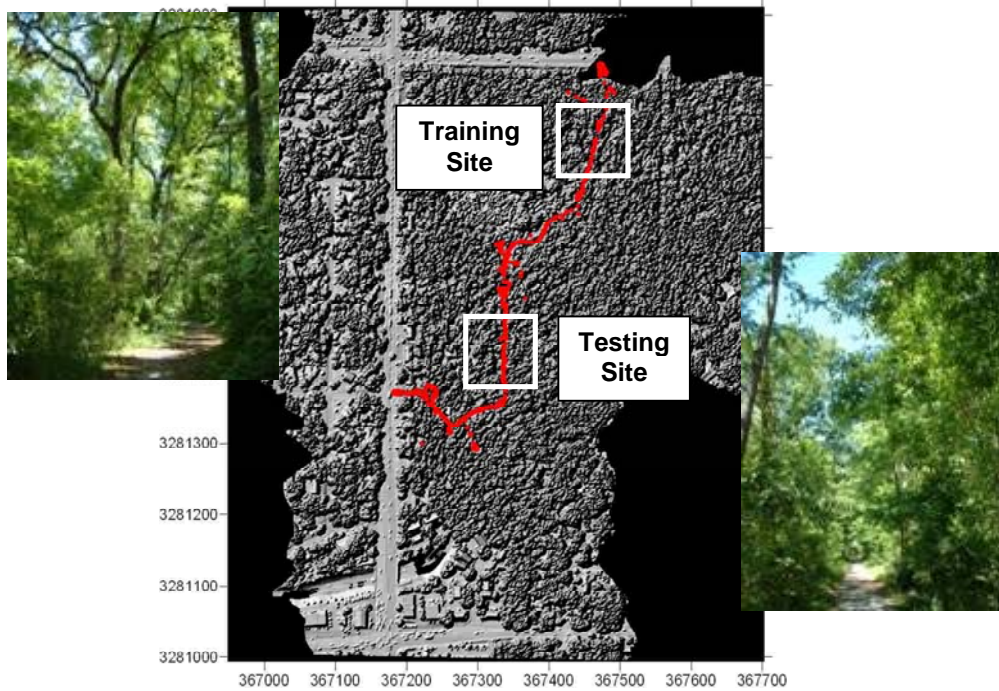


Figure 3-9. Shaded relief image and ground photos of the study area. The GPS trail is in red dots, training and testing sites photos are on each side. Axes labels in Universal Transverse Mercator (UTM) meters.

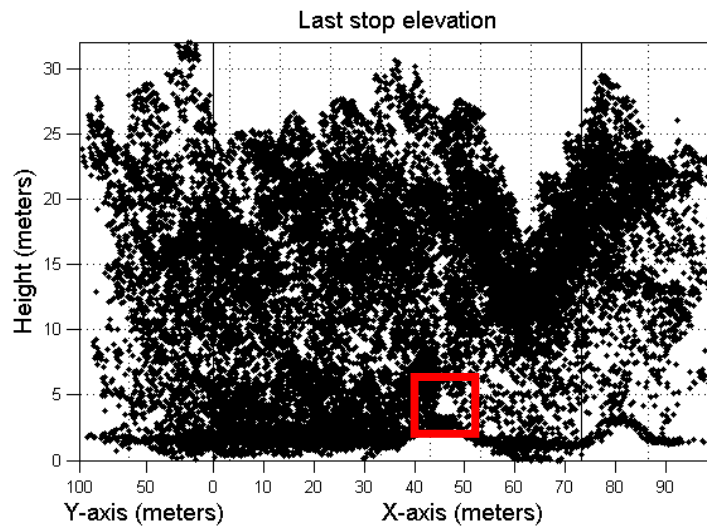


Figure 3-10. Point cloud from the training site. The empty space above the trail surface (red box) is the trail.

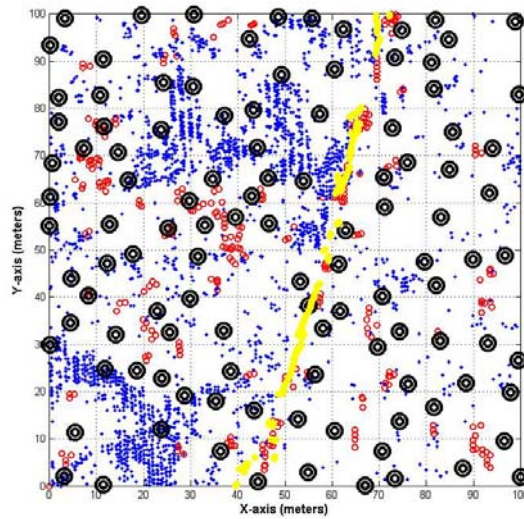


Figure 3-11. ALSM data points between 1 m and 4 m elevation (blue dots), tree trunks (black double circles), smooth surface points (red small circles), and GPS trail (yellow circles). Units are in meters.

Finding the connected gaps between two points on the trail is similar to computing the visibility between those points. Therefore, the selected data points will be considered as visibility blocks. However, it is still necessary to fill up the unknown space where no penetration occurs due to the data sparseness. The estimated tree trunk locations serve this purpose by adding the locations to the set of visibility blockers. An elaborate algorithm is introduced in Chapter 4 to detect and delineate individual tree crowns, but for the purpose of estimating of big dominant certain tree locations and avoid adopting falsely detected (or uncertain) small tree locations, only the seed finding process in section 4.3.1 is employed in this work. Adjacent trees are assumed to be at least 5 m apart (i.e. $R = 5$ m in the process of finding seed points). The selected peak points are added to the set of visibility blockers.

It is computationally intensive to compute the visibility for all angles at all locations, and the blockers are still too sparse to uniquely or clearly show trail paths. Another feature of trails is therefore used to further constrain the problem. I exploit the fact that height variances on the trail

surface should be small relative to variances in the understory. Triplets of ground surface points are used to compute a height standard deviation. A threshold α is computed, assuming a single measurement over an ideal flat plane (equation 3-3).

$$\alpha = std([0, 0, \beta]) \approx 0.058 \quad (3-3)$$

where $\beta = 0.1 \text{ m}$. The value of β includes the ALSM system error and the estimated ground surface error. Standard deviations less than α are considered smooth surfaces and are used as seeds for computing visibility vectors. The visibility blockers and smooth surface points are shown with the GPS trail in Figure 3-11.

3.2.4 Visibility Vectors and Geometric Constraints

While visibility is often regarded as a ray-tracing problem, in the foliage, we must recognize that meaningful visibility requires a reasonable (non-zero) solid angle. This constraint is enforced using a visibility cylinder, created between each pair of smooth surface points. Tree trunks and any ALSM points in this cylinder are considered as visibility blockers of the path between the two smooth surface points. The diameter of the cylinder is empirically chosen to be 3 m. Too small a diameter will yield many false visibility vectors, and too large a diameter will fail to detect some trail gaps. A slightly bigger scope diameter than the size of the actual trail may miss the clear optical gaps on the trail, but it could detect easiest paths to traverse through the terrain even if there is no formal trail in the area. It is assumed that more than three data points or a tree trunk inside this cylinder causes no visibility. All such visibility vectors are shown in Figure 3-12 (A). Note that false trails indicate potential lines-of-fire for tactical scenarios.

Finally, geometric constraints of visibility vectors are used to remove vectors which are on non-trails. First, the visibility vectors on trails should have front-back connections (non-terminal

points). A backside angle of $\pm 30^\circ$ is allowed, and all visibility vectors which do not have connections in this angle are eliminated. This angle gives the freedom of handling non-straight trails. The ability to detect more curved trails (or simply paths of potential trafficability) increases as this angle tolerance is increased, but that could also potentially increase the confusion between the real front-back connection and the side visibility vectors. Secondly, most real trails exhibit some side visibility. These side visibility vectors in an angle range ($30^\circ \sim 150^\circ$ on both sides) are removed where front-back connections exist. In this study area, there was only one trail. So, thirdly, the longest trail is selected after summing the lengths of the connected paths to finalize the detection in a “winner take all” strategy (Figure 3-12 (B)). Unlike the study site in this work, more than one trail could exist in many cases. In those cases, instead of finding the only winning trail, we could find multiple paths by successively omitting the winning paths from consideration and picking the “next best” path. For the case where there is no formal trail but one desires to detect paths of least resistance for route planning and soldier trafficability analysis, we could use all acquired visibility vectors that are found in Figure 3-12.

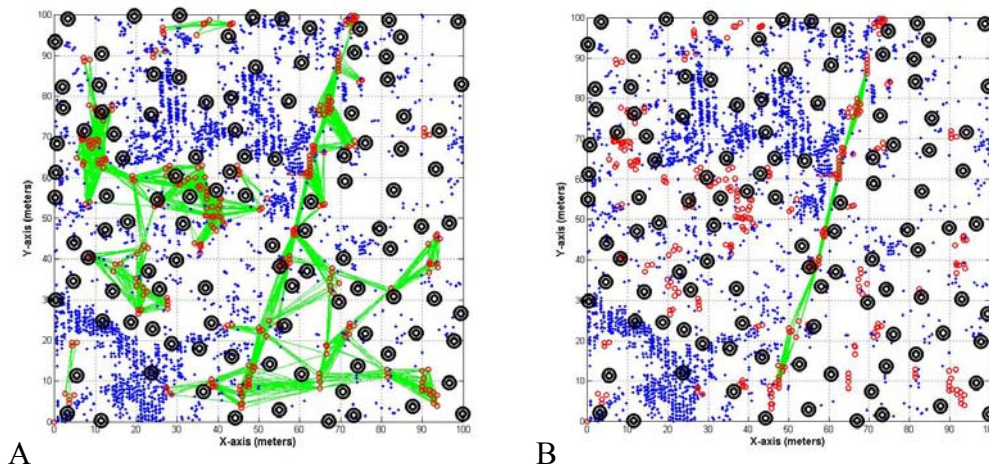


Figure 3-12. All acquired visibility vectors and the winning trail candidate in the training site.
A) Visibility vectors (green lines). B) The winning trail candidate in the training area (green lines). All units are in meters.

3.2.5 Result on Test Sites

The trail in the testing site is fairly straight overall, but is locally curved at several points and narrower than in the training site (2 m ~ 3 m). Using the same approach as in the training site, visibility blockers, tree trunks, and smooth surface points are acquired. GPS trail points are indicated with these segmented points in Figure 3-13 (A). The winning trail candidate is shown in Figure 3-13 (B) after using the same geometric constraints of visibility vectors as in the training site. The trail in the testing site is successfully detected. Note that the edges (north and south side) of the trail do not have visibility vectors because they do not have front-back connections.

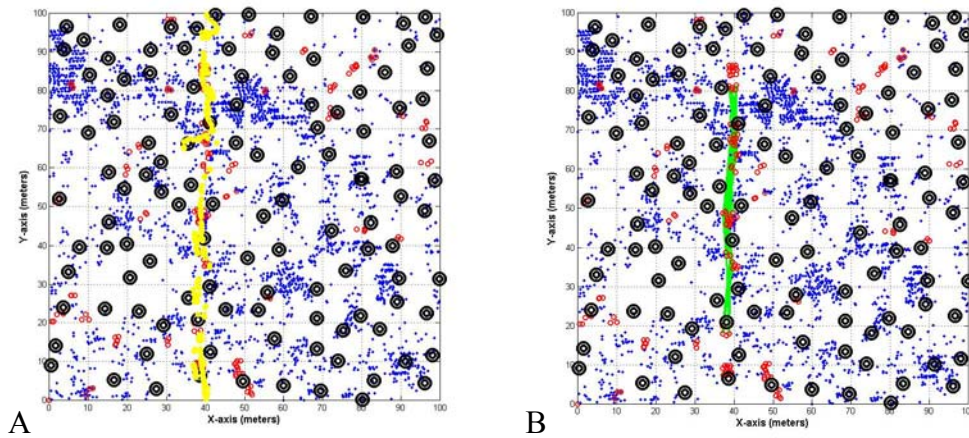


Figure 3-13. The winning trail candidate in the testing site. A) Segmented points and GPS trail (yellow circles) in the testing area. B) The winning trail candidate in the testing area (green lines). All units are in meters.

CHAPTER 4 A CLUSTERING APPROACH TO INDIVIDUAL TREE DETECTION

4.1 Introduction

In Chapter 3, two important applications were presented that utilize field-of-view (scope) geometric mappings. Such structuring elements were appropriate for those point-to-point paradigms. Most civilian research and management of forests, however, is more concerned with structural parameters that relate directly to individual trees because they bear directly on ecological health of the forest and the potential yield of forest stands in timber or paper pulp resources. More recently, it has been suggested that the estimation of such parameters could also be used to arbitrate carbon sequestration and cap-and-trade practices to mitigate the buildup of greenhouse gasses (Binford *et al.*, 2006).

Locating and delineating full tree crowns can enable estimates of tree counts, tree species, crown area, canopy closure, gap analysis and volume and biomass estimation (Gougeon and Leckie, 2003; Reurebuch *et al.*, 2005). For the detection of single trees from LiDAR data, most previous work has focused on segmentation of rasterized or interpolated tree height images (i.e. 2D digital images in which the pixel value equates to height, also called Digital Surface Model (DSM)) using standard image processing methods (Hyypä *et al.*, 2001; Persson *et al.*, 2002; Holmgren and Persson, 2004; Chen *et al.*, 2006; Koch *et al.*, 2006). However, airborne LiDAR data is acquired as a discrete set of point locations (a so-called “point cloud”), and collapsing the point cloud down into an image unnecessarily discards much useful information. Recent work has been reported that employs direct processing on the original LiDAR point data rather than rasterized image data (Andersen *et al.*, 2002; Pyysalo and Hyypä, 2002; Morsdorf *et al.*, 2003; Wack *et al.*, 2003) to avoid this loss of information.

There is strong interest in the integration of laser scanning and aerial imagery because laser data provide accurate height information and 3D crown shape (at high point densities), whereas optical imagery provides better planform geometry and color (spectral) information (Hyypä *et al.*, 2004). Leckie *et al.* (2003), Popescu *et al.* (2003), Popescu *et al.* (2004), and Popescu and Wynne (2004) used laser scanning and aerial imagery data on the problem of single tree isolation. However, the focus here is to develop an improved method to segment trees based solely on LiDAR measurements, with the understanding that the proposed method could subsequently be used in conjunction with imagery to further improve segmentation.

Even with high resolution LiDAR data, such as that described herein, individual trees can be hard to separate because more than one tree can occupy a given volume above a surface patch, e.g. interlocked canopies and leaning trees (Figure 4-1 (B) and (C)). This results in clusters in the tree segmentation process that can have severe overlap. In addition to the overlapped canopies, some other characteristics of trees, such as very irregular shapes and the different sizes of tree canopies as shown in Figure 4-1 (A) make the use of simple detection techniques problematic.

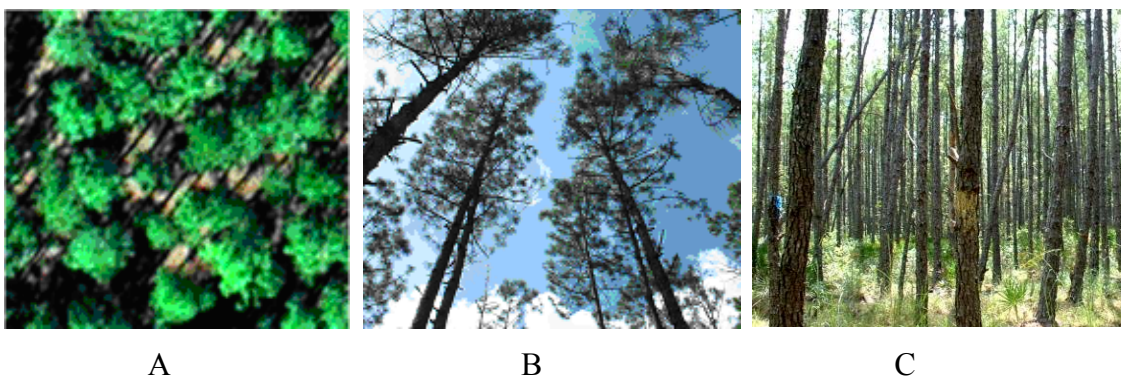


Figure 4-1. Aerial photos illustrating the variation of canopy morphology even within managed pine forests. A) An aerial photo showing irregular shapes and different sizes of tree canopies. B) A ground photo showing interlocked canopies. C) A ground photo showing leaning trees.

The most common approach to segmenting trees in LiDAR data is to employ a region growing algorithm instantiated with “seed points” on each tree. Finding the seeds (i.e. treetops) is a crucial step in the process of detecting individual trees since subsequent steps are heavily dependent on the number of seeds and the locations of seeds. Most current approaches are moderately successful, provided that the filter size and image smoothing parameters are appropriate for the particular tree size and image resolution (Gougeon and Leckie, 2003). Finding an appropriate size of filter (or search radius when point data is used) to detect the treetops is not a trivial problem because different filter sizes should be applied to different areas for optimal detection accuracy. Schardt *et al.* (2002) and Brandtberg *et al.* (2003) tried to solve this problem using linear scale-space method (Lindeberg, 1996) that was based on Gaussian smoothing of the rasterized image data at multiple scales. Results from this approach remain sensitive to determining the appropriate scale parameter, and the step of convolving the image with a Gaussian kernel could be problematic because individual canopies may exhibit diverse asymmetric shapes. A detailed explanation of the scale-space method and its implementation on the study sites are presented in section 4.2.

In this work, I address the issue of the size of the search radius, R , and propose an approach that automatically grows locally optimal canopy clusters, or regions, (equivalent to an adaptive search radius) to segment individual trees. All steps in the process work directly on the 3D ‘cloud’ of LiDAR points. I first separate the laser returns corresponding to the ground from those corresponding to the above-ground biomass using an adaptive multiscale filter (Kampa and Slatton, 2004) presented in section 2.3. In the process, the low order (slowly varying) terrain surface is subtracted from the LiDAR points to “level out” the ground. The subsequent tree segmentation operates only on the above-ground points and is divided into three main stages: (1)

finding all possible seed points for each tree using a minimum search radius R_{\min} , (2) region growing instantiated at those seed points, (3) merging partial tree detections (incomplete clusters) using an agglomerative hierarchical structure.

4.2 Scale-Space Method

It is well known that measurements of many natural processes or objects often exhibit structure over a wide range of scales (Turcotte, 1997). In the particular case of tree segmentation in aerial data (be it from LiDAR or some other modality, such as multispectral imagery or radar), one finds that trees in localized stands may exhibit similar canopy shapes and sizes, but over larger areas or multiple areas the canopy shapes and sizes can vary widely. Thus, for a tree segmentation algorithm to be truly successful, it must accommodate this variation automatically without requiring a high degree of empirical “tuning” for each site. The scale-space method represents one of the most successful previous methods for addressing tree segmentation in LiDAR data, and is thus explored here for the purpose of providing context to the new method proposed in this work.

In image processing, extracting meaningful structure that exists over a certain range of scales, sometimes referred to as multi-scale structure (Lindeberg, 1993) is often handled by creating a scale-space representation of the image data. The idea of scale in signals and scale-space filtering of 1D signals were introduced by Witkin (1983) and Koenderink (1984). A scale-space representation of a given image $f(x, y)$ is a family of derived signals $L(x, y; t)$ defined by convolution of the image with Gaussian kernels of different variances $g(x, y; t)$ with the scale parameter $t = \sigma^2$ (equation 4-1).

$$L(x, y; t) = g(x, y; t) * f(x, y) \quad (4-1)$$

The 2D Gaussian kernel at scale level t is given in equation 4-2.

$$g(x, y; t) = \frac{1}{2\pi t} \exp\left(\frac{-(x^2 + y^2)}{2t}\right) \quad (4-2)$$

The Gaussian kernel belongs to a class of kernels that guarantees a monotonic smoothing of the original image (Babaud *et al.*, 1986) meaning that Gaussian smoothing does not produce new extrema when increasing the scale parameter.

As a preliminary step, for the detection of individual trees, the 3D point data are converted into a 2D digital height image by selecting the maximum height laser point within each grid cell. The pixels with empty values are replaced with the mean of non-zero neighbor pixels, and this process is repeated until no empty values exist in the image by gradually employing more neighbor pixels (Figure 4-2). Often times, laser point outliers from a lightly Gaussian smoothed 2D height surface are removed to produce a smooth and consistent canopy surface.

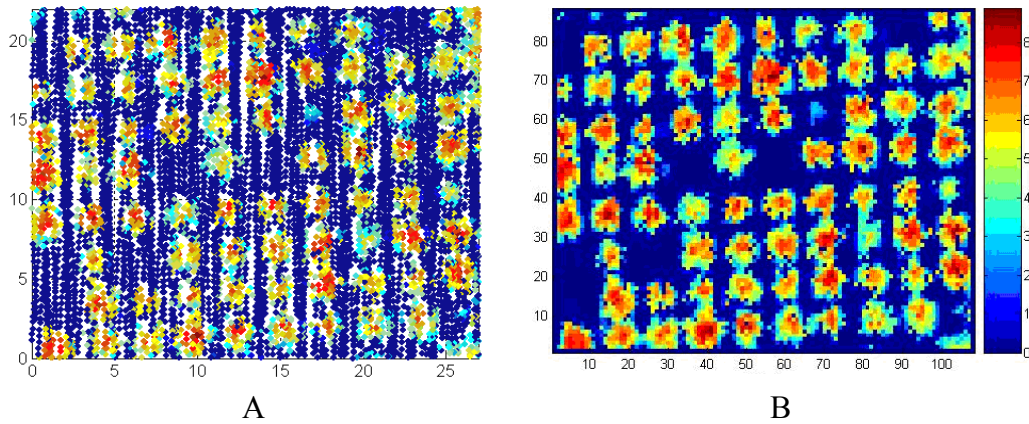


Figure 4-2. Creation of 2D height image from 3D LiDAR point clouds. A) First-stop 3D elevation points in a plot with low culture at PPINES. Units are in meters. B) Interpolated image of the 3D laser points with a 25 cm pixel size. Thus, the imaged area is roughly 27 m by 22 m.

A scale-space representation of the image in Figure 4-2 (B) using equation 4-1 is shown in Figure 4-3. Since an appropriate scale interval is not known in advance, in practice, a user defines a range of scales with a constant scale increment. In this example, a large interval is

chosen (here, $\sigma = [0.5, 6]$) with an increment of 0.5 to see the changes in a wide range. Each layer in the scale-space stack (Figure 4-3 (B)) represents convolution at a scale showing the evolution of the original image through scale. Individual images have been successively smoothed by convolution with a Gaussian kernel of increasing scale.

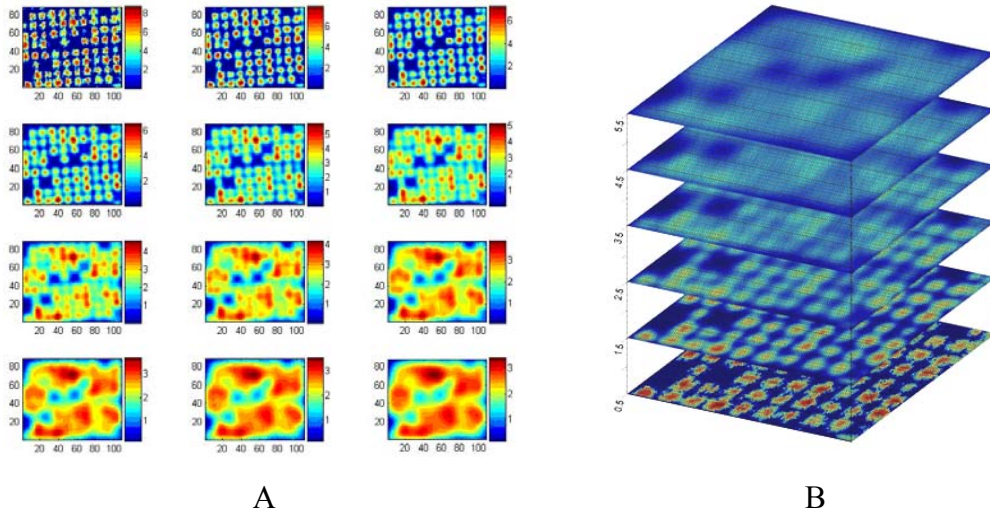


Figure 4-3. An example of a scale-space representation. A) A scale-space representation of the image in Figure 4-2 (B) with σ ranging from 0.5 to 6.0 in increments of 0.5 (beginning from the top left to the bottom right). B) An illustration of the scale-space stack. The smallest σ resides on the bottom of the stack, and the largest on the top.

Although the scale-space method well represents image structures at multiple scales, it does not address the problem of selecting locally appropriate scales to detect wanted objects. A general methodology for feature detection with automatic scale selection has been proposed by Lindeberg (1993). This method is based on local extrema over scales of different combinations of normalized derivatives. Lindeberg (1993) showed that a Gaussian “blob” with characteristic radius $\sqrt{t_0}$ assumes a maximum of its scale-space signature at a scale t_0 . The scale-space signature of a blob is given by the normalized Laplacian (equation 4-3)

$$\left| \nabla_{norm}^2 L(x, y; t) \right| = t \left| L_{xx} + L_{yy} \right| \quad (4-3)$$

where L_{xx} and L_{yy} are the 2nd order derivatives along x-axis and y-axis respectively. The normalization factor, t , allows the blobs to be compared at different scale-levels. These derivatives are computed at the spatial maximum of the blob, which is found by locating the maximum value in a moving window of pre-defined size. The detected blobs and strength of their scale-space signatures at each scale is shown in Figure 4-4. Note that the scale-space signature becomes stronger and the number of blobs reduces as the scale parameter increases.

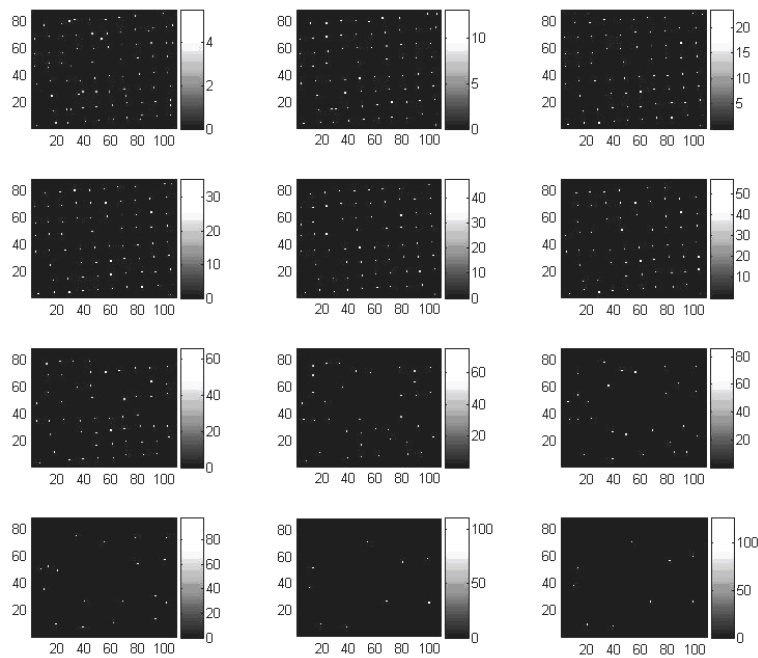


Figure 4-4. The detected blobs and strength of their scale-space signatures at each scale. The scale, $\sigma = [0.5:0.5:6]$, starts from the top left to the bottom right.

The dominant scale-level in the image is revealed by the mean blob signature (Figure 4-5). The mean blob signature typically has a maximum at a certain scale, and an appropriate scale interval is usually defined from this mean blob signature graph in order to capture blobs of notably smaller and larger sizes. Figure 4-5 indicates that the size of the dominant blobs for this

example is around at $\sigma = 3$ (i.e. 3 pixels = 0.75 cm in radius), which roughly corresponds to the significant width of dominant tree crowns in this plot when doubled for crown diameter.

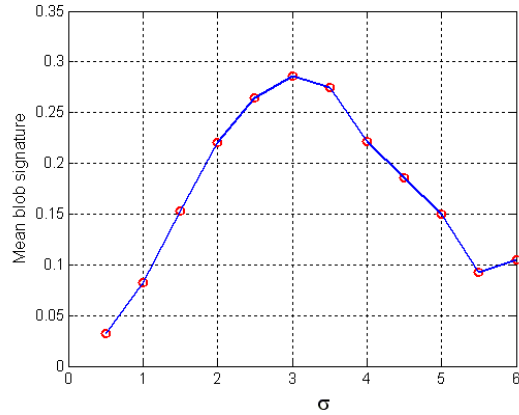


Figure 4-5. The mean blob signature. The maximum occurred at a scale corresponding to $\sigma = 3$.

All detected blobs from the scale-space interval are now sorted in descending order according to their blob strength. The strongest blobs are marked in the image in this order until the distance between the current blob and other marked blobs are far enough (here, 4 pixels = 1 m is chosen for the threshold to yield best results). The identified single blobs represent individual trees, and the result in the selected area is shown in Figure 4-6. Several false positives are found in the measurement plot.

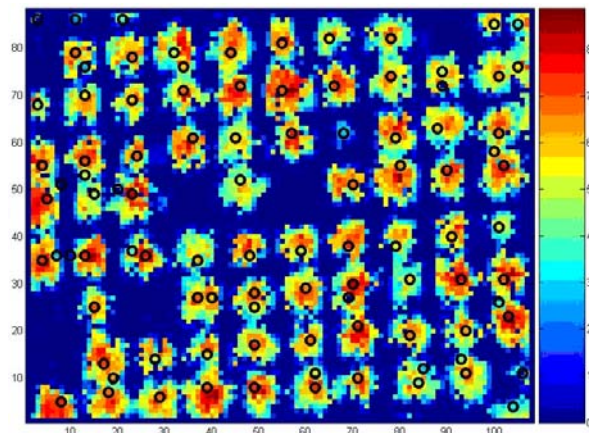


Figure 4-6. The result of individual tree detection by the scale-space method. The detected trees are shown by black circles.

4.3 Proposed Algorithm

4.3.1 Finding Seed Locations

Finding the seed points (i.e. treetops) for canopies in the LiDAR point cloud is a crucial step since it serves as the initial condition for subsequent steps. The search radius R (or, when rasterized image data are used, the window size of the local-maximum filter) determines the minimum allowable canopy radius, and the seed point should be the highest LiDAR point for a particular tree canopy. In this section, an algorithm is developed to find the seed locations using the raw laser point data assuming that R is known for the region of interest (ROI). In general, the appropriate size of R is not known, and this case will be explored in section 4.3.4. The elevations of the first-stop LiDAR points are used for this step since these points better express the overall top canopies than do the last-stop elevation points.

To identify the seed points, it starts by finding the highest point h_1 in the LiDAR data set, denoted by A , which is taken to be the first seed point s_1 . The subset A' is then formed by removing points proximal to s_1 from the set A . Proximal points are defined to be those points in the full data set A inside a circular search region (with the radius R) centered at a seed point. The highest point h_2 is then located within A' . If h_2 is higher than the set of points proximal to h_2 in set A (Figure 4-7 (A)), it is identified as a second seed point s_2 and a reduced subset A'' is defined. If h_2 is not higher than the points proximal to it (Figure 4-7 (b)), the next highest point h_3 in A' is identified. The process is repeated to identify additional seed points in progressively smaller subsets $\dots A'' \subset A' \subset A$ while using the entire data set A to search for proximal points. This process terminates when all such seed points are found. The seed points are then indexed to represent individual trees. The algorithm is summarized by a pseudo code in Table 4-1.

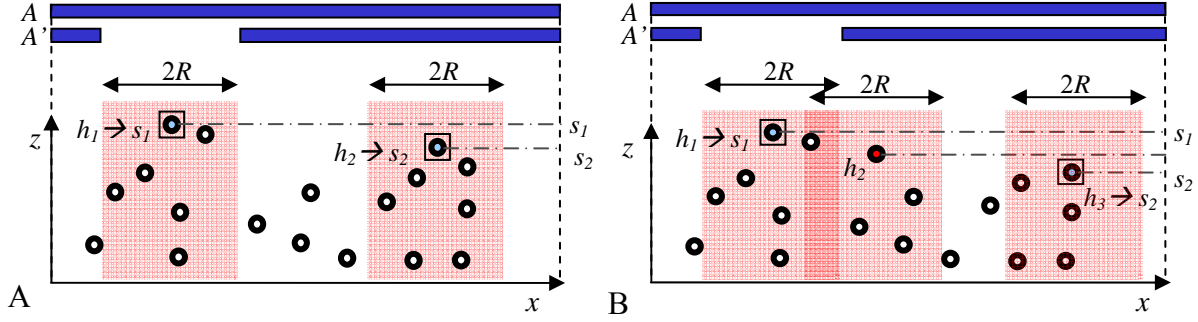


Figure 4-7. Identifying the seed points in two different cases. A) The case of the highest point in set A' , h_2 , being above all points within the search region ($2R$), so that $h_2 \rightarrow s_2$. B) The case of the highest point in A' , h_2 , not being above all points within the search region ($2R$), so $h_3 \rightarrow s_2$.

Table 4-1. Algorithm of finding seed points.

Initialization: $i = 1$, R , $F = \{ \}$
Set $A = \{ \text{all LiDAR points in ROI} \}$
The set of seed points: $S = \{ \}$
Define neighbor points: $N_R(h) = \{ p : \text{dist}(p, h) \leq R \}$
 $A^{(0)} = A$, $A^{(i)} = A - \bigcup_{j=1}^i N_R(s_j)$ for $i \geq 1$
while $(A^{(i-1)} - F) \neq \{ \}$
 $h_i = \max(a \in A^{(i-1)} - F)$
 $f = \max(a \in N_R(h_i))$
 if $h_i = f$
 $s_i = h_i$, $F = \{ \}$, $i = i + 1$, $S = S \cup \{ S_i \}$
 else if $h_i < f$
 $F = F \cup \{ h_i \}$
 end if
end while

4.3.2 The Effect of R on Finding Seed Points

Most previous algorithms for finding seed points either assume that the search radius R (or size of the moving window) is known *a priori* or they empirically test different sizes to find the best one for a particular site. However, it is not optimal to define a single measure of canopy

size due to their irregular shapes and different morphologies across various tree species, ages, and management treatments. As one would expect, tree detection results are very sensitive to the size of R . If R is too large, small trees are missed, yet elongate branches (or small clusters of branches) are mistakenly segmented as trees if R is too small (Figure 4-8). Therefore, there is a need for a systematic approach to find an optimal size of R that adaptively reacts to the nature of the canopies locally in the given ROI.

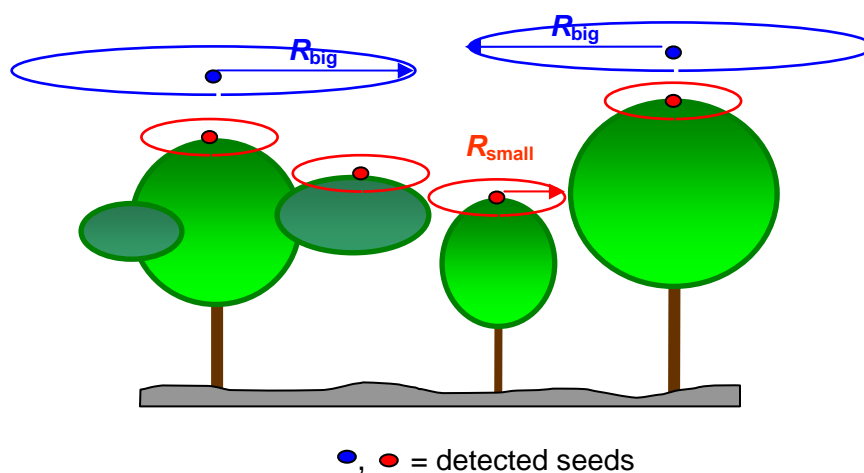


Figure 4-8. Sensitivity of the detection result to the search region R . If a single R value is used that is too big, elongated branches are not detected as trees, which is good, but some small trees are missed, which is not good. The converse occurs if a single value for R is used that is too small.

As an example, a small area (14 m×14 m) in the IMPAC site is selected (Figure 4-9 (A)). The Figure 4-9 (B) shows the changes in the number of detected seeds when different sizes of R (from 10 m to 1 m in intervals of 0.1 m) are used over the area. Figure 4-10 shows the locations of detected trees with different sizes of R . Note that using smaller intervals than 0.1 m or R values smaller than 1 m would not provide any reliable improvement since the LiDAR data have approximately decimeter point spacing. Using the algorithm described in section 4.3.1, we see that more trees are detected as R decreases, but we also get more falsely detected trees. There

are 9 trees in this example area, and the number of detected seed points is very close to the ground truth when $R = 1.3$ m, but it never found the correct number of trees. The implication is that a single value of R is not sufficient to detect all different sizes of trees in general. To overcome this problem, an agglomerative clustering approach is developed and described in section 4.3.4. Through the local agglomeration of small clusters, the effect of a spatially-adaptive R is realized while assuring every point is uniquely associated with a particular tree cluster.

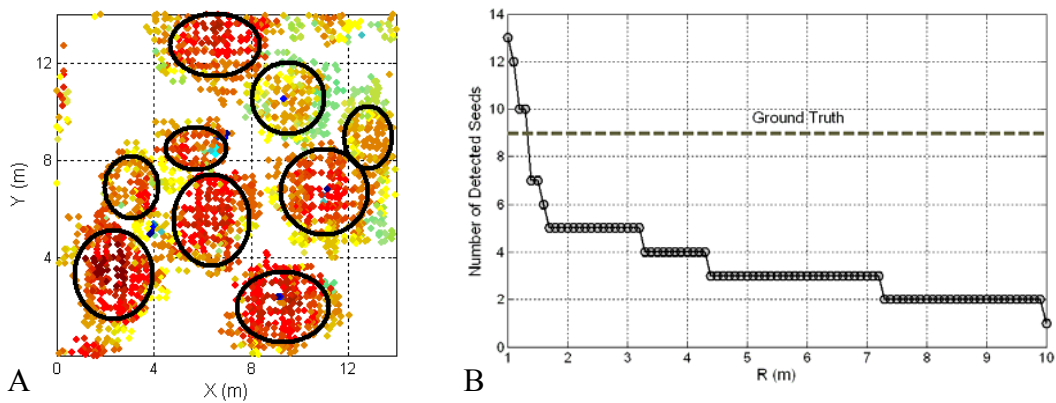


Figure 4-9. The number of detected seeds depending on R in a small selected area. A) The ground truth of a small selected area (14 m×14 m). The known tree locations are circled in the area. B) The number of detected seeds for the area depending on the size of R . The number of real trees in the plot, which is 9, is indicated by the dashed line.

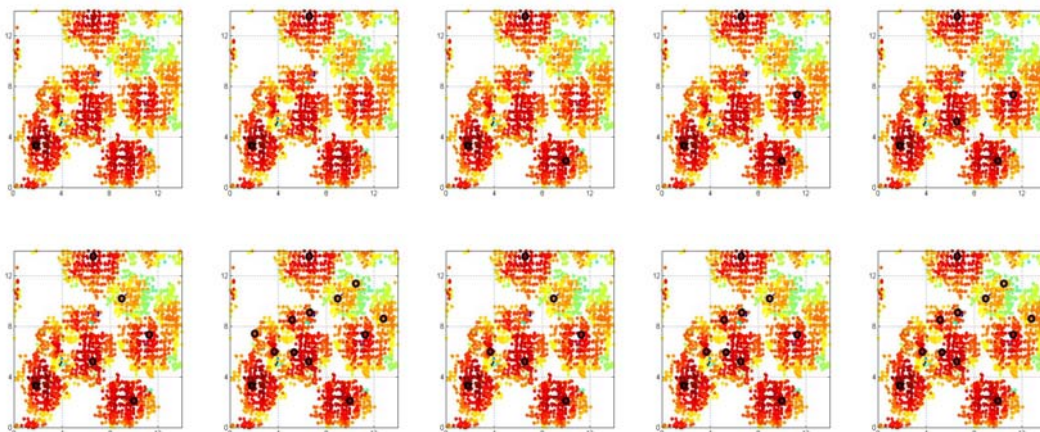


Figure 4-10. The changes in detected seed points that occur by changing the size of R from 10 m to 1 m (from top left to bottom right). All units in meters.

4.3.3 Region Growing Process

After finding the seed locations, the remaining LiDAR points associated with individual tree canopies need to be delineated. It is challenging to extract the exact boundaries between trees because some tree canopies are intermingled (overlapping in 3D) and tree canopy boundaries are not always distinct. The well known watershed segmentation algorithm (Beucher and Lantuejoul, 1979) has been the most popular method to delineate the tree crown boundaries in 2D (image) data. By conceptually pouring water onto the elevation image starting at the seed locations, the approximate tree boundaries are detected as connected paths. In this study, I develop a new method that is similar in concept to the watershed segmentation but applicable to the raw LiDAR 3D point data

To find the boundary of each tree, the first-stop elevation points are used. First, the seed points are found using $R = 1$ m and then indexed. Starting from the highest point that is not already indexed, the nearest indexed point that is above the current considered point is found. If the horizontal distance between the current point and that nearest indexed neighbor is smaller than an interval T , the current point is assigned the same index number as that neighbor. Otherwise, it is not labeled. The interval T starts from 0.1 m. Once all the points in the ROI are considered, T is increased by 0.1 m, and the process is repeated. This incremented labeling progressively grows the clusters of LiDAR points associated with each seed point until we form a collectively exhaustive and mutually exclusive collection of sets representing the initial tree canopies. The purpose of restricting the labeling to a neighborhood, set by T , and adopting the label of the nearest indexed point within that neighborhood regardless of whether it is a seed point or just a previously indexed point is to reduce the chance of erroneously associating a considered point on a large canopy with a smaller tree (seed) that happens to be closer. An illustration of this case is shown in Figure 4-11. In the figure, assigning labels using Euclidian

distance would result in $L : x_i \rightarrow s_1$ (i.e. Tree 1) because of $d_1 < d_2$ even though we see that x_i should be associated with s_2 (i.e. Tree 2). By following the incremental labeling by growing regions with T as described herein, we can correctly associate points with larger canopies even if they are closer to smaller trees. This is critical since we have instances of canopies touching or overlapping. The LiDAR point spacing dictates the range of reasonable starting values and step sizes for T , which are roughly 1 to 2 times the nominal LiDAR point spacing. The algorithm of region growing process is illustrated in Table 4-2, and an example of a region growing result is shown in Figure 4-12. In it, the seed points were found using $R = 1$ m, and the regions were subsequently grown by incrementing T from 0.1 m in steps of 0.1 m until all points were labeled.

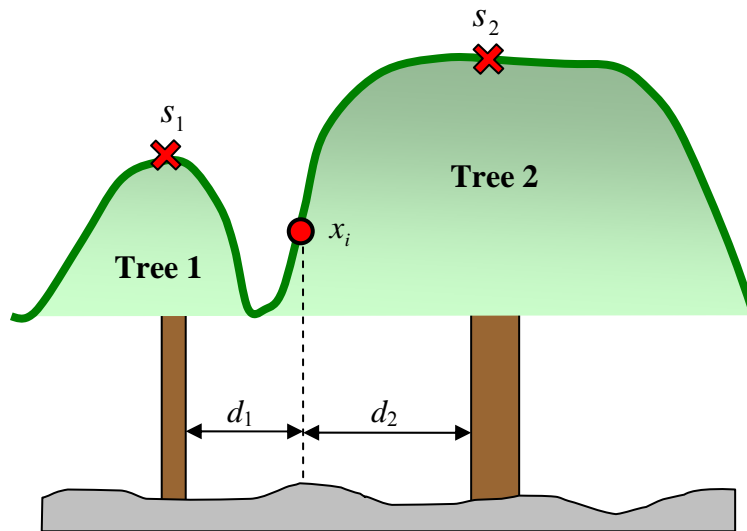


Figure 4-11. An illustration of a case where T is necessary. The point x_i can be correctly associated with Tree 2 by following the incremental labeling by growing regions with T . s_1 and s_2 represent the treetops (i.e. seed points) of Tree 1 and Tree 2 respectively.

Table 4-2. Region growing algorithm.

```

Initialization:  $T$ ,  $T_{step}$ 
Set  $A = \{\text{all LiDAR points in ROI}\}$ 
The set of seed points:  $S = \{s_1, s_2, \dots, s_l\}$ 
The set of unlabeled points:  $P = A - S = \{p_1, p_2, \dots, p_n\}$ 
The set of labeled points:  $B = \{b_1, b_2, \dots, b_m\}$ 
Set  $B = S$ 
Sort  $P$  (high  $\rightarrow$  low)
while  $P \neq \{\}$ 
    for  $i = 1$ : number of points in  $P$ 
        Find the nearest point from  $p_i$ :  $b_{\min}$ 
        if  $dist_{xy}(p_i, b_{\min}) < T$ 
             $B = B \cup \{p_i\}$ 
             $P = P - \{p_i\}$ 
        end if
    end for
     $T = T + T_{step}$ 
     $n = size(P)$ 
end while

```

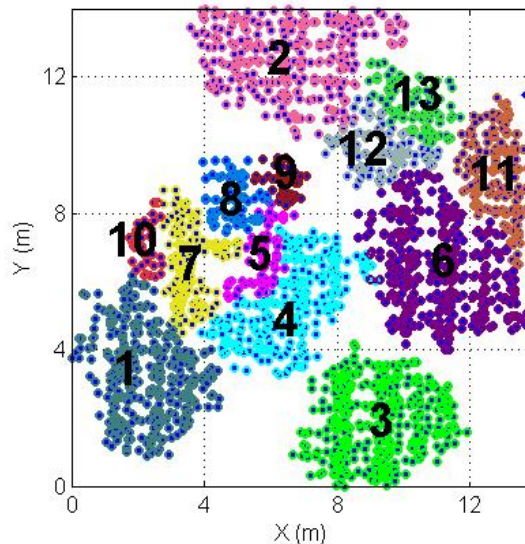
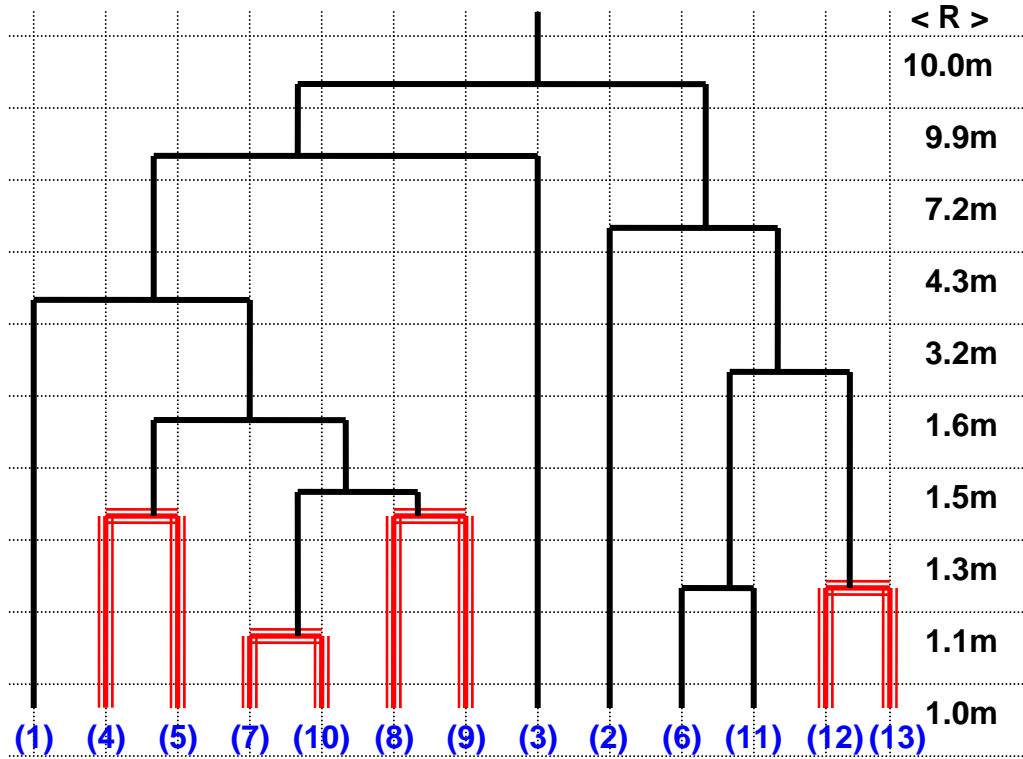


Figure 4-12. An example of the region growing result with incrementing T from 0.1 m in steps of 0.1 m until all points are labeled. The seed points are found using $R = 1$ m. This is a downward looking view of the area in Figure 4-9 (A). Each color indicates a segmented cluster of LiDAR points representing a detected tree in the region growing process. Each cluster is numbered from 1 to 13. Over segmentation can be seen in some cases.

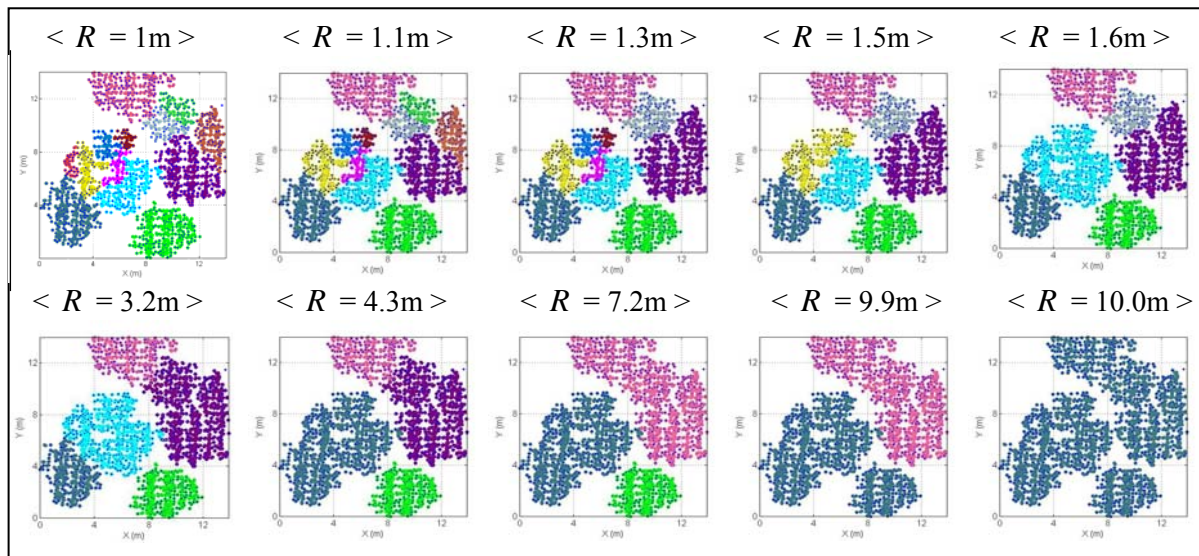
4.3.4 Agglomerative Hierarchical Clustering

Even with the incremented labeling described in section 4.3.3, we expect the initial results to be over segmented in some instances (Figure 4-12) since R was chosen small so as not to miss trees. An agglomerative hierarchical clustering approach is therefore employed to overcome this over segmentation. To show the inherent hierarchical structure of this problem, in Figure 4-13, a hierarchical tree is created by merging the clusters created by the region growing process in section 4.3.3 based on the specific values of R that was found in section 4.3.2. The merging clusters, eight small clusters should be merged as four trees, are shown with red branches. As shown in the hierarchical tree, one value of R cannot guarantee successful segmentation.

Agglomerative hierarchical methods generally begin with each observation being considered as a separate cluster and then proceed to combine clusters until all observations belong to one cluster or some stopping criterion is satisfied. Each LiDAR point could represent an individual observation (i.e. singleton) in the lowest level of the hierarchical clustering data structure, but it would not be very meaningful or computationally efficient to use individual LiDAR points to initiate the clustering. Since the size of R dictates the size of tree canopy clusters that can be detected, I specify a minimum value for R to be 1 m because no trees smaller than that are present in the study sites. Note however, that the minimum value of R could be chosen to be smaller if needed.



A



B

Figure 4-13. An example of hierarchical tree and merged clusters at specific levels of R . A) An example of hierarchical tree over the small area in Figure 4-9. Each number represents a cluster at the lowest level, and the red branches in the hierarchical tree are the cases where the following clusters should be merged. B) Merged clusters at specific levels of R . All units are in meters.

The region growing process in section 4.3.3 provides the set of clusters at the lowest level (i.e. the leaf level) of the hierarchical clustering tree. From that point on, clusters are merged solely using agglomeration and not region growing. Small clusters representing partial canopies are merged with their nearest neighbor cluster in space as determined by the distance $d(r, s)$ between cluster centroids (also known as the ‘centroid linkage’ method). Essentially, $\min(d)$ is used to establish which clusters are nearest neighbors. In equation 4-4, $d(r, s)$ is the horizontal l^2 -norm (Euclidean distance) between cluster centroids, n_r, n_s are the number of LiDAR points in cluster r and s respectively, and \underline{x}_{r_i} is the i th point in cluster r .

$$d(r, s) = \left\| \frac{1}{n_r} \sum_{i=1}^{n_r} \underline{x}_{r_i} - \frac{1}{n_s} \sum_{i=1}^{n_s} \underline{x}_{s_i} \right\|_2 \quad (4-4)$$

In most agglomerative methods, the decision to merge clusters requires a threshold test on a similarity measure. For tree segmentation, when attempting to select a threshold value based solely on 2D measures of horizontal point similarity, it is generally not possible to find a value that provides good separation among all trees and yet does not over segment individual tree canopies that exhibit large elongated branches (i.e. partial-tree clusters), which may appear similar to small, yet complete tree clusters. Thus, I exploit the canopy penetration of the LiDAR to find a threshold based upon vertical point adjacency within a cluster. A value for each cluster is assigned to be the standard deviation of z values (above-ground elevations of both first and last returns), σ_z . It was suspected that high values of σ_z would occur for complete trees and lower values of σ_z would occur for elongated branches because of the larger vertical distribution of biomass in complete trees. All clusters satisfying $\sigma_z < \tau$ are merged with their nearest cluster neighbors by the centroid linkage technique, where the threshold τ is determined via supervised

learning. This process is repeated at the next level in the clustering tree until no clusters remain with $\sigma_z < \tau$. Through this process, we realize the effect of a spatially adaptive R . Table 4-3 outlines the agglomerative clustering algorithm that is developed in this section.

Table 4-3. Agglomerative clustering algorithm.

```

Initialization:  $R_{\min}, T, T_{step}$ 
Set level index  $L = 1$ 
Do seed finding process at  $L$  (section 4.3.1)
Do region growing process ( $T, T_{step}$ ) (section 4.3.3)
while any cluster satisfies  $\sigma_z < \tau$  at  $L$ 
    for  $i = 1$ : number of clusters at  $L$ 
        Compute  $\sigma_z$  for cluster  $i$ ;  $\sigma_z(c_i)$ 
        Compare  $\sigma_z(c_i)$  with  $\tau$ 
        if  $\sigma_z(c_i) \geq \tau$ 
            Leave  $c_i$  as is
        else if  $\sigma_z(c_i) < \tau$ 
            Find the nearest cluster,  $c_j$ , by centroid linkage
            Merge  $c_i$  with  $c_j$ :  $c_j \leftarrow c_j + c_i$ 
        end if
    end for
     $L = L + 1$ 
end while

```

To determine the threshold, τ , a Bayesian approach was used with 120 training sample points randomly selected from each class (partial tree clusters w_1 and complete tree clusters w_2) at the PPINES site. The probability density function (pdf) for each class, (i.e. the likelihood of w_i with respect to x), is estimated using a Parzen windowing approach (Duda *et al.*, 2001), and shown in Figure 4-14. The likelihood $p(x|w_i)$ shows the probability of obtaining a particular feature value x (here, $x = \sigma_z$) given that it belongs to class w_i . The optimal (Bayesian) decision boundary between the two classes, x^* , is selected by minimizing the probability of error (equation 4-5) under the assumption of equal prior probabilities (i.e. $P(w_1) = P(w_2)$). Basically,

the probability of error is minimized by choosing the maximum *a posteriori* probability. That is, by deciding w_1 if $P(w_1 | x) > P(w_2 | x)$ and by deciding w_2 otherwise for a given x . From 100 different subsets of training samples, I observed that the value of x^* was not very sensitive to the particular training samples. I obtained a mean value of 0.62 m for x^* , with a standard deviation of 0.04 m, which is at the noise floor of the LiDAR data (5 ~ 10 cm). The value of 0.62 m was subsequently adopted for τ and used on all plots in the PPINES. This value would have to be trained on each forest among different pine plantation forests to be optimal, but the same value of τ is used in the IMPAC study site in this work to observe the robustness of τ by testing it on data from a plantation that is different from the one used to train τ .

$$x^* = \underset{-\infty \leq x \leq \infty}{\text{Arg min}} [P(\text{error})]$$

$$\text{where } P(\text{error}) = P(w_2) \int_{-\infty}^x p(x | w_2) dx + P(w_1) \int_x^{\infty} p(x | w_1) dx \quad (4-5)$$

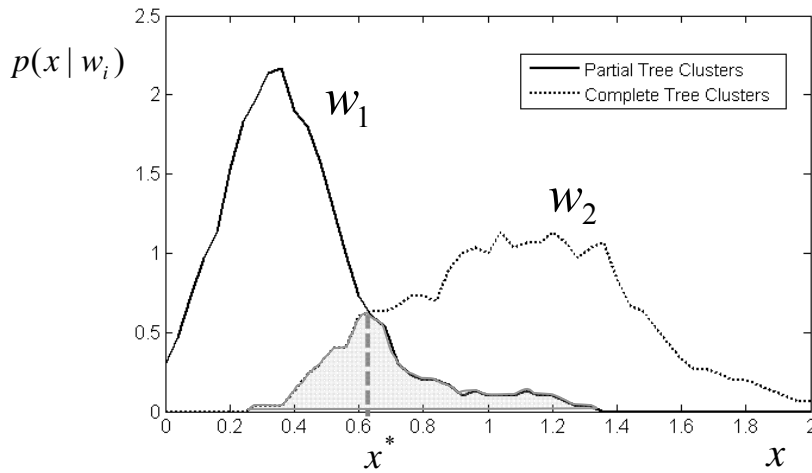


Figure 4-14. Probability density functions of the two classes (w_1 : partial tree clusters, w_2 : complete tree clusters) estimated by the Parzen windowing method. The Bayesian (optimal) decision boundary, x^* , and the resulting probability of error (shaded area) are shown. Here, the random variable x represents the standard deviation (in meters) of heights in the cluster points, σ_z .

The segmentation result over the small area is presented in Figure 4-15. In this example, the algorithm successfully segments nine actual tree canopies, thus revealing the overall efficacy of this approach. Block diagram of the proposed algorithm is shown in Figure 4-16.

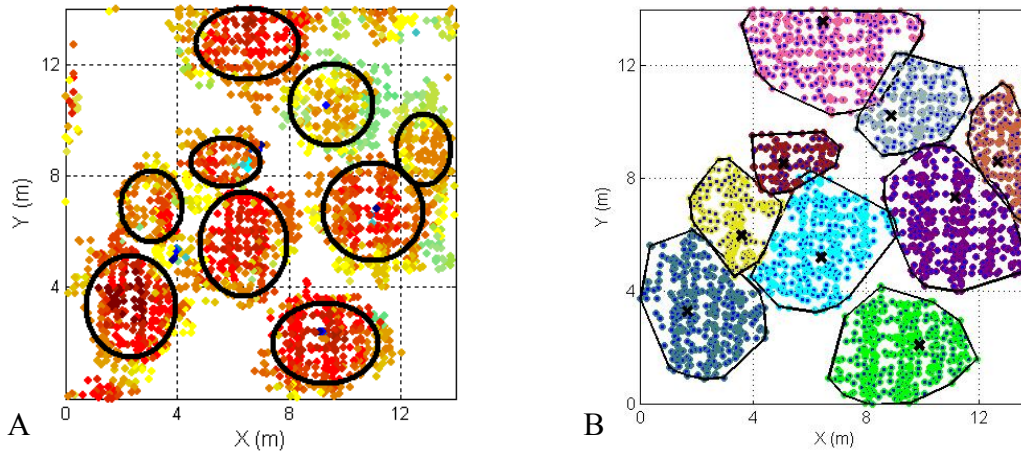


Figure 4-15. The segmentation result over the small area. A) The ground truth showing known locations of nine actual trees with circles. Actual sizes and shapes of the tree canopies are different from those of the circles. B) The segmentation result. A uniform color is used to indicate the set of LiDAR points that are segmented as a given tree. The seed points are marked as crosses, and the maximal boundary of each tree is indicated by convex hulls (closed black curves). Nine actual trees are successfully identified.

4.4 Results and Comparison

The results of the tree segmentations are tabulated in Table 4-4. As shown in Figure 2-3, the canopy distributions differ according to the cultural treatments and the age of plots, and we expect the segmentation results to be dependent on these distributions. The numbers of all trees detected by the algorithm are recorded in the column of ‘Detected’ in Table 4-4. ‘Correct’ is the number of trees that are correctly detected among all detected trees, and their percentages are in the parentheses. ‘Wrong’ is the number of trees detected by the algorithm that do not exist in the ground truth (partial canopies labeled as whole trees), and ‘Missed’ is the number of trees that the algorithm could not detect (whole trees labeled as partial canopies and subsequently merged

into nearest complete trees). The evaluation of the tree detection was based on the measurement plots even though the algorithm detects all the trees inside the treatment plots. The areas on all sides in the treatment plots but not in the measurement plots comprise a buffer zone that mitigates edge effects in the spatial analysis.

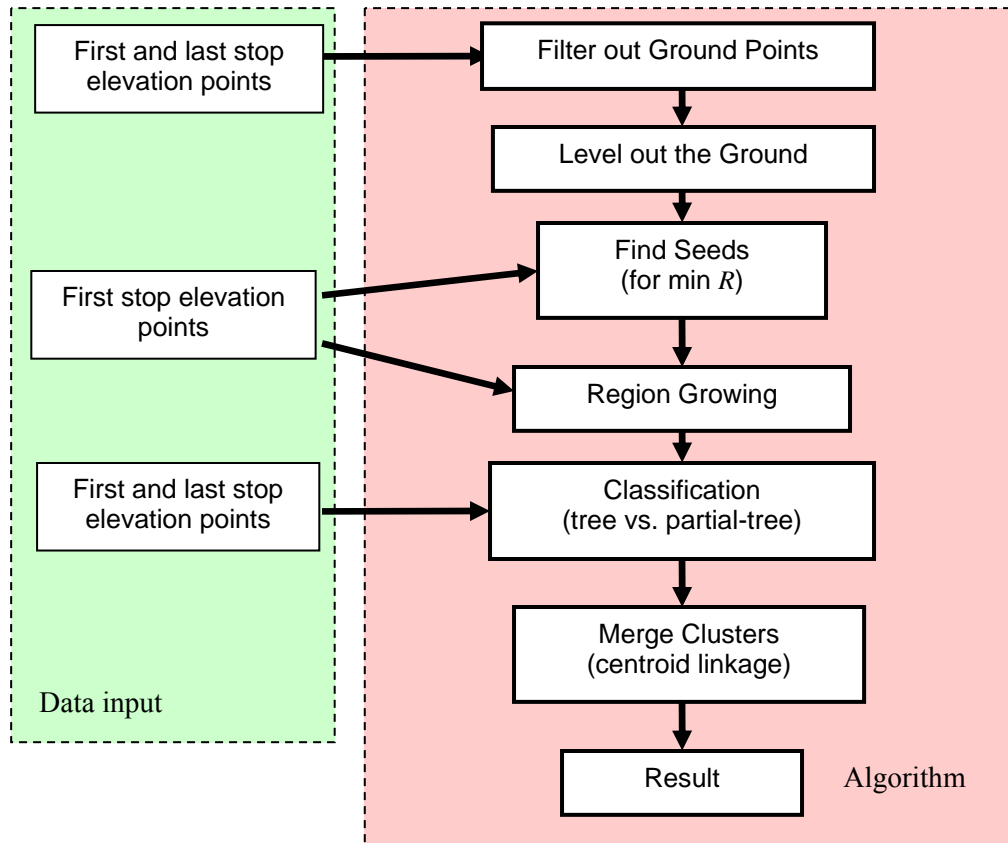


Figure 4-16. Methodology overview of the proposed algorithm.

The overall detection accuracy was $970/1020 = 95.1\%$ with no significant bias (i.e. the number of false positives (57 trees) is similar to the number of false negatives (50 trees)). As expected, the detection accuracy was higher at PPINES since the horizontal distribution of trees was more regular because of the young age of the trees and the square spacing between trees. The plots at the PPINES with low culture showed the best result (98.6%) without significant

bias. In the high culture plots, the trees grew bigger, resulting in more overlap and complexity in the canopy distributions. This caused more occurrences of ‘Wrong’ and ‘Missed’, but the percentage of correctly detected trees (96.9%) was still close to that of the low culture plots. The detection results at the IMPAC plots with high culture were as good as the high culture results at PPINES since fertilization made the older trees at IMPAC bigger and distinct from their neighbors. Also contributing to this high detection accuracy was the fact that fertilization over the long duration of the IMPAC plots eventually resulted in instances of competitive tree mortality (Table 4-4), which increased some of the gaps between trees. The lowest detection accuracy occurred for the case of the low culture plots at IMPAC (84.0%). Unlike at PPINES, the IMPAC plots with low culture had less tree mortality (more closely packed trees) and more irregularity in canopy size and shape. Several difficult cases were also observed in these plots where small trees were leaning towards nearby taller trees and parts of their canopies were underneath or inside neighboring trees.

Table 4-4. Results of individual tree segmentation. Here, H = High culture, L = Low culture. High cultural intensity attempts to maximize growth and health of the trees through fertilization and control of understory vegetation. Low cultural intensity does not.

Site	Plot Type	Number of Plots	Number of Planted Trees	Number of Living Trees	Result			
					Detected	Correct	Wrong	Missed
PPINES	H	8	384	351	367	340 (96.9%)	27	11
	L	8	384	354	356	349 (98.6%)	7	5
IMPAC	H	6	240	134	150	129 (96.3%)	21	5
	L	6	240	181	154	152 (84.0%)	2	29
Total	--	28	1248	1020	1027	970 (95.1%)	57	50

A segmentation result on a plot at the PPINES with high culture is shown in Figure 4-17. Odd-shaped tree canopies are successfully detected because no assumptions are made on

horizontal canopy morphology. The treetop, tree boundary, and LiDAR points of each tree are shown in the figure. Two false positives and one false negative are found in the measurement plot.

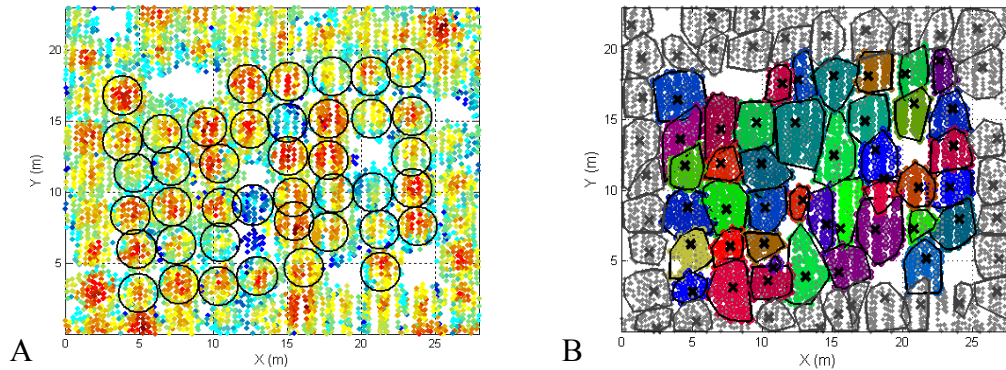


Figure 4-17. An example of the segmentation results (a plot with high culture at PPINES). A) Known tree locations are manually circled on top of the first-stop elevation points where the ground points are filtered out. Actual sizes and shapes of the tree canopies are different from those of the circles. B) The segmentation result. A uniform color is used to indicate the set of LiDAR points that are segmented as a given tree inside the measurement plot. The seed points are marked as crosses, and the maximal boundary of each tree is indicated by convex hulls (closed black curves). Detected trees that lie outside the measurement plot are shown with grey crosses and lines.

The same study sites are tested by the scale-space method mentioned in section 4.2 (Table 4-5), and the detection result is compared with the result by the proposed method (Figure 4-18). There is no big difference between the two methods in detection accuracy at PPINES because of relatively less complex of the spatial distribution of trees and closer to Gaussian distribution of the tree crowns. However, the accuracy by scale-space method drops more rapidly than the accuracy by the proposed method as the test site becomes complicated. The accuracy by the scale-space method drops more than 10% at IMPAC compared to the accuracy by the proposed method. In addition, the scale-space method produces more false positives (92 trees) and false negatives (85 trees) overall.

Table 4-5. Results of individual tree segmentation by the scale-space method. Here, H = High culture, L = Low culture.

Site	Plot Type	Number of Plots	Number of Planted Trees	Number of Living Trees	Result			
					Detected	Correct	Wrong	Missed
PPINES	H	8	384	351	378	343 (97.7%)	35	8
	L	8	384	354	366	348 (98.3%)	18	6
IMPAC	H	6	240	134	142	115 (85.8%)	27	19
	L	6	240	181	141	129 (71.3%)	12	52
Total	--	28	1248	1020	1027	935 (91.7%)	92	85

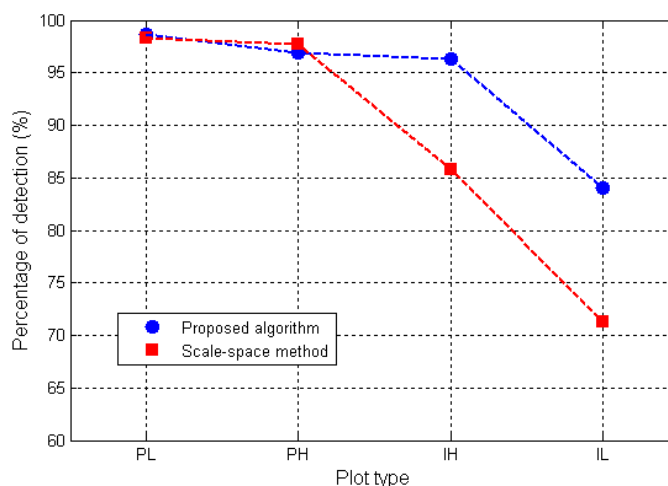


Figure 4-18. Performance comparison between the proposed method (blue) and the scale-space method (red) based on Tables 4-4 and 4-5. Plot codes: PL = low culture at PPINES, PH = high culture at PPINES, IH = high culture at IMPAC, and IL = low culture at IMPAC.

4.5 Discussion

Using the proposed approach, I obtained overall tree detection accuracies in excess of 95% over the two test sites (Table 4-4). The only exception was the set of low culture treatment plots at IMPAC, where a fairly good detection accuracy of 84% was still achieved. As mentioned in the previous section, those plots exhibited considerable intermingling among adjacent canopies

and greater variation in canopy size and shape than the other plots. The detection accuracy in the set of high culture treatment plots at IMPAC was high and close to that for the plots at PPINES even though τ was trained on PPINES, providing evidence of the robustness of τ . In general, lower detection accuracy at a testing site (site at which τ was not trained) could be attributed to either greater structural complexity at the testing site or simply the fact that τ was not trained at the testing site. But here, we see good performance at IMPAC with high culture, similar to that at PPINES. Thus, it appears that the detection accuracy was mainly affected by the complexity of the tree canopies in the low culture IMPAC site. The small standard deviation in x^* across multiple randomized samplings of the training data suggests that the parameterization in the clustering step is robust and could be applied to other managed sites of different tree ages, stem spacings, or species using only modest amounts of training data. This is an important observation because the availability of high resolution remote sensing data sets, (in particular LiDAR data sets) over sites with ample ground-truth is often limited. As a result, one cannot generally run a large number of inter-comparisons of estimation performance across different sites, as is often done in other estimation or pattern recognition studies in which data is not so limited.

Even though the scale-space method shows high accuracy at PPINES where the trees are well apart and the crown shapes are close to Gaussian distribution, there are some caveats in this method: (1) The scale-space method needs a preprocessing to convert 3D point clouds into a 2D smooth image by giving up more detail information of LiDAR points. Moreover, a reverse step is needed, after segmenting individual tree crowns, to recover the individual tree LiDAR points which are necessary to estimate tree parameters such as tree heights and crown lengths. (2) Another drawback of scale-space method is finding the local extrema at each level. This is a chicken-and-egg problem since it is similar to the problem of finding the right size of R

mentioned in section 4.3.2. (3) As seen in the Figure 4-3, the local maxima drift as scale changes. This drifting phenomenon becomes severe as the scale parameter gets larger, and the blobs in the bigger scales generally have high scale-space signature. The algorithm chooses the strong blobs rather than following weaker blobs which have more accurate locations. (4) Besides the drifting phenomenon, it is not a trivial problem to decide if the current blob is overlapped with previously chosen blobs since another search region should be determined for this task.

Flying multiple times over a particular ROI is generally necessary to obtain high densities of laser points ($10 - 20$ points/m²) given the current constraints on minimum flight speed, minimum allowable flying altitude, maximum laser pulse rate, and maximum scanner frequency. Although, increasingly high laser pulse rates of new LiDAR systems can reduce somewhat the need for multiple flight lines (Slatton *et al.*, 2007). Unlike the flights over IMPAC, only horizontal (East-West) flights were acquired over PPINES. As shown in Figure 4-19, this resulted in narrow vertical (North-South) gaps that are visible in the point clouds between scan lines. While the overall tree detection accuracy was high in spite of this phenomenon, in general such gaps can cause difficulty in detecting trees if a tree happens to be separated into a multiple clusters by a gap. The worst case scenario would be when the scan lines from multiple flights overlap almost exactly rather than one flight “filling in” the gaps from another. Therefore, when researchers have input on the design of the flight plan, orthogonal flight lines should be requested to get better coverage over the ROI.

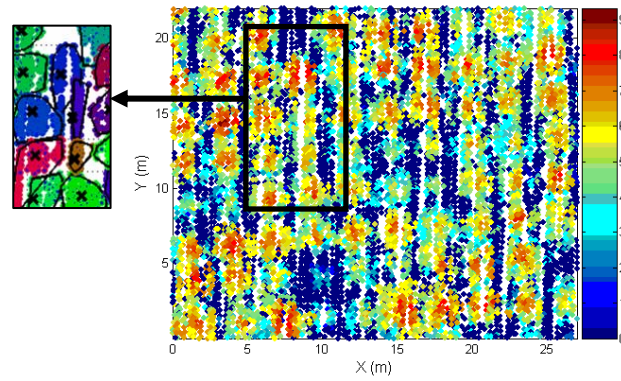


Figure 4-19. A top view of the low culture PPINES plot shown in Figure 2-3. The aircraft was flying East-West (right-left in the figure) over the site. Narrow gaps roughly 1m or less in width are visible (marked with a rectangle) in the point data between scan lines even though partially-overlapping flight lines were acquired. A subset of the detection result is shown inside the small box to the left. While such gaps do not seem to strongly affect the correct detection of the trees, they can affect the estimated shapes of the detected canopies and estimates of HT and CL in cases where the highest points on the trees are missed. Orthogonal flight lines could mitigate such gaps.

CHAPTER 5 FOREST PARAMETER ESTIMATION

5.1 Introduction

Once individual trees are detected, the possibility is opened up to estimate important parameters such as the number density of trees, tree height, crown length, and crown area directly from the segmented points. From these parameters, other forest parameters, such as diameter at breast height (DBH), basal area, and leaf area index (LAI) could be estimated from allometric equations (Amaro *et al.*, 2003; Song, 2007). The focus on this chapter is estimations of two parameters for which I had *in situ* measured values from a ground survey, tree height (HT) and crown length (CL).

5.2 Estimation of Tree Height and Crown Length

5.2.1 Tree Height (HT)

The highest point among the segmented points for each tree is considered as the treetop, and the distance to the treetop from the ground is regarded as the height of that tree (Figure 5-1). The accuracy of this depends primarily on the density of LiDAR points since the laser beam divergence is very narrow, the height error from UF-ALSM measurements is at the decimeter scale (Shrestha *et al.*, 1999), and the error in the estimation of bare-surface ground elevation (Cho and Slatton, 2007) rarely exceeds two or three decimeters. If the point density is very low, it is likely that the system will miss the actual treetop thereby resulting in underestimation of the true maximum height.

5.2.2 Crown Length (CL)

In the field work, foresters are interested in 'effective' crown length. A whorl is a common feature of pine trees and is defined as a cluster of branches that radially come from the main trunk at roughly the same height. The base of the live crown can be defined as the lowest whorl

with 50% or more of the branches containing live green needles. As a tree ages, the older (lower) whorls become shaded by the newer whorls on that tree. This trend is emphasized in managed forests where all trees are at the same stage, so shading on older whorls by neighboring trees of similar heights increases with time. As the whorls age and lose sun exposure, they die and over time the base of the live crown moves up as the tree height increases (Long *et al.*, 2004). Crown length can be computed simply by subtracting the height to the base of the live crown (HTLC) from HT (Figure 5-1).

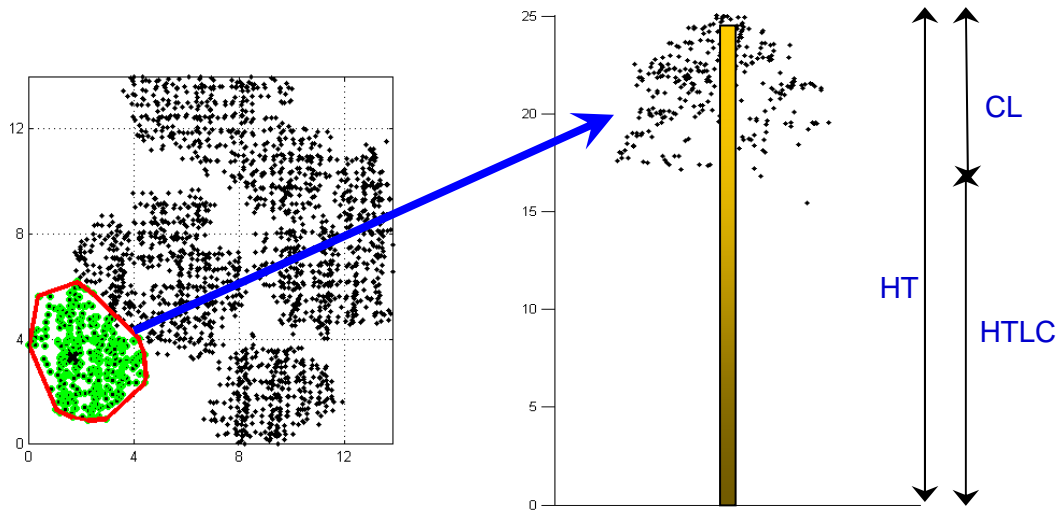


Figure 5-1. An illustration of estimates of HT, HTLC, and CL on segmented LiDAR points. An estimate of the vertical projection of maximal crown area for a segmented tree is circumscribed by a convex hull (closed red curves), and the estimated location of a tree stem is indicated by a brown bar.

The base of the live crown is usually difficult to estimate since the lower limit of the canopy is not always obvious because LiDAR points can hit the stems (trunks) and dead branches. In this work, owing to absence of understory vegetation, a simple method is developed. By smoothing the vertical distribution of non-ground LiDAR points (both first and last returns),

the height where a significant number of points first appear in a given tree cluster can be found. A 2 m long sliding window was incremented up from the ground in 1 m intervals at each tree cluster, and the number of points in the window is counted. When the number of points in the window first exceeds more than 1% of the total number of points in that cluster, the median height of the LiDAR points in the window is recorded as the HTLC of that tree.

5.3 Results and Discussion

From the IMPAC site, I was able to use all trees in the 12 plots to estimate HT and CL because the ground truth survey included all trees. It was thus possible to examine two cases for IMPAC. In the first case (Case 1), only correctly detected trees are used, that is, falsely detected trees and missed trees are not counted. In the second case (Case 2), all trees segmented by the algorithm are used for the experiment. Case 2 is more general since it is not always known beforehand if a segmented tree is classified correctly or not. Unfortunately, at PPINES only 25% of the trees in each plot (except 2 plots) were selected to measure the parameters during the ground survey. So at PPINES, I used all correctly detected trees (83 trees) in two plots and a random sampling of 140 correctly detected trees from the remaining 14 plots. As a result, wrongly detected trees and missed trees could not be included in the PPINES results. The differences between estimates and ground truth values for HT and CL are summarized in Table 5-1.

5.3.1 Tree Height

For the PPINES site, the mean of all ground truth tree heights was 7.95 m, and the mean of all estimated tree heights was 7.71 m. The mean of absolute height differences between the ground truths and the estimates was 0.34 m (percentage of error = $\pm 4.22\%$) and the standard deviation was 0.29 m.

Table 5-1. The mean differences between the ground truth values and the estimates of HT and CL. The standard deviations are given in parentheses. Because the ground survey at IMPAC was exhaustive, two different cases could be studied: (1) Case 1: only correctly detected trees are used, and (2) Case 2: all trees segmented by the algorithm are used. Only Case 1 could be studied at PPINES because the ground survey was based on randomized sampling rather than exhaustive.

	Tree Height (HT)			Crown Length (CL)		
	Case 1	Case 2		Case 1	Case 2	
		Whole	Each plot		Whole	Each plot
PPINES	0.34m (0.29m)	--	--	0.84m (0.58m)	--	--
IMPAC	0.78m (0.63m)	0.58m	0.60m (0.44m)	1.40m (0.97m)	0.39m	0.81m (0.69m)

For all correctly detected trees in IMPAC (i.e. Case 1), the mean of all ground truth tree heights was 22.00 m, and the mean of all estimated tree heights was 21.85 m. The mean of absolute height differences was 0.78 m (percentage of error = $\pm 3.55\%$) and the standard deviation of them was 0.63 m. For Case 2, over the whole (all 12 plots), the mean of all ground truth heights was 21.34 m and mean of all estimated heights was 21.92 m. Interestingly, this difference (0.58 m) was smaller than the difference achieved in the first case. This shows that there is a good agreement between the mean of all ground truth and the mean of all estimates (from all detected trees) at this site even though the algorithm misses some trees and detects some false trees. To look at a smaller size of ROI, the same experiment was executed for individual plots (0.027 ha), and the result still shows good agreement but slightly larger errors; the mean of difference between ground truth and estimates of each of the 12 plots was 0.60 m and the standard deviation was 0.44 m. While it is possible in general for large errors to occur locally, these results imply that one could reasonably expect good average agreement with ground truth even over small plots, such as these.

5.3.2 Crown Length

For the PPINES site, the mean of all ground truth crown lengths was 5.51 m, and the mean of all estimated crown lengths was 5.04 m. The mean of absolute CL differences between the ground truths and the estimates was 0.84 m and the standard deviation was 0.58 m.

For IMPAC, in Case 1, the mean of all ground truth crown lengths was 6.39 m, and the mean of all estimated crown lengths was 6.01 m. The mean of absolute CL differences was 1.40 m and the standard deviation was 0.97 m. In Case 2, the mean of all ground truths was 6.18 m and mean of all estimates was 5.79 m. As seen the trend in HT estimation, this difference (0.39 m) is smaller than the difference in Case 1 showing that there is a good agreement between the mean of all ground truths and the mean of all estimates over the test area. Based on the individual plots for a smaller size of ROI, the mean of difference between ground truths and estimates of each of the 12 plots was 0.81m and the standard deviation was 0.69 m.

5.3.3 Underestimation of the Parameters

In the subsequent parameter estimation, I also obtained agreement between estimates and ground truth to within several decimeters. The average tree height was underestimated by 0.24 m and 0.15 m over PPINES and IMPAC, respectively. Much of this residual is likely caused by instances where the LiDAR did not happen to hit the top most point of some crowns. There was more chance of missing the treetops over PPINES because the peaks of the crowns tended to be sharper over PPINES than over IMPAC resulting in larger underestimation for HT over PPINES. The average crown lengths were underestimated by 0.47 m and 0.38 m over PPINES and IMPAC, respectively. The slightly larger estimation error for CL is not surprising since CL estimates depend on both the estimated HT and how well the lower canopy is sampled. The occluding effect of the upper canopy implies that the lower canopy is not sampled as densely as the upper canopy. The underestimate of CL at PPINES was slightly larger than at IMPAC. The

most likely reason for this is that the younger tree canopies in PPINES are shorter and thicker resulting in less penetration of the LiDAR. Furthermore, there is always some uncertainty in the field measurements themselves because of irregularities in the terrain surface and measurement errors. In these study sites, the terrain is quite flat, so any errors that may be present in the ground surveys are most likely due to random measurement errors by field personnel.

5.3.4 Impact of LiDAR Point Density

Over the range of LiDAR point densities examined here (10 – 20 points/m²), the RMS errors in the estimates decreased with increasing density for both the tree heights and crown lengths (roughly 0.5 m to 0.1 m for HT and 1.1 m to 0.3 m for CL for 10 to 20 points/m², respectively). This suggests that high LiDAR point densities are important for accurate estimation of individual tree parameters. In particular, as mentioned in the previous section, higher point densities increase the chances of a LiDAR return from the highest point in each tree canopy, thus reducing underestimation of tree height. It would be potentially interesting to determine minimal LiDAR point densities that could still yield useful estimates in order to acquire LiDAR data most efficiently. However, general statements along those lines are problematic because the degree to which lower LiDAR point densities would be useful would depend on the flight pattern (presence of orthogonal flight lines), forest type, parameters being estimated, and the tolerance for uncertainty for the particular application.

5.4 Other Parameters

5.4.1 Crown Area

Based on the segmented LiDAR points, estimates of the vertical projection of maximal crown area for each segmented tree could be obtained using the circumscribing convex hulls computed for each crown cluster (Figure 5-1). Similarly, the 3D shape of the upper crown “surface” of each tree could be estimated since the LiDAR points provide height information

along with horizontal positions. However, I do not present formal estimates of crown area or shape here since they were not independently measured in the ground survey.

5.4.2 Diameter at Breast Height (DBH)

The diameter at breast height (DBH) is one of the most important parameters in forest inventories. Usually the tree height correlates strongly with stem diameter and height can be assessed accurately with a laser scanner as shown in section 5.3. A simple empirical DBH model for loblolly and slash pines using the regression formula in equation 5-1 could be developed on the basis of field measurements of tree height and crown diameter (CD).

$$DBH = \alpha \times HT + \beta \times CD + \gamma \quad (5-1)$$

where coefficients α , β , and γ can be calibrated using local field inventory data.

5.4.3 2-Dimensional Open Gaps

There are many ways of quantifying the 2-dim gaps over a forested area. The simplest method is computing the ratio of non-vegetation area to the whole area. This is a straight forward computation since the non-vegetation area is the complement of the area of the detected trees in Chapter 4. Simply, it would be ‘max(gap)=1’ in the case of no vegetation in the area, and ‘min(gap)=0’ when vegetation covers the whole area.

However, the area ratio method described above fails to count the canopy density. Although it is very difficult to have accurate canopy density from LiDAR data due to lack of LiDAR penetration in understory in thick forest, we can still use some information from LiDAR data which shows some difference between dense canopy and sparse canopy; we have less non-ground LiDAR points on sparse canopy because more points penetrate the canopy and reach the ground. Therefore, instead of considering the vegetation area uniformly, we can compute 2D pdf of ALSM points in the area by using a non-parametric approach such as Parzen window method.

It would be a good supplement to compute lacunarity as an overall parameter for the interest area since ‘area ratio’ or ‘2D pdf’ does not inform of the distribution of the gaps. Mandelbrot (1982) introduced the concept of lacunarity as a quantitative measure of the distribution of gap sizes, and is also used in texture analysis (Dobson *et al.*, 1997; Limas Serafim, 1997; Du and Yeo, 2002). Lacunarity was developed to cover the case of fractals that have different appearances even though they are constructed with identical fractal dimensions. Large lacunarity implies large gap and clumping of points, and small lacunarity implies a more uniform distribution of gap sizes. The range of lacunarity is between 0 and infinity.

5.4.4 3-Dimensional Open Gaps

Three dimensional gaps can be more precisely defined if we know the full canopy structure. Since ALSM describes the upperstory canopy structure very well, open gap towards zenith sky that is related to GPS (L-band) microwave attenuation and personnel detectability from the sky can be computed. Figure 5-2 shows an example of using 3D gap to compute the maximum possible open angles at locations on the ground. The open angle θ , is calculated at 90% confidence level assuming that the observer is at 2 m above ground level, moving inside the measurement plot at 1 m intervals. The ALSM points that cover the circle area of the cone scope are used to compute the confidence level. That is, the angle θ is increased until the ALSM point coverage on the circle area of the cone scope reaches 10% of the circle area. A weight was given to the point inside the cone scope depending on the height of the point since lower points inside the cone scope contribute more towards blocking the visibility than higher points. In Figure 5-2 (c), we clearly see the high open angle where big open gaps (no tree near around) exist.

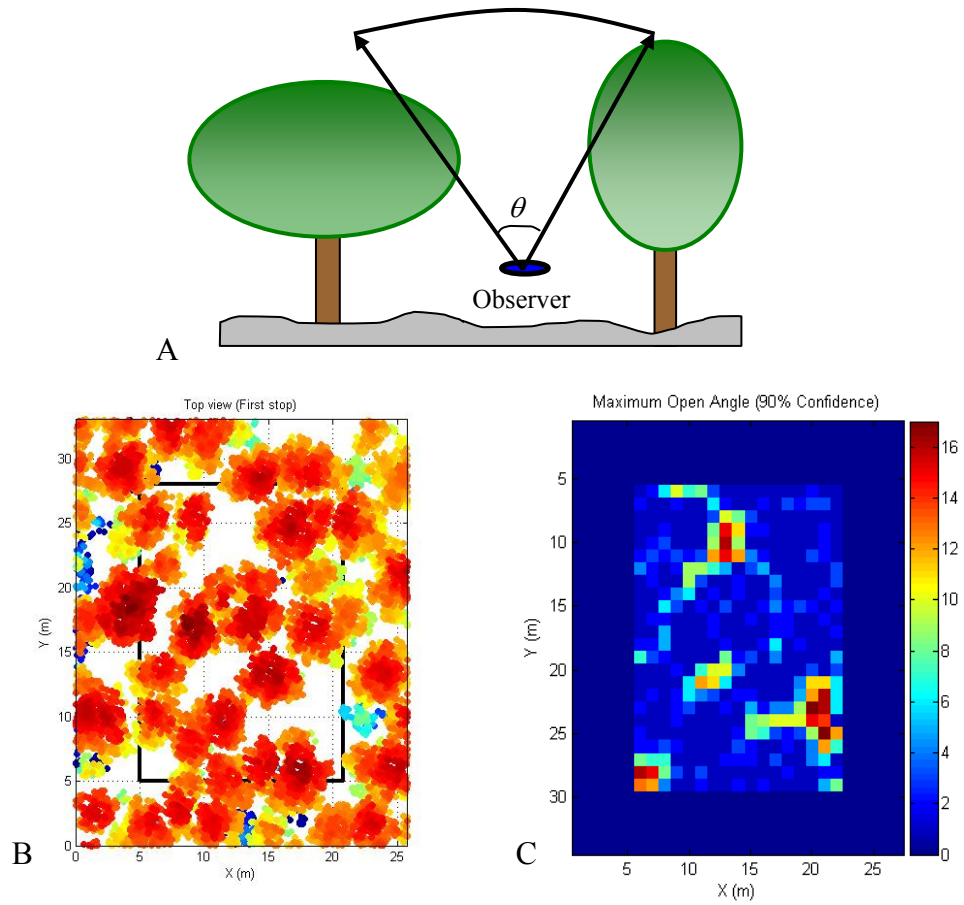


Figure 5-2. An example of the maximum possible open angles at locations on the ground. A) Illustration of upward open gap from an observer. B) A plot in the IMPAC site. C) Maximum possible open angle at the 90% confidence (observer level = 2 m from the ground).

CHAPTER 6 SPIN IMAGES OF DIFFUSE TARGETS

6.1 Motivation

Geometric structures of individual trees are one of the most interests to forest researchers, but it is usually difficult to have them from overhead image sensors. However, due to some penetration through canopies of ALSM points and their precisely located 3D measurements, there will be some ways of showing vertical (side-view) differences between different canopy classes. In this chapter, spin images are computed to see the possible discrimination between the different geometric structures of the segmented clusters.

Spin images developed by Johnson and Hebert (Johnson, 1997; Johnson and Hebert, 1999) are a 3D point matching method based on shape characteristics only. Spin images have some attractive characteristics, such as invariance to rigid transformations (rotation, scale, and pose), limited sensitivity to variations of position of mesh vertices, flexibility (since no hypotheses are made on the surface representation), and ease of computation. This method has been successfully applied to shape matching (Johnson and Hebert, 1998; Johnson, 2000) and 3D object retrieval (Assfalg *et al.*, 2004), and textured spin images were recently introduced to include texture information (Brusco *et al.*, 2005).

It is a new attempt to use spin images on diffuse targets such as tree canopies described in this study, and there are a couple of advantages of using spin images for this application: (1) ALSM points are not evenly distributed on the canopies because the spot dispersal created by the oscillating mirror creates a saw-toothed pattern on the ground, and because of the combining of multiple flight lines. Also, trees that are viewed near the edges of the ALSM imaging swath are partially occluded (i.e. the opposite side of the canopy from the laser direction has very sparse point density at high scan angles). Therefore, instead of using the raw point distribution,

‘spinning’ around the tree stem mitigates these irregularities. (2) Tree canopies are inherently irregular targets, so we desire many realizations to characterize the canopies. Spin images are expected to reduce overall sensitivity to these irregularities and increase the discrimination between profiles of different canopy structures. Therefore, for example, comparing spin images of the segmented clusters in Chapter 4 could be another way of classifying small tree canopies from partial-tree clusters at the expense of more complexity and computational cost (but more detail vertical structures).

6.2 Spin Images

Creation of a spin image begins from an oriented point that is a 3D point associated with a direction. Usually, an oriented point is defined at a surface mesh vertex using the 3D position of the vertex and surface normal at the vertex. An oriented point defines a partial, object-centered, coordinate system. Two cylindrical coordinates are defined with respect to an oriented point: the radial coordinate α , defined as the perpendicular distance to a line along the surface normal vector \bar{n} , and the elevation coordinate β , defined as the signed perpendicular distance to the tangent plane defined by vertex normal and position (Figure 6-1). In Figure 6-1, \bar{p} is a point on the surface of the object and \bar{n} is the normal of the tangent plane in \bar{p} . For an oriented point, $O = \langle \bar{p}, \bar{n} \rangle$, a spin map is defined by mapping any point \bar{x} in the 3-D space onto a 2-D space according to the equation 6-1, where the set of spin image pixel values is denoted by S_o such that $S_o = R^3 \rightarrow R^2$.

$$S_o(\bar{x}) \rightarrow [\alpha, \beta] = \left[\sqrt{\|\bar{x} - \bar{p}\|^2 - (\bar{n} \cdot (\bar{x} - \bar{p}))^2}, \bar{n} \cdot (\bar{x} - \bar{p}) \right] \quad (6-1)$$

In other words, the oriented point defines a family of cylindrical coordinate systems, with the origin in \bar{p} , and with the axis along \bar{n} . The spin map projection of \bar{x} retains the radial distance

(α) and the elevation (β), while it discards the polar angle. This projection ensures that, for any given oriented point, a unique spin map exists. The projected coordinates α and β of each mesh vertex are used to construct the spin images.

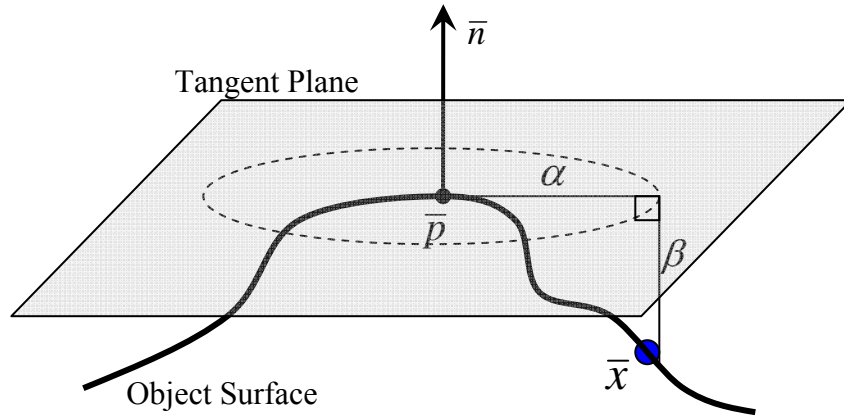


Figure 6-1. The object centered 3-D coordinate system to create a spin image. The (α, β) coordinates provide a 2D index of a surface point \bar{x} relative to the oriented point \bar{p} .

6.3 Creating Spin Images from ALSM Points

The process in this application could be somewhat different from the process that was originally developed since the oriented points can be defined as just the treetop points of each cluster. By defining them, it greatly reduces the amount of computation needed in the original algorithm such as computing the surface mesh vertices, computing surface normal at each vertex, and considering each surface mesh vertex as an oriented point. Another big difference is that the sizes of the spin images can be fixed since initial canopy clusters are already segmented. Choosing the size of spin image is an issue in many other applications since it strongly affects the result a lot. In this work, I fixed the size of the spin images ($\alpha \times \beta$) as $4 \text{ m} \times 10 \text{ m}$ with the grid size of 0.5 m resulting in $8 \text{ pixel} \times 20 \text{ pixel}$ images (Figure 6-2). However, there is a

problem with fixing the size of images since the sizes of canopies of the segmented clusters varies a lot. This may not be a problem if many samples (i.e. clusters) from each class can be created, but creating many training samples is not easy for this application. Furthermore, the shape of the crown is more important than the size of the canopy for characterizing different tree crowns. This problem is easily solved by scaling the range of the ALSM points in the cluster to fit in the spin image range, $[0 \text{ m}, 4 \text{ m}]$. By doing this, the size of canopies is no longer an issue. For the β -axis of the spin image, I limited the range to be $[H, H - 10 \text{ m}]$ where H is the height of the treetop points. In this way, ALSM points that are lower than 10 m from the treetop are not considered. This allows us to take most of the main canopy points into account, and remove the contribution of understory objects.

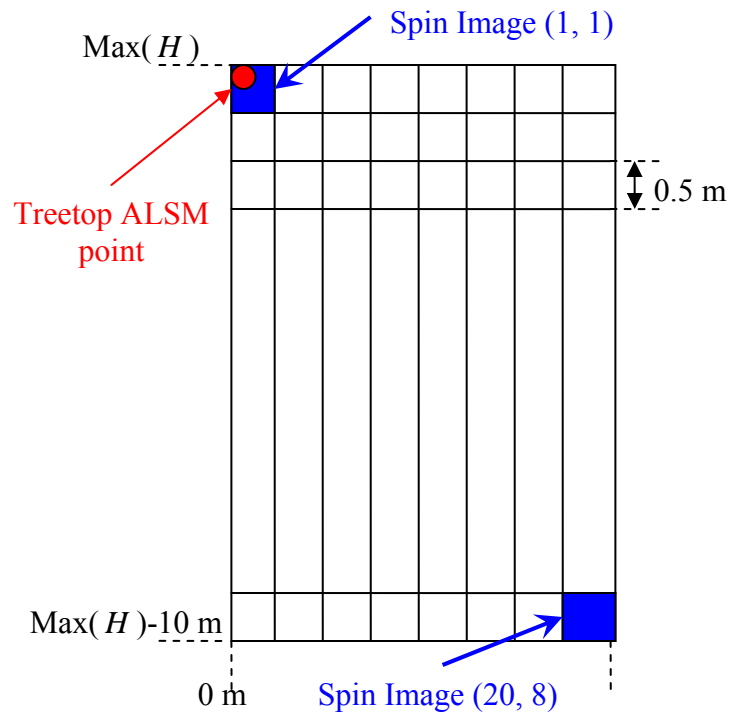


Figure 6-2. Selection of the size of spin image. The size of spin image is fixed as 8×20 with grid size of 0.5 m. The α -axis is the horizontal axis, and the β -axis is the vertical axis.

One of the disadvantages of the standard spin images algorithm is that the density of the data points must be uniform across the surfaces being compared (Dinh and Kropac, 2006). This issue occurs in the application here because there are different numbers of ALSM points in each cluster. The local point density varies a lot, and the size difference of canopies creates different number of points in each cluster. Again, this may not present a big problem if we could create many spin images for many cases with different number of points, but that would require an unrealistic number of training examples. Therefore, to make fair comparisons between spin images, the number of points in each cluster is normalized.

Figure 6-3 shows an example of a spin image of a full tree cluster. Figure 6-3 (A) shows just the points that are spun and mapped onto 2D. The spin-map of the cluster (Figure 6-3 (B)) is created by using the image size that is defined above, and the corresponding spin image is shown in Figure 6-3 (C). The idea of accumulating the points of the spin-map into discrete bins is equivalent to a linear smoothing of the spin-map with an impulse response of value one over the bin and zero elsewhere. In the spin image, the gray values are associated to the counts of points in the spin-map falling in each discrete bin (white color = zero points, darker color = more points).

Unlike the application of spin image to arbitrary 3D object recognition from any vantage point, the application here is considered as a special case for three reasons: (1) There is no full description of the model (no expected closed-form geometric shape). The query points (or cluster), and model as well, are always from the partial view (i.e. downward-looking from the sky). This partial view makes it harder to distinguish the objects, but it makes the spin image computation easier. (2) Whole tree canopies or portions of tree canopies are segmented via the adaptive region growing algorithm in Chapter 4 before the spin image computation. This greatly

reduces the computation load since a single spin image is needed per cluster by centering the spin image at the seed point of the cluster. Thus, computing a spin image at each and every point is not necessary. (3) The LiDAR data can be exploited much more fully by using both first and last stops and other features including intensity values. By these extra features, the standard spin images can be extended to better characterize diffuse objects.

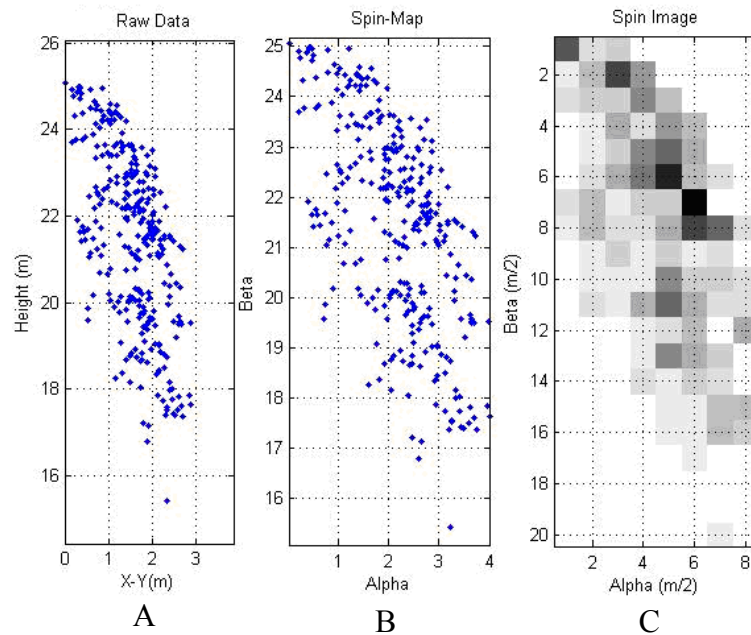


Figure 6-3. An example of a spin image of a full tree cluster. A) The raw points are spun with respect to the oriented point. Units are in meters. B) The spin-map. Units are in half-meters. C) The spin image of the cluster. Units are in half-meters.

6.4 Spin Images of Canopy Clusters

The spin images of 12 initial clusters in the small test area at the IMPAC site (Figure 4-12) are created and shown in Figure 6-4. Cluster #1, 2, 3, and 6 are ‘tree’ clusters, and the other clusters are ‘partial-tree’ clusters. The maximum pixel value in the whole spin image set occurred in cluster #9. The numbers of points in each pixel are normalized by this maximum

value. In the spin images of the tree clusters, we see that the points are spread diagonally from the upper left to the lower right portions of the image. Cluster #5, 9, and 10 are partial-tree clusters representing small portions of the tree canopies, and the spin images are quite different from the general spin images of tree clusters. Many points are located on the top portion of the images and the pixel values are spiky suggesting that good separation between the complete trees and partial trees could be achieved. Clusters #4, 7, 8, 12, and 13 are partial-tree clusters representing large portions of the tree canopies and present spin images that exhibit intermediate values between the two cases of ‘full tree clusters’ and ‘small canopy portion clusters’.

As another example, in Figure 6-5, two spin images are created from each three different classes; PPINES with low culture treatment (PPINES-L), PPINES with high culture treatment (PPINES-H), and IMPAC. To take the differences of actual canopy sizes into consideration, the range of α -axis is not scaled here. Most of the points in the cluster at PPINES-L, as shown in Figure 6-5 (A), are located right near the stem showing very narrow cone shape of the tree crown. The spin images of the clusters at IMPAC, Figure 6-5 (C), show that the distribution of the pixels is smoother unlike the spiky distribution of the clusters at PPINES-L. We also see wider cone shapes with more voids inside the crowns. The spin image shapes of the clusters at PPINES-H are intermediate between the two other classes, but closer to the spin images of the clusters at PPINES-L.

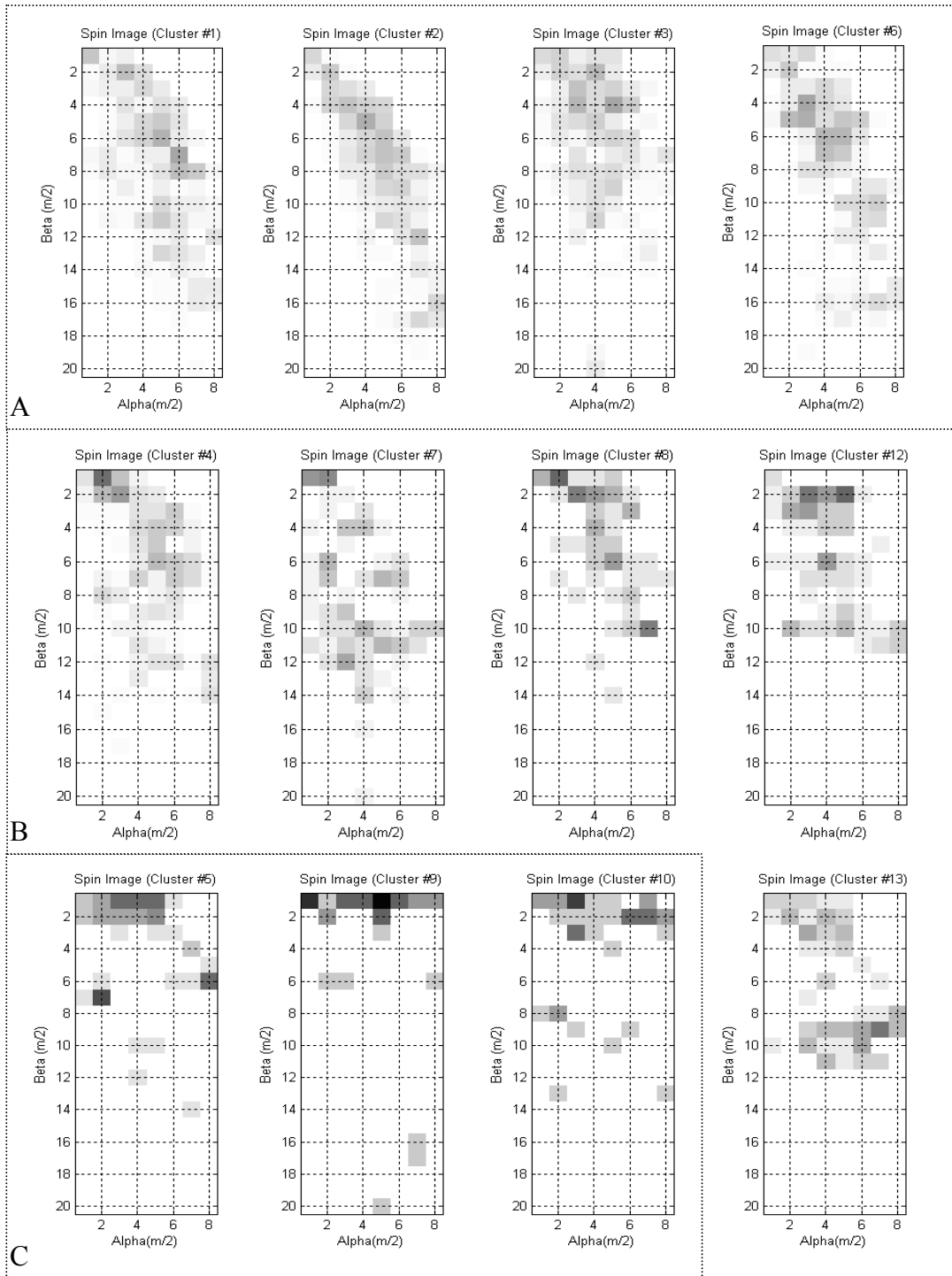


Figure 6-4. Spin images of each cluster in Figure 4-12. A) Clusters #1, 2, 3, and 6 are ‘tree’ clusters. B) Clusters #4, 7, 8, 12, and 13 are ‘non-tree’ clusters, but they correspond to large fractions of the tree canopies. C) Clusters #5, 9, and 10 are also ‘non-tree’ clusters, and they correspond to small fractions of the tree canopies. (The cluster number on each cluster is shown in Figure 4-12.) All units are in half-meters.

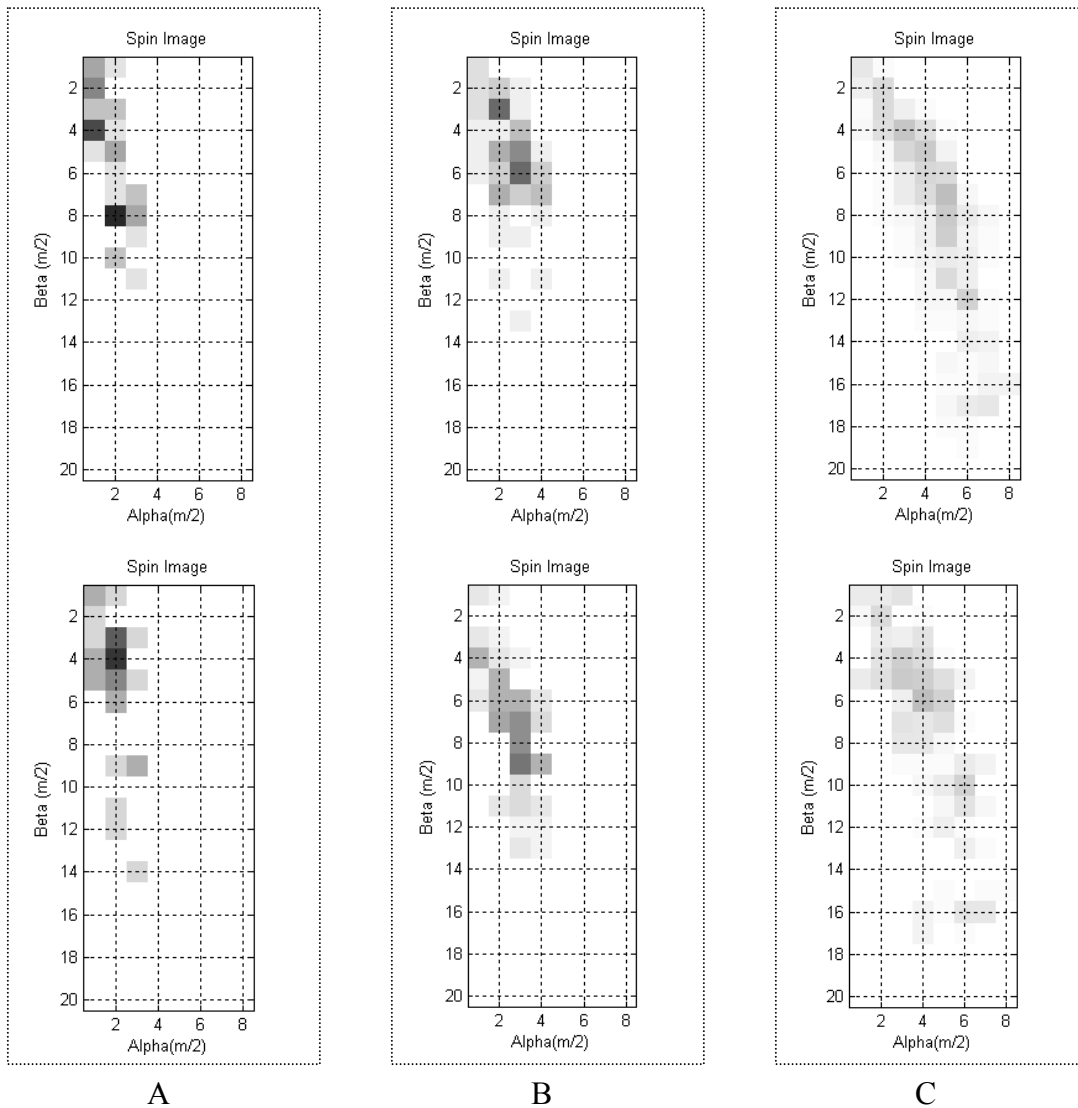


Figure 6-5. Spin images of tree clusters from three different classes. A) A cluster at PPINES with low culture treatment. B) A cluster at PPINES with high culture treatment. C) A cluster at IMPAC.

It is promising that, in many cases, spin images provide good separation between different tree structures. For the training processes, in the future, the spin image of each sample from each set of clusters could be computed and stored in the model library. To classify a given cluster, the spin image of the given cluster is generated and compared to all the stored spin images to find the most highly correlated image using a template matching scheme. The standard

way of computing linearly related images is the normalized linear correlation coefficient. Given two images P and Q with N bins each, the linear correlation coefficient $R(P, Q)$ is shown in equation 6-2 (Johnson 1997).

$$R(P, Q) = \frac{N \sum p_i q_i - \sum p_i \sum q_i}{\sqrt{(N \sum p_i^2 - (\sum p_i)^2)(N \sum q_i^2 - (\sum q_i)^2)}} \quad (6-2)$$

R , ranging between -1 (anti-correlation) and +1 (completely correlated), measures the normalized error using the distance between the data and the best least squares fit line to the data. The images are similar when R is high and not similar when R is low. The correlation coefficient imposes an ordering on point correspondences, so the spin image that gives the highest value of R is selected.

It should be noted that over modest sized areas, such as IMPAC and PPINES, this correlation comparison could be done between the considered spin image and every training spin image, as suggested above. For larger areas, however, it would be more efficient to estimate an expected spin image for the various training cases and simply compare the considered spin image to that small library of expected (mean or maximum likelihood) spin images.

As an example, the expected spin image for each class in Figure 6-4 is computed by averaging the spin images in each class. Each spin image is then compared to the expected spin images by using the linear correlation coefficient in equation 6-2. The mean of the correlation coefficients for each case is shown in Table 6-1. From Table 6-1, we see that the spin images in the class of large fractional tree canopies appear to be more correlated to the expected spin image of the complete tree class than the expected spin image of the class of small fractional tree canopies. Very weak correlation between the class of complete tree and the class of small

fractional tree canopies suggests reasonable separability between these two classes, which could be helpful in tree detection.

Another example for the case of different tree classes, such as PPINES-L, PPINES-H, and IMPAC, is shown in Figure 6-5. Five spin images are created for each class to compute the expected spin image, and the mean value of the correlation coefficients for each case is listed in Table 6-2. It shows a very weak correlation between the spin images in PPINES (both PPINES-L and PPINES-H) and the expected spin image in IMPAC, indicating that the spin image features offer good separability between plantations. The age difference (here, between PPINES and IMPAC) is well captured by the spin images while the cultural difference (here, between PPINES-L and PPINES-H) is not.

The results in Tables 6-1 and 6-2 are regarded as preliminary findings primarily because a small number of spin images were used. They do provide evidence, however, that spin images have the potential to separate full tree clusters from partial tree clusters and trees of one age from trees of another age. Thus, it is speculated that spin images could be used to revisit tree clusters that are suspected of erroneously grouping two trees into one cluster or over segmenting one tree into two clusters. Based on spin image results, old seed points could be deleted or new seed points could be instantiated and the clustering algorithm re-run for that small area to improve the tree detection accuracy.

Table 6-1. The mean value of the correlation coefficients for each case in Figure 6-4. Here, CT = complete tree clusters, LPT = large fraction of the tree canopies, and SPT = small fraction of the tree canopies.

	CT	LPT	SPT
CT	0.808	0.517	0.087
LPT	0.438	0.799	0.327
SPT	0.088	0.271	0.684

Table 6-2. The mean value of the correlation coefficients for each case in Figure 6-5. Five spin images are used to compute the expected spin image for each class.

	PPINES-L	PPINES-H	IMPAC
PPINES-L	0.815	0.673	0.263
PPINES-H	0.687	0.842	0.380
IMPAC	0.265	0.367	0.813

6.5 Reducing Computational Complexity

6.5.1 Number of Bins

Each pixel in the spin image is considered as a feature, so a high dimensional feature space is usually created. As a result, basic template matching is sometimes inefficient because: (1) each spin image comparison requires a correlation of two spin images, an operation on order of the relatively large number of bins (e.g. 160 bins in section 6.3) in a spin image; and (2) when a spin image is matched to the model library, its correlation with all of the spin images from all of the models should be computed. Therefore, it would be desirable to transform the spin image pixels into a low dimensional space via Principle Component Analysis (PCA), and then take a small number of features that capture most of the variance of the spin image. PCA is a common technique for image compression in object recognition (Murase and Nayar, 1995). By computing the eigenvectors of the covariance matrix of the set of vectors, PCA determines an orthogonal basis, called the eigenspace, in which to describe the vectors. PCA has become popular for efficient comparison of images because it is optimal in the correlation sense (Fukunaga, 1990).

6.5.2 Number of Points on an Object

There are some cases where the whole (or part) of the object can be pre-segmented before computing spin images. These cases resolve some issues of standard spin images and reduce the computational cost tremendously. Deciding on the size of spin image bins (resolution) and the

size of spin image (local region of interest) is not trivial, and it is important to have uniform mesh resolution over the entire model for spin image matching. These issues are much less problematic in the cluster-based spin images described here. Furthermore, the required costly search over all n spin images of the object to find the point that corresponds to a given spin image on an object of n points is greatly reduced by the initial segmentation.

6.5.3 Number of Spin Images

As we have seen in this study, there are cases where objects have irregular shapes. In these cases, many spin images should be created from each class and stored in the model library because of non-fixed shapes of the objects. This results in high computational cost during numerous spin image comparisons to the library even though great reduction is achieved by the initial segmentation. Instead of storing all the spin images for each class, one global pdf could be computed since the spin images from the same class would be similar. This global pdf can be less sensitive to noisy sampling on diffuse and non-regular object shapes. By considering each spin image as a 2D histogram, a non-parametric method such as Parzen window estimation can be used to compute individual 2D pdf. These 2D pdfs will be combined to create the global pdf for each class. Then, a simple way of comparing two spin images is measuring the Kullback-Leibler (KL) divergence between their two pdfs.

CHAPTER 7 CONCLUSIONS AND FUTURE WORK

7.1 Conclusions

Small footprint LiDAR technology can provide spatially dense coverage over forest canopies and penetrates the canopy by illuminating the ground and understory through small gaps in the crown layer. These advantages, relative to other remote sensing modalities, such as passive optical and radar, allow the identification of individual trees and the estimation of their heights and crown lengths from LiDAR data. Determining the optimal window sizes to accurately find treetops has been the most important and difficult part in the process of delineating single trees to date. An adaptive region growing method was developed by using an agglomerative hierarchical clustering structure to merge the partial-tree clusters that are segmented by the region growing process.

The entire process of the proposed approach was developed directly on the raw point cloud data to avoid loss of 3D information from interpolating the point data into height images. Working on point data with high point density requires more computational time and/or memory than working with images, but this can be alleviated by dividing the ROI into smaller areas to suit the memory resources of a particular computational platform (i.e. the ‘divide-and-conquer’ strategy). It was shown that the proposed algorithm performs very well overall for two managed pine plantation forests of different ages and species. The lowest detection accuracy occurred for the IMPAC plots with low culture because the canopies in these plots are more interlocked and variable in sizes than in other plots. However, the performance was more than 10% better at IMPAC than that of the scale-space method. The estimates of tree heights and crown lengths were slightly underestimated, but agreed with ground truth to within several decimeters.

Geometric mappings with field of view functions inside forests were developed to find optical gaps. The most probable walking trails in heavily vegetated areas were detected by computing optical lines of sight based on a set of visibility blockers and geometric constraints. I also found that it is possible to define relatively simple parameterizations of light interception by forested canopies that allow for the prediction of IPAR from ALSM data. I employed optical scope functions that constrained the field of view from the ground through the canopy towards the sun in order to estimate IPAR from a 3D point cloud of ALSM data. Several scope functions were investigated, and a simple cone function with a divergence angle of $\pm 7^\circ$ and distance weighting was found to produce very good agreement with *in situ* IPAR measurements across species and treatment classes.

Estimates of IPAR using ALSM data and a calibrated scope function are likely to be more statistically reliable across wide areas than *in situ* estimates of IPAR derived from a limited sample population. This is because estimates of IPAR obtained from ALSM data are spatially dense due to the fact that the scope function can be translated in small spatial increments. Because ALSM provides us with meter-scale 3D structure rather than simply vertical structure, we can easily compute the number of laser returns, which corresponds to the number of occlusions, from a hypothetical observer in the forest to any location in the sky. Furthermore, by knowing the site latitude and longitude and the sun's position on arbitrary dates and times, one could predict clear-sky IPAR for a variety of times of the year or times of the day using a couple of seasonally representative ALSM data sets (e.g. ALSM acquired during periods of peak and minimum leaf areas). Such predictions through time could be useful inputs for ecological process models.

7.2 Future Work

7.2.1 Extension to Different Forest Types

In the proposed tree detection algorithm, the stopping criterion on the agglomeration was determined by minimizing the Bayes error over the training data, resulting in a threshold τ . Additional features could, in principle, be incorporated for the estimation of τ , but that would likely make the results more sensitive to the specific training data set. Strictly speaking, the optimal value of τ for a given location will depend on characteristics of the ROI, such as the tree species, crown density, spacing between trees, and age of the trees. However, the small standard deviation in τ values obtained from repeated randomized sampling in this study suggests that conditioning the agglomeration on the standard deviation of point elevations is robust and that modest amounts of training data will suffice to estimate τ . To achieve optimal results over sites other than those examined here (particularly if those sites contain tree species other than Loblolly and Slash pine), one should train the algorithm using local ground truth data. It would be interesting to test the robustness of τ on natural forests and determine how much the detection rate is degraded.

In the estimation of IPAR, although testing over different forest types was not possible due to a lack of additional ground truth data, I expect that the proposed approach may perform well over other forests with minimal empirical calibration since I used scope functions described by a minimal set of parameters. In the case of the conical scope, I found the strongest dependence to be on a single parameter, the divergence angle α . This implies that the adjustment of one parameter may be sufficient to achieve reasonable agreement with ground-based measurement over differing forests. That performance would depend, however, on the nature of the understory. ALSM data obtains fewer returns from the understory than from the upper canopy. Thus, interception by the lower canopy and understory may be understated using the current approach.

This limitation of the ALSM measurement could be mitigated however by limiting observer points to be higher than some specified elevation above the ground, or by estimating 3D volumes for the detected trees (for example, by assuming a uniform biomass distribution inside a 3D convex hull of ALSM points on a tree). It should also be noted that if one were to use high observer elevations, the distance from the observer to the LiDAR points δ may then take on greater importance than it did in this study. This hypothesis requires further verification through future testing over other managed and natural forests as the ALSM and ground truth data become available.

7.2.2 Line-of-Sight Visibility

Two of the most critical factors governing estimating of optical flux through the canopy are topography and landcover. InSAR has been used to map topography at spatial resolutions of a few meters to tens of meters. However, in steep terrain, distortions in the topography caused by radar foreshortening lead to significant errors in the resulting Digital Elevation Models (DEMs). ALSM, on the other hand, can provide very high resolution 3D positions of millions of laser pulses that intercept the ground or landcover. By coupling 3D landcover density estimates with underlying topographic information, there are many applications that can be addressed, as extensions of the ideas of line-of-sight visibilities and optical scope functions in Chapters 3, such as: (1) optimal path planning through forested terrain to minimize traversal times, (2) reducing the vulnerability of personnel that occurs when forward progress is slowed due to impediments (dense vegetation), (3) detecting or avoiding detection of personnel by thermal InfraRed (IR) sensors, and (4) improving satellite-ground RF communications (including GPS reception) in forested terrain by locating and avoiding areas of high canopy density.

7.2.3 Multi-feature Spin Images

Spin images have been successfully used in shape matching by deriving a view-independent description of both database and query objects. Often, when range data are used to measure 3D structure, the targets are opaque to the laser. Thus, there is no penetration of the target by the laser and one obtains measurements of a true surface. In such cases, only surface information (surface shape) is accounted for in the spin image calculation. However, there are other instances where not only the surface shape is acquired but also some internal information due to penetration into the object, such as medical imaging, ranging sensor over rough loose material (or, an object with discontinuous surfaces), radar imaging of vegetated terrain, and LiDAR sensing over forests. These internal points can potentially provide more information, but these points could also cause problems in the calculation and matching of standard spin images.

Consequently, an extension of spin images, tentatively called multi-feature spin images, could be suggested to account for partial penetration of diffuse targets. This new approach is targeted to some special applications, but this could be looked at as a more general way of using spin images. Multi-feature spin images create more features than using the raw value of the point location in standard spin images or spin image in Brusco *et al.* (2005) that characterize texture values such as R, G, B, and luminance. This leads to potentially many scalar-valued spin images (one for each feature) at each local part of the object. The ‘features’ could consist of statistics that are extracted from the neighborhood of points inside a predefined region from the local origin, and appropriate features could be extracted depending on the applications. Since ALSM gives partial penetration over forest with intensity and last stop points, multi-feature spin images should allow better discrimination between different structures than standard spin images. Also, it is expected that this new approach could give better recognition for clusters that are in between tree clusters and partial-tree clusters in standard spin images as shown in Figure 6-4.

Feature-based spin images suggested here would promise better performance, but this method implies potentially high computational cost as the number of selected features grows. Therefore, reducing the number of features is very important to speed up the process, but in many cases, the best features are not known in advance so that many possible features need to be examined to see which features tend to give best separation between classes via spin images. One way to address this problem is computing mutual information (MI) over training data to select only those features that are most predictive of class separability. Optimal feature reduction for LiDAR data using MI was developed in (Luzum *et al.*, 2005). That method could be extended for this work such that simple PCA is still used to control the computational complexity of comparing scalar-valued spin images to the model library, and MI is used to select the subset of transformed spin image features that best predicts the class.

7.2.4 New ALSM Technology

Modern ALSM systems, such as the Optech Gemini system, have made it possible to map large areas much more efficiently than before by employing laser pulse rates in excess of 150 kHz. This laser pulse rate is five times faster than the Optech 1233 system that is used in this study. In addition, the Gemini system records four returns (instead of two returns with the 1233 system) and provides the choice of angle beam divergence (wide and narrow). Denser spatial coverage by this system can reduce the need for multiple flight lines and reduce the visible gaps in the point clouds between scan lines shown in Figure 4-19. The finer representations of tree canopies by this denser spatial and vertical resolution are expected to yield better accuracy in individual tree detection and tree parameter estimations. Moreover, it is anticipated to better observe understory vegetation, which will help to estimate line-of-sight visibilities in natural forests.

LIST OF REFERENCES

- Aber, J.D., and R. Freuder, 2000. Variation among solar radiation data sets for the Eastern US and its effects on predictions of forest production and water yield, *Climate Research*, 15: 33–43.
- Amaro, A., D. Reed, and P. Soares, 2003. *Modelling Forest Systems*, CABI Publishing, Cambridge, MA, USA.
- Andersen, H., S.E. Reutebuch, and G.F. Schreuder, 2001. Automated individual tree measurement through morphological analysis of a LIDAR-based canopy surface model, *Proceedings of the First International Precision Forestry Cooperative Symposium*, University of Washington, Seattle, USA, June 17-20, pp. 11–22.
- Andersen, H., S.E. Reutebuch, and G.F. Schreuder, 2002. Bayesian object recognition for the analysis of complex forest scenes in airborne laser scanner data, *International Archives of the Photogrammetry, Remote Sensing and Spatial Information Sciences*, 34(3A): 35–41.
- Assflag, J., G. D'Amico, A. Del Bimbo, and P. Pala, 2004. 3D content-based retrieval with spin images, *IEEE International Conference on Multimedia and Expo (ICME)*, Vol.2, 27–30, pp. 771-774.
- Babaud, J., A.P. Witkin, M. Baudin, and R.O. Duda, 1986. Uniqueness of the Gaussian kernel for scale-space filtering, *IEEE Transaction on Pattern Analysis and Machine Intelligence*, 8(1):26–33.
- Battaglia, M., and P.J. Sands, 1998. Process-based forest productivity models and their application in forest management, *Forest Ecology and Management*, 102:13–32.
- Beucher, S., and C. Lantuejoul, 1979. Use of watersheds in contour detection, *International Workshop on Image Processing, Real-time Edge and Motion Detection/Estimation*, Rennes, France.
- Binford, M.W., H.L. Gholz, G. Starr, and T.A. Martin, 2006. Regional carbon dynamics in the southeastern U.S. coastal plain: Balancing land cover type, timber harvesting, fire, and environmental variation, *Journal of Geophysical Research*, 111, D24S92, doi:10.1029/2005JD006820.
- Brandtberg, T., and F. Walter, 1998. Automated delineation of individual tree crowns in high spatial resolution aerial images by multiple-scale analysis, *Machine Vision and Applications*, 11:64–73.
- Brandtberg, T., T.A. Warner, R.E. Landenberger, and J.B. McGraw, 2003. Detection and analysis of individual leaf-off tree crowns in small footprint, high sampling density lidar data from the eastern deciduous forest in North America, *Remote Sensing of Environment*, 85(3): 290–303.

- Brock, J.C., C.W. Wright, A.H. Sallenger, W.B. Krabill, and R.N. Swift, 2002. Basis and methods of NASA Airborne Topographic Mapper LiDAR surveys for coastal studies, *Journal of Coastal Research*, 18(1):1–13.
- Brusco, N., M. Andreetto, A. Giorgi, and G.M. Cortelazzo, 2005. 3D registration by textured spin-images, *Proceedings of the 5th International Conference on 3-D Digital Imaging and Modeling (3DIM)*, 13-16, pp. 262–269.
- Butson, C., R. Fernandes, R. Latifovic, and C. Wenjun, 2002. A robust approach for estimating LAI from Landsat TM/ETM+ imagery, *Proceedings of the IEEE International Geoscience Remote Sensing Symposium (IGARSS '02)*, 4:2328–2330.
- Carter, W.E., R.L. Shrestha, G. Tuell, D. Bloomquist, and M. Sartori, 2001. Airborne Laser Swath Mapping shines new light on earth's topography, *EOS, Transactions American Geophysical Union*, 82(46):549–555.
- Chen, Q., D. Baldocchi, P. Gong, and M. Kelly, 2006. Isolating individual trees in a savanna woodland using small footprint LIDAR data, *Photogrammetric Engineering and Remote Sensing*, 72:923–932.
- Cho, H., and K.C. Slatton, 2007. Morphological processing of severely occluded digital elevation images to extract and connect stream channels, *IEEE International Conference on Image Processing (ICIP)*, 2:241–244.
- Colbert, S.R., E.J. Jokela, and D.G. Neary, 1990. Effects of annual fertilization and sustained weed-control on dry-matter partitioning, leaf-area, and growth efficiency of juvenile loblolly and slash pine, *Forest Science*, 36:995–1014.
- Cropper, W.P., and H.L. Gholz, 1993. Simulation of the carbon dynamics of a Florida slash pine plantation, *Ecological Modelling*, 66:231–249.
- Czaplewski, R.L., 1999. Multistage remote sensing: toward an annual national inventory, *Journal of Forestry*, 97(12):44–48.
- Dalla-Tea, F., and E.J. Jokela, 1991. Needlefall, canopy light interception, and productivity of young intensively managed slash and loblolly pine stands, *Forest Science*, 37:1298–1313.
- Dinh, H.Q., and S. Kropac, 2006. Multi-resolution spin-images, *Proceedings of the IEEE Society Conference on Computer Vision and Pattern Recognition (CVPR'06)*, 1:863–870.
- Dobson, M.C., L. Pierce, J. Kellndorfer, and F. Ulaby, 1997. Use of SAR image texture in terrain classification, *IEEE Geoscience and Remote Sensing Symp. (IGARSS)*, 3:1180–1183.
- Drake, J.B., R.O. Dubayah, D.B. Clark, R.G. Knox, J.B. Blair, M.A. Hofton, R.L. Chazdon, J.F. Weishampel, and S. Prince, 2002. Estimation of tropical forest structural characteristics using large-footprint LiDAR, *Remote Sensing of Environment*, 79:305–319.

- Du, G., and T.S. Yeo, 2002. A novel lacunarity estimation method applied to SAR image segmentation, *IEEE Transaction on Geoscience and Remote Sensing*, 40(12):2687–2691.
- Duda, R.O., P.E. Hart, and D.G. Stork, 2001. *Pattern Classification*, 2nd edition, John Wiley & Sons, USA.
- Eggleston, N.T., M. Watson, D.L. Evans, R.J. Moorhead, and J.W. McCombs, 2000. Visualization of airborne multiple-return LIDAR imagery from a forested landscape, *Proceedings of the ERIM International Conference on Geospatial Information in Agriculture Forestry*, 1:470–477.
- Farid, A., D.C. Goodrich, and S. Sorooshian, 2006. Using airborne Lidar to discern age classes of cottonwood trees, *Western Journal of Applied Forestry*, 21(3):149–158.
- Flood, M., 2002. From commercial data to commercial products: research priorities in the commercial sensor, *International Workshop on Three-dimensional Analysis of Forest Structure and Terrain Using LiDAR Technology*, Victoria, March 12–15.
- Fukunaga, K., 1990. *Introduction to statistical pattern recognition*, Academic Press, New York.
- Gay, L.W., K.R. Knoerr, and M.O. Braaten, 1971. Solar radiation variability on the floor of a pine plantation, *Agricultural Meteorology*, 8:39–50.
- Gholz, H.L., S.A. Vogel, W.P. Cropper, K. McKelvey, K.C. Ewel, R.O. Teskey, and P.J. Curran, 1991. Dynamics of canopy structure and light interception in *Pinus elliottii* stands in north Florida, *Ecological Monographs*, 61(1):35–51.
- Giesen, J.. *Sunshine applet*, URL: <http://www.jgiesen.de/sunshine/> (last date accessed: 21 October 2005).
- Gong, P., Y. Sheng, and G.S. Biging, 2002. 3D model-based tree measurement from high-resolution aerial imagery, *Photogrammetric Engineering and Remote Sensing*, 68(11):1203–1212.
- Gronbeck, C.. *Sun angle*, URL: <http://www.susdesign.com/sunangle/> (last date accessed: 21 October 2005).
- Gougeon, F.A., and D.G. Leckie, 2003. Forest information extraction from high spatial resolution images using an individual tree crown approach, *Information report BC-X-396*, Pacific Forestry Centre, Canadian Forest Service, Victoria, British Columbia, Canada.
- Halthore, R.N., S.E. Schwartz, J.J. Michalsky, M.H. Bergin, R.A. Ferrare, B.N. Holben, and H.M. ten Brink, 1996. A closure experiment: prediction and measurement of direct-normal solar irradiance at the ARM site, *American Geophysical Union Fall Meeting*, San Francisco, December, A11C-12, 15–19.

- Haugerud, R.A., D.J. Harding, S.Y. Johnson, J.L. Harless, C.S. Weaver, and B.L. Sherrod, 2003. High-resolution LiDAR topography of the Puget Lowland, Washington – a bonanza for earth science, *GSA Today*, 13(6):4–10.
- Hebert, M.T., and S.B. Jack, 1998. Leaf area index and site water balance of loblolly pine (*Pinus taeda* L.) across a precipitation gradient in east Texas, *Forest Ecology and Management*, 105:273–282.
- Holdcroft, C.J., C.L. Campbell, I.J. Davenport, R.J. Gurney, and N. Holden, 2005. Measurement of canopy geometry characteristics using LiDAR laser altimetry: A feasibility study, *IEEE Transaction on Geoscience and Remote Sensing*, 43(10):2270–2282.
- Holmgren, J., M. Nilsson, and H. Olsson, 2003. Estimation of tree height and stem volume on plots-using airborne laser scanning, *Forest Science*, 49:419–428.
- Holmgren, J., and A. Persson, 2004. Identifying species of individual trees using airborne laser scanning, *Remote Sensing of Environment*, 90:415–423.
- Hyde, P., R. Dubayah, B. Peterson, J.B. Blair, M. Hofton, C. Hunsaker, R. Knox, and W. Walker, 2005. Mapping forest structure for wildlife habitat analysis using waveform lidar: Validation of montane ecosystems, *Remote Sensing of Environment*, 96:427–437.
- Hyypä, J., J. Pulliainen, A. Saatsi, and M. Hallikainen, 1997. Radar-derived forest inventory by compartments, *IEEE Transactions on geoscience and remote sensing*, 35:392–404.
- Hyypä, J., H. Hyypä, M. Inkinen, M. Engdahl, S. Linko, and Y.H. Zhu, 2000. Accuracy comparison of various remote sensing data sources in the retrieval of forest stand attributes, *Forest Ecology and Management*, 128:109–120.
- Hyypä, O. K., M. Lehtikoinen, and M. Inkinen, 2001. A segmentation-based method to retrieve stem volume estimates from 3-D tree height models produced by laser scanners, *IEEE Transactions on geoscience and remote sensing*, 39(5):969–975.
- Hyypä, J., H. Hyypä, P. Litkey, X. Yu, H. Haggrén, P. Rönholm, U. Pyysalo, J. Pitkänen, and M. Maltamo, 2004. Algorithms and methods of airborne laser-scanning for forest measurements, *International Archives of Photogrammetry and Remote Sensing*, vol XXXVI, 8/W2, Freiburg, Germany.
- Johnson, A.E., 1997. *Spin-Images: A Representation for 3-D Surface Matching*, Ph.D. dissertation, Carnegie Mellon University, Pittsburgh, USA.
- Johnson, A.E., and M. Hebert, 1998. Recognizing objects by matching oriented points, *Proceedings of the IEEE Conference on Computer Vision and Pattern Recognition (CVPR)*, pp. 684–689.
- Johnson, A.E., and M. Hebert, 1999. Using spin-images for efficient multiple model recognition in cluttered 3-D scenes, *IEEE Transactions on Pattern Analysis and Machine Intelligence*, 21(5):433–449.

- Johnson, A.E., 2000. Surface landmark selection and matching in natural terrain, *Proceedings of the IEEE Conference on Computer Vision and Pattern Recognition (CVPR)*, 2:413–420.
- Jokela, E.J., and T.A. Martin, 2000. Effects of ontogeny and soil nutrient supply on production, allocation, and leaf area efficiency in loblolly and slash pine stands, *Canadian Journal of Forest Research*, 30:1511–1524.
- Kampa, K., and K.C. Slatton, 2004. An adaptive multiscale filter for segmenting vegetation in ALSM data, *IEEE Geoscience and Remote Sensing Symp. (IGARSS)*, 6:3837–3840.
- Koch, B., U. Heyder, and H. Weinacker, 2006. Detection of individual tree crowns in airborne lidar data, *Photogrammetric Engineering and Remote Sensing*, 72(4):357–363.
- Koenderink, J.J., 1984. The structure of images, *Biological Cybernetics*, 50:363–370.
- Kucharik, C.J., J.M. Normana, and S.T. Gower, 1998. Measurements of leaf orientation, light distribution and sunlit leaf area in a boreal aspen forest, *Agricultural and Forest Meteorology*, 91:127–148.
- Landsberg, J.J., and S.T. Gower, 1997. *Applications of Physiological Ecology to Forest Management*, Academic Press, New York.
- Leckie, D.G., F.A. Gougeon, D.A. Hill, R. Quinn, L. Armstrong, and R. Shreenan, 2003. Combined high-density lidar and multispectral imagery for individual tree crown analysis, *Canadian Journal of Remote Sensing*, 29(5):633–649.
- Lefsky, M.A., W.B. Cohen, S.A. Acker, G.G. Parker, T.A. Spies, and D. Harding, 1999a. LiDAR remote sensing of the canopy structure and biophysical properties of Douglas-fir western hemlock forests, *Remote Sensing of Environment*, 70:339–361.
- Lefsky, M.A., D. Harding, W.B. Cohen, G. Parker, and H.H. Shugart, 1999b. Surface LiDAR remote sensing of basal area and biomass in deciduous forests of eastern Maryland, USA, *Remote Sensing of Environment*, 67:83–98.
- Lieffers, V.J., C. Messier, K.J. Stadt, F. Gendron, and P.G. Comeau, 1999. Predicting and managing light in the understory of boreal forests, *Canadian Journal of Forest Research*, 29:796–811.
- Limas Serafim, A.F, 1997. Discrimination of natural homogeneous textures based on fractal models, *Proceedings of the IEEE International Symposium on Industrial Electronics (ISIE)*, 3:773–778.
- Lindeberg, T., 1993. On scale selection for differential operators, *Proceedings of 8th Scandinavian Conference on Image Analysis*, Tromso, Norway, 2:857–866.
- Lindeberg, T., 1996. Scale-space: a framework for handling image structure at multiple scales, *Proceedings of CERN School of Computing*, Egmond aan Zee, The Netherlands, 8–21.

- Lim, K., P. Treitz, M. Wulder, B. St-onge, and M. Flood, 2003. LiDAR remote sensing of forest structure, *Progress in Physical Geography*, 27:88–106.
- Long, J.N., T.J. Dean, and S.D. Roberts, 2004. Linkages between silviculture and ecology: examination of several important conceptual models, *Forest Ecology and Management*, 200(1-3):249–261.
- Luzum, B.J., K.C. Slatton, and R.L. Shrestha, 2005. Analysis of spatial and temporal stability of airborne laser swath mapping data in feature space, *IEEE Transactions in Geoscience and Remote Sensing*, 43(6):1403–1420.
- MacFarlane, D.W., E.J. Green, A. Brunner, and R.L. Amateis, 2003. Modeling loblolly pine canopy dynamics for a light capture model, *Forest Ecology and Management*, 173:145–168.
- Mader, G.L., 1992. Rapid static and kinematic Global Positioning System solutions using the ambiguity function technique, *Journal of Geophysical Research*, 97:3271–3283.
- Maltamo, M., K. Mustonen, J. Hyypä, J. Pitkanen, and X. Yu, 2004. The accuracy estimating individual tree variables with airborne laser scanning in a boreal nature reserve, *Canadian Journal of Forest Research*, 34:1791–1801.
- Mandelbrot, B., 1982. *The Fractal Geometry of Nature*, W.H. Freeman and Company.
- Martin, T.A., and E.J. Jokela, 2004. Developmental patterns and nutrition impact radiation use efficiency components in southern pine stands, *Ecological Applications*, 14:1839–1854.
- McCrary, R.L., and E.J. Jokela, 1996. Growth phenology and crown structure of selected loblolly pine families planted at two spacings, *Forest Science*, 42:46–57.
- McCrary, R.L., and E.J. Jokela, 1998. Canopy dynamics, light interception, and radiation use efficiency of selected loblolly pine families, *Forest Science*, 44:64–72.
- Means, J.E., S.A. Acker, D.J. Harding, J.B. Blair, M.A. Lefsky, W.B. Cohen, M.E. Harmon, and W.A. McKee, 1999. Use of large-footprint scanning airborne LiDAR to estimate forest stand characteristics in the western Cascades of Oregon, *Remote Sensing of Environment*, 67:298–308.
- Messier, C., and P. Puttonen, 1995. Spatial and temporal variation in the light environment of developing Scots pine stands: the basis for a quick and efficient method of characterizing light, *Canadian Journal of Forest Research*, 25:343–354.
- Montieth, J.L., 1972. Solar radiation and productivity in tropical ecosystems, *Journal of Applied Ecology*, 9:747–766.
- Morsdorf, F., E. Meier, B. Allgöwer, and D. Nuesch, 2003. Clustering in airborne laser scanning raw data for segmentation of single trees, *International Archives of the Photogrammetry, Remote Sensing and Spatial Information Sciences*, 34, Part 3/W 13, pp. 27–33.

- Murase, H., and S. Nayar, 1995. Visual learning and recognition of 3-D objects from appearance, *International Journal of Computer Vision*, 14:5–24.
- Ni-Meister, W., D.L.B. Jupp, and R. Dubayah, 2001. Modeling LiDAR waveforms in heterogeneous and discrete canopies, *IEEE Transaction on Geoscience and Remote Sensing*, 39(9):1943–1958.
- Parker, G.G., M.A. Lefsky, and D.J. Harding, 2001. Light transmittance in forest canopies determined from airborne LiDAR altimetry and from in-canopy quantum measurements, *Remote Sensing of Environment*, 76:298–309.
- Persson, A., J. Holmgren, and U. Soderman, 2002. Detecting and measuring individual trees using an airborne laser scanner, *Photogrammetric Engineering and Remote Sensing*, 68(9):925–932.
- Popescu, S.C., R.H. Wynne, and R.F. Nelson, 2003. Measuring individual tree crown diameter with lidar and assessing its influence on estimating forest volume and biomass, *Canadian Journal of Remote Sensing*, 29:564–577.
- Popescu, S.C., R.H. Wynne, and J. Scrivani, 2004. Fusion of small-footprint lidar and multispectral data to estimate plot-level volume and biomass in deciduous and pine forests in Virginia, USA, *Forest Science*, 50(4):551–565.
- Popescu, S.C., and R.H. Wynne, 2004. Seeing the trees in the forest: Using lidar and multispectral data fusion with local filtering and variable window size for estimating tree height, *Photogrammetric Engineering and Remote Sensing*, 70(5):589–604.
- Pyysalo, U., and H. Hyypä, 2002. Reconstructing tree crowns from laser scanner data for feature extraction, *International Society for Photogrammetry and Remote Sensing – ISPRS Commission III Symposium (PCV'02)*.
- Reurebuch, S., H. Andersen, and R. McGaughey, 2005. Light detection and ranging (LIDAR): an emerging tool for multiple resource inventory, *Journal of Forestry*, 103(6):286–292.
- Roth, B.E., E.J. Jokela, T.A. Martin, D.A. Huber, and T.L. White, 2007a. Genotype x environment interactions in selected loblolly and slash pine plantations in the southeastern United-Sates, *Forest Ecology and Management*, 238:175–188.
- Roth, B.E., K.C. Slatton, and M.J. Cohen, 2007b. On the potential for high-resolution lidar to improve rainfall interception estimates in forest ecosystems, *Frontiers in Ecology and the Environment*, 5(8):421–428.
- Saatchi, S.S., R. Treuhaft, and M.C. Dobson, 1994. Estimation of leaf area index over agricultural areas from polarimetric SAR images, *Proceedings of the IEEE International Geoscience Remote Sensing Symposium (IGARSS '94)*, 2:826–828.
- Sampson, D.A., and H.L. Allen, 1998. Light attenuation in a 14-year-old loblolly pine stand as influenced by fertilization and irrigation, *Trees – Structure and Function*, 13:80–87.

- Sampson, D.A., and H.L. Allen, 1999. Regional influences of soil available water-holding capacity and climate, and leaf area index on simulated loblolly pine productivity, *Forest Ecology and Management*, 124:1–12.
- Samuelson L.J., K. Johnsen, and T. Stokes, 2004. Production, allocation, and stemwood growth efficiency of *Pinus taeda* L. stands in response to 6 years of intensive management, *Forest Ecology and Management*, 192:59–70.
- SAS Institute Inc., 2000. SAS/STAT User's Guide: Version 8, vols. 1–3, SAS Institute Inc., Cary, NC, 3884 pp.
- Schardt, M., M. Ziegler, A. Wimmer, R. Wack, and R. Hyyppä, 2002. Assessment of forest parameter by means of laser scanning, *The International Archives of the Photogrammetry, Remote Sensing and Spatial Information Sciences*, Graz, Austria, XXXIV, 3A, 302-309.
- Shrestha, R.L., W.E. Carter, M. Lee, P. Finer, and M. Sartori, 1999. Airborne Laser Swath Mapping: accuracy assessment for surveying and mapping applications, *Journal of American Congress on Surveying and Mapping*, 59(2):83–94.
- Slatton, K.C., M.M. Crawford, and B.L. Evans, 2001. Fusing interferometric radar and laser altimeter data to estimate surface topography and vegetation heights, *IEEE Transaction on Geoscience and Remote Sensing*, 39(11):2470–2482.
- Slatton, K.C., W.E. Carter, and R.L. Shrestha, 2005. A simulator for Airborne Laser Swath Mapping via photon counting, *Proceedings of the SPIE 2005 Defense and Security Symposium*, 5794:12–20.
- Slatton, K.C., W.E. Carter, R.L. Shrestha, and W. Dietrich, 2007. Airborne Laser Swath Mapping: Achieving the resolution and accuracy required for geosurficial research, *Geophysical Research Letters*, 34, L23S10.
- Song, C., 2007. Estimating tree crown size with spatial information of high resolution optical remotely sensed imagery, *International Journal of Remote Sensing*, 28(15):3305–3322.
- Swindel, B.F., D.G. Neary, N.B. Comerford, D.L. Rockwood, and G.M. Blakeslee, 1988. Fertilization and competition control accelerate early southern pine growth on flatwoods, *Southern Journal of Applied Forestry*, 12:116–121.
- Todd, K., F. Csillag, and P. Atkinson, 2003. Three-dimensional mapping of light transmittance and foliage distribution using LiDAR, *Canadian Journal of Remote Sensing*, 29(5):544–555.
- Turcotte, D.L., 1997. *Fractals and chaos in geology and in geophysics*, 2nd edition, Cambridge.
- Wack, R., M. Schardt, U. Lohr, L. Barrucho, and T. Oliveira, 2003. Forest inventory for eucalyptus plantations based on airborne laser scanner data, Proceedings of the ISPRS working group III/3 workshop, “3-D reconstruction from airborne laser scanner and InSAR data”, S. 1–1.

- Wang, Y.P., and P.G. Jarvis, 1990. Description and validation of an array model – MAESTRO, *Agricultural and Forest Meteorology*, 51:157–180.
- Waring, R.H., and W.H. Schlesinger, 1985. *Forest Ecosystems: Concepts and Management*, Academic Press, New York.
- Weed, C.A., M.M. Crawford, A.L. Neuenschwander, and R. Gutierrez, 2002. Classification of LiDAR data using a lower envelope follower and gradient based operator, *Proceedings of the IEEE International Geoscience Remote Sensing Symposium (IGARSS)*, 3:1384–1386.
- Will, R.E., N.V. Narahari, B.D. Shiver, and R.O. Teskey, 2005. Effects of planting density on canopy dynamics and stem growth for intensively managed loblolly pine stands, *Forest Ecology and Management*, 205:29–41.
- Witkin, A.P., 1983. Scale-space filtering, *Proceedings of 8th International Joint Conference on Artificial Intelligence*, Karlsruhe, Germany, 1019–1022.
- Zacks, S., 1994. *Stochastic Visibility in Random Fields – Lecture Notes in Statistics*, Springer-Verlag.
- Zhang, K., S. Chen, D. Whitman, J. Yan, and C. Zhang, 2003. A progressive morphological filter for removing nonground measurements from airborne LIDAR data, *IEEE Transaction on Geoscience and Remote Sensing*, 41(4):872–882.

BIOGRAPHICAL SKETCH

Heezin Lee was born in Kwang-Yang, South Korea. He received his B.S. degree in electrical engineering from Sung-Kyun-Kwan University, South Korea in 1995 and his M.S. degree in electrical engineering and computer science from Syracuse University, Syracuse, New York in 1999. Since 2000, he has been working toward his Ph.D. degree in electrical and computer engineering at the University of Florida. He began working under the supervision of Dr. K. Clint Slatton in 2003. His research interests broadly include remote sensing, pattern recognition, image processing, and digital signal processing.